1997

Interfacial characterizations and analytical applications of chemically-modified surfaces

Jianhong Wang
Iowa State University

INFORMATION TO USERS

This manuscript has been reproduced from the microfilm master. UMI films the text directly from the original or copy submitted. Thus, some thesis and dissertation copies are in typewriter face, while others may be from any type of computer printer.

The quality of this reproduction is dependent upon the quality of the copy submitted. Broken or indistinct print, colored or poor quality illustrations and photographs, print bleedthrough, substandard margins, and improper alignment can adversely affect reproduction.

In the unlikely event that the author did not send UMI a complete manuscript and there are missing pages, these will be noted. Also, if unauthorized copyright material had to be removed, a note will indicate the deletion.

Oversize materials (e.g., maps, drawings, charts) are reproduced by sectioning the original, beginning at the upper left-hand corner and continuing from left to right in equal sections with small overlaps. Each original is also photographed in one exposure and is included in reduced form at the back of the book.

Photographs included in the original manuscript have been reproduced xerographically in this copy. Higher quality 6" x 9" black and white photographic prints are available for any photographs or illustrations appearing in this copy for an additional charge. Contact UMI directly to order.

UMI

A Bell & Howell Information Company
300 North Zeeb Road, Ann Arbor MI 48106-1346 USA
313/761-4700 800/521-0600

Interfacial characterizations and analytical applications of chemically-modified surfaces

by

Jianhong Wang

A dissertation submitted to the graduate faculty

in partial fulfillment of the requirements for the degree of

DOCTOR OF PHILOSOPHY

Major: Analytical Chemistry

Major Professor: Marc D. Porter

Iowa State University

Ames, Iowa

1997

Graduate College
Iowa State University

This is to certify that the Doctoral dissertation of

Jianhong Wang

has met the dissertation requirements of Iowa State University

Signature was redacted for privacy.

Major Professor

Signature was redacted for privacy.

For the Major Program

Signature was redacted for privacy.

For the Graduate College

DEDICATION

This dissertation is dedicated to my family, whose love and support helped me through the difficult times, my husband Xiaobing Xie, my parents Zhengli Wang and Chunmei Nie, and my brother Jianping Wang.

TABLE OF CONTENTS

ACKNOWLEDGMENTS

I would like to gratefully acknowledge my major professor Marc D. Porter for his guidance, encouragement, confidence and patience during the past five years of study. The results presented in this dissertation are a product of the combined efforts of myself with a select set of Porter group members. Dr. Shelley Coldiron, Dr. Bikas Vaidya and Steve Watson are acknowledged for their contribution in the pH sensor project. Dr. Chuanjian Zhong is acknowledged for his contribution in the chloride removal project. Discussions with Dr. John-Bruce Green and Dr. Vivian Jones are greatly appreciated for the SFM projects. Jeremy Kenseth is acknowledged for the synthesis of dithio-bis(succinimidylundecanoate). This research was funded by Hach Company, National Science Foundation, Microanalytical Instrumentation Center of Iowa State University, Center for Advanced Technology Development, and Ames Laboratory. The Ames Laboratory is operated for the U. S. Department of Energy by Iowa State University under contract No. W-7405-eng-82. The United States government has assigned the DOE Report number IS-T 1835 to this thesis.

I would also like to thank my husband Xiaobing Xie, and my parents, Zhengli Wang and Chunmei Nie for their love, patience, encouragement, and continuous support throughout the years.

GENERAL INTRODUCTION

Introduction

During the past decade, important advances have been made towards intelligent design and fabrication of chemically modified surfaces for a variety of applications, including electrocatalysis, corrosion, lubrication, environmental monitoring, chemical sensors, and biotechnology.[1-4] The utility of the surface modification in chemical analysis is of particular interest because of the critical role of liquid- and gas-solid interfaces in a host of transduction mechanisms that rely on the specificity and extent of the interactions between an analyte and the surface. Novel strategies and methodologies have been developed to achieve the desired surface architecture on various surfaces including polymer coatings and monolayer assemblies. These developments have created enormous opportunities in many cross-disciplinary fields such as material science, analytical chemistry and physical chemistry, aiming at both advancements in fundamental understanding and technological applications of interfacial phenomena. Central to these efforts are the ability to tailor the surface architecture in ways that will optimize the rates and selectivities of chemical processes occurring at the interfaces, and the ability to examine interfacial reactions at levels that will allow nanoscale or molecular structures to be rationally probed. For the latter ability, while the use of scanning probe microscopies (SPM) has proved valuable due to their capabilities in characterizing the microscopic structure of surfaces with a high spatial resolution, relatively little efforts have been given to study the microscopic interfacial reactivities in situ. The creation of these abilities constitutes one of the major challenges to

analytical chemists. To meet the challenge, the goal of this work is to explore several new strategies and approaches to the surface modification and the microscopic characterization of interfaces in the areas mainly targeting sensor technologies that are of interest to environmental control or monitoring, and SPM techniques that can monitor interfacial chemical reactions in real time.

As a starting point, the following sections will review the latest developments in the above activities with focus on specific areas. First, a literature review of the development of optical pH sensors is provided. Second, the development of scanning force microscopy (SFM) is described with emphasis on the instrumentation and modes of operation. Finally, a review of a variety of methods for the elimination of chloride interference in chemical oxygen demand (COD) determination is presented.

Optical Sensors. Chemical sensors are probes used to determine the concentration of an analyte through chemical interaction with an immobilized reagent. If this interaction between the analyte and the reagent causes a change in the optical properties of the reagent phase which is measured through the optical fiber, they become fiber-optical chemical sensors. Development, characterization, and application of optical chemical sensors for pH, metal ions, gases, and biological materials have in recent years become an area of rapidly increasing research activity.[5-14] Chemical sensors involving the immobilization of colorimetric reagents at optical fibers have been developed for applications in biomedical[14] and environmental analyses,[15] as well as in process analytical chemistry.[12]

The large number of optical pH sensors developed is, in part, a result of the availability of acid-base indicators on which to base the sensor design, and, in part, due to the

importance of pH determinations. Compared with the electrochemical sensors, the main advantages that the optical pH sensors offer include the lack of necessity of reference electrodes, minimal susceptibility to electrical interference, internal calibration, and most importantly, capability for remote sensing through fiber optics.[16] Most of the optical sensors developed for pH measurement are based on absorbance[17-28] or fluorescence[13, 29-38] measurements in the UV-visible region via an indicator immobilized on a support material. However, measurements based on changes in reflectance,[39-45] fluorescence lifetime,[46, 47] evanescent wave absorption[48-50] and infrared spectroscopy[51] have also been developed. Sensors for pH have employed acid-base indicators that have been immobilized at a variety of polymeric materials,[19-22, 30, 38, 40-43, 51-53] ion-exchange resins,[33, 39, 54] and porous[32, 37, 55] or "sintered" glasses.[31] Diverse techniques have been utilized to immobilize the acid-base indicators, which include adsorption of the chromophore on polymeric supports[56-58] or directly on the fiber;[19] covalent bond to the fiber[59] or to a fixed support;[60] entrapment in polymeric structures;[61, 62] and sol-gel procedure.[50, 63] Most optical pH sensors developed suffer from some disadvantages compared with the electrochemical sensors, such as limited dynamic range, poor long-term stability, and slow response. In Chapter 1, the development of a new pH sensing film with a large pH dynamic range, fast response, and improved long-term stability based on the covalent immobilization of fluoresceinamine at cellulose acetate thin film.

Scanning Force Microscopy. Scanning probe microscopies are quickly becoming routine methods in many laboratories. The ability to probe the microscopic and nanoscopic structure of surfaces in a variety of ambient conditions with a low-maintenance instrument

that sits on a benchtop has contributed to the popularity of these technologies. Scanning tunneling microscopy (STM), invented in 1982, was the first technique capable of directly imaging surface atoms in real space.[64] The success of STM for achieving atomically resolved images of surfaces triggered the development of a variety of other scanning probe microscopes. Among these, and the most popular, is the scanning force microscopy (SFM), invented in 1986 by Gerd Binnig, Calvin Quate and Christoph Gerber.[65] Whereas STM functions by scanning a sharp metal tip over the surface of a conducting or semiconducting sample, an SFM does not require a tip or a sample to be conductive. Therefore, virtually all materials can be imaged using variations of SFM.

Instead of using a tunneling current to sense the proximity of the scanning tip to the surface, force microscopies take advantage of the variety of short- and long-range forces between two masses (e.g., van der Waals, magnetic, and electrostatic forces). Force microscopes image a sample by scanning a probe mounted on a cantilever across a sample surface and then detecting the changes in the forces between the tip and the surface by measuring the deflections of the cantilever. However, unlike STM there are a number of different methods for detecting the deflection of the cantilever, such as tunneling,[65] capacitance,[66] interferometry,[67] optical beam deflection,[68] and others. Optical beam deflection is the simplest and most widely used of these force detection methods. Figure 1 shows a SFM design equipped with an optical beam deflection system. A laser beam is reflected off of the backside of the cantilever into a position-sensitive diode detector. By using a photodiode composed of four independent parts, the vertical deflection of the cantilever in

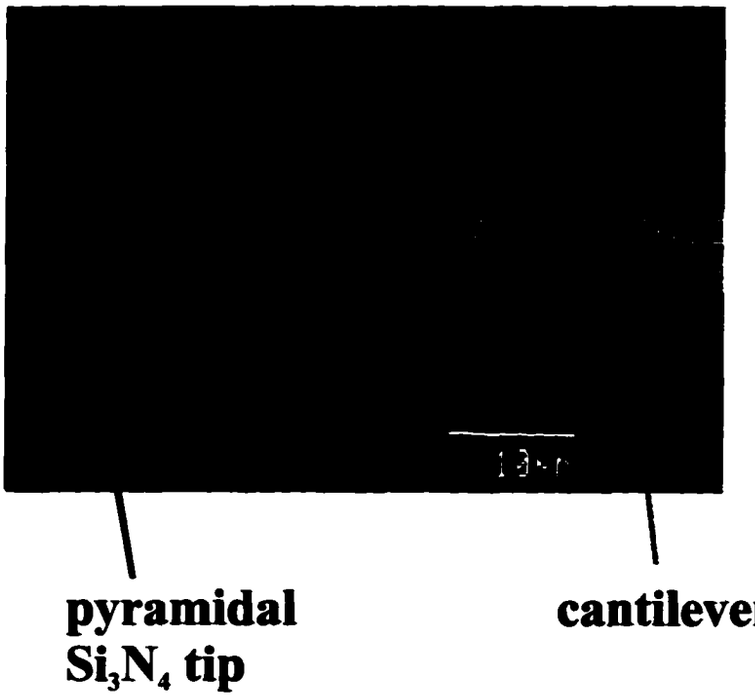

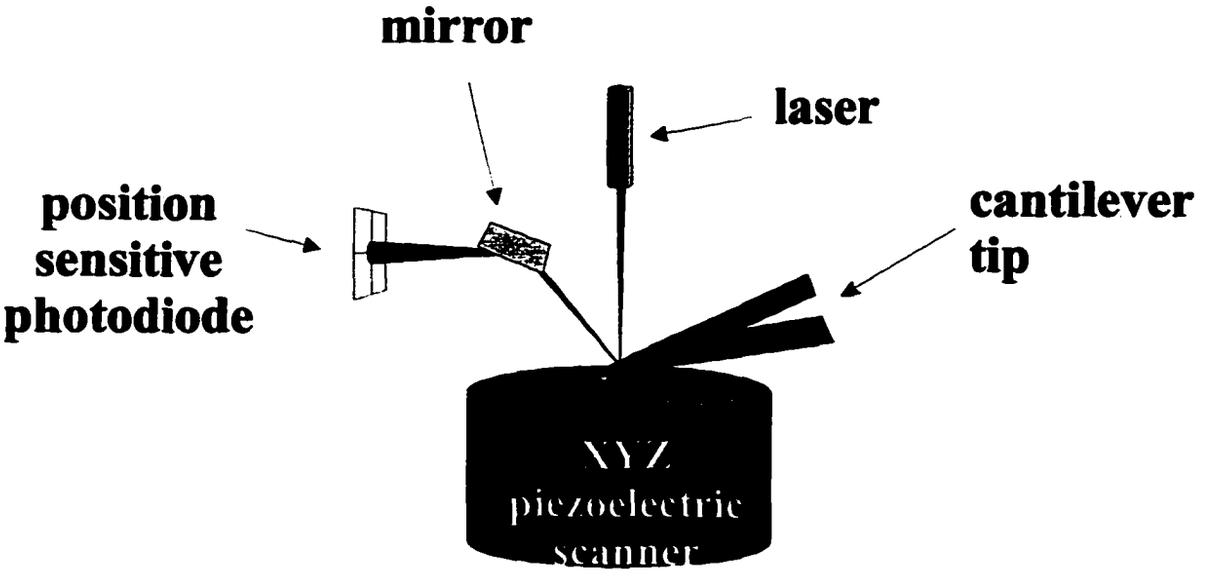

Figure 1. Schematic of the principle components for an optical lever type SFM (Reproduced from (95)).

response to surface topography, as well as its torsional motion due to the frictional force between tip and sample, can be measured simultaneously.

SFM can be operated in various modes. The most elementary mode of SFM operation is the contact mode. With this mode, a cantilevered tip is brought into direct physical contact with a sample. As the tip is rastered across the surface, the deflection of the tip is used to map out the topography. As with all SPM techniques, the use of a feedback loop is optional. In one case, deflection without feedback is plotted as a function of sample position, and in the other case, a feedback loop dynamically adjusts the vertical position of the sample in an effort to keep the deflection constant. Topographical information can be obtained in this way. New modes of SFM have been developed to measure material properties, such as elasticity, adhesion, friction, etc. Elasticity may be determined from one variation of contact mode known as force modulation.[69] The vertical position of the sample is modulated while the tip is in contact with the sample, and the resulting cantilever deflection may be correlated with the elasticity of the tip-sample contact zone. Non-contact mode SFM has also been developed to image soft samples, such as biological materials and soft polymers, which otherwise can be damaged by the larger forces of contact mode operation. A common noncontact SFM technique uses a stiff cantilever held above the sample surface and oscillated at a frequency close to its resonance frequency. When the tip is brought close to the surface, the resonance frequency of the cantilever is modified by the force gradient between the tip and sample. The van der Waals force extends far enough above the sample to influence the tip without the tip actually touching the surface. The

change in the oscillation of the cantilever can be measured using most deflection detection methods.

While SFM has proven invaluable in addressing issues related to the nanoscale topography of a wide variety of interfacial materials, we have been focusing on extending the capabilities of SFM to increase the chemical content gained from the imaging process.[70, 71] One of our goals was to take advantage of the nanoscale resolution of SFM to characterize interfacial chemical transformations in situ at the molecular level. The model system we chose to conduct the study results from the spontaneously adsorbed monolayers (SAMs). SAMs have been proposed as model systems for the study of a wide range of surface effects[3] due to their well-defined composition and structure, extraordinary stability both in vacuum and in ambient, and most significantly the high degree of control over the chemical and physical properties of the interface. Of those, the most well studied are formed by the chemisorption of alkyl thiols ($X(CH_2)_nSH$) to gold electrodes.[3] Figure 2 illustrates the idealized structure of an alkyl thiolate monolayer adsorbed on gold. There are effectively three regions to the monolayer film: 1) the adsorbate-substrate interface; 2) the body of the adsorbate; and 3) the adsorbate-environment interface. Among all the characterization techniques for the monolayers, infrared reflection absorption spectroscopy (IRRAS) has proven the most valuable.[72] In our studies, IRRAS was utilized together with SFM to characterize the chemical reactions at the monolayer-solution interface both macroscopically and microscopically. Chapter 2 demonstrates the applicability of SFM for characterizing interfacial chemical reactions at a nanoscale level. Chapter 3 further demonstrates the

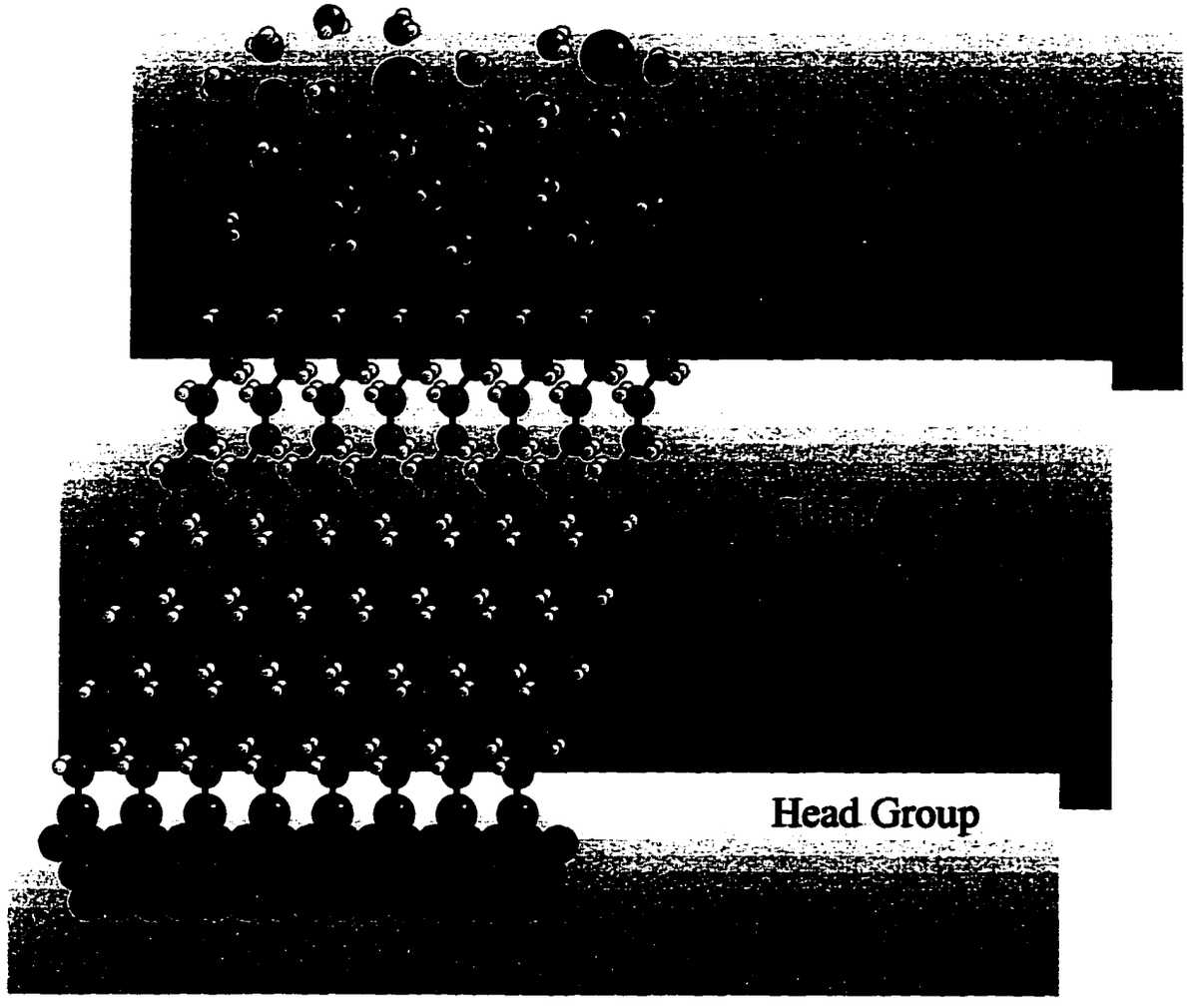

Figure 2. Idealized structure of alkyl thiolate monolayers at Au(111) (Reproduced from (95)).

capability of SFM of modifying surface locally, and the impact of this type of processing to the nanofabrication of surfaces for sensor technology.

Chloride Interference in Chemical Oxygen Demand Determination. Oxygen demand is an important parameter for determining the effect of organic pollutants on receiving water. As microorganisms in the environment consume these materials, oxygen is depleted from the water. This can have adverse effect on fish and plant life. There have been several methods developed to measure this oxygen demand,[73] among which chemical oxygen demand (COD) is widely applied over other methods (e.g., biochemical oxygen demand (BOD) and total organic carbon (TOC)). Acidic dichromate is commonly used for the oxidation of the organic material for a COD determination.[73-92] While not an organic pollutant, chloride ion can be oxidized by acidic dichromate which can result in a positive deviation in a COD determination. In addition, ammonia also gets oxidized in presence of chloride, which is otherwise not oxidized by the acidic dichromate.[93] Thus, the chloride interference in a sample containing ammonia is even more pronounced.

The present methods of COD determination mask the effect of chloride ion by addition of a mercury salt[74, 75, 79, 81, 86, 90-92] which reacts with chloride ion to form an unreactive complex. Other attempted approaches to manage the problem of chloride ion interference include the addition of silver salts[82-85] to mask chloride ion, the addition of chromium(III)[87] to reduce the oxidation potential, the determination of the amount of chloride oxidized by iodometric titration with a subsequent correction for the oxidized chloride,[80] and the removal of chloride as hydrochloric acid from an acidified sample solution.[93, 94] However, the effectiveness of these approaches for compensation vary depending on sample matrix.

Furthermore, as environmental regulations are tightening, it has become increasingly important to develop a more environmentally friendly approaches for COD and other chemical analysis. Hence, an efficient and environmentally friendly method of chloride removal in COD determination is clearly needed. Since an electrode can be used as a reagent for oxidation or reduction reaction, and it is also reusable and environmental friendly, we developed an electrochemical approach to the elimination of Cl^- interference in COD analysis and is described in Chapter 4.

Dissertation Organization

Centered on the main theme, four specific topics are presented as four chapters in this dissertation following the general introduction. Chapter 1 describes the development of two immobilization schemes for covalently immobilizing fluoresceinamine at cellulose acetate and its application as a pH sensing film. Chapter 2 investigates the applicability of SFM to following the base-hydrolysis of a dithio-bis(succinimidylundecanoate) monolayer at gold in situ. Chapter 3 studies the mechanism for the accelerated rate of hydrolysis of the dithio-bis(succinimidylundecanoate) monolayer at Au(111) surface. Chapter 4 focuses on the development of an electrochemical approach to the elimination of chloride interference in Chemical Oxygen Demand (COD) analysis of waste water. The procedures, results and conclusions are described in each chapter.

References

(1) Zhong, C. J.; Porter, M. D. *Anal. Chem.* **1995,** *67*, 709A-715A.

(2) *Interfacial Design and Chemical Sensing*; American Chemical Society: Washington, DC, 1994.

(3) Ulman, A. *An Introduction to Ultrathin Organic Films: From Langmuir Blodgett to Self-Assembly*; Academic Press: New York, 1991.

(4) *Handbook of Surface Imaging and Visualization*; CRC Press: Boca Raton, FL, 1995.

(5) Janata, J. In *Principles of Chemical Sensors*; Plenum: New York, 1989, chapter 1.

(6) Wohltjen, H. *Anal. Chem.* **1984,** *56*, 87A-103A.

(7) Janata, J. *Anal. Chem.* **1990,** *62*, 33R-44R.

(8) Seitz, W. R. *Anal. Chem.* **1984,** *56*, 16A-34A.

(9) Narayanaswamy, R. *Anal. Proc.* **1985,** *22*, 204-206.

(10) Wolfbeis, O. S. *Fresenius'Z. Anal. Chem.* **1986,** *325*, 387-392.

(11) Wolfbeis, O. S. *Anal. Proc.* **1987,** *24*, 14-15.

(12) Hirschfeld, T.; Callis, J. B.; Kowalski, B. R. *Science* **1984,** *226*, 312-318.

(13) Brenci, M.; Baldini, F. *IEEE Lasers and Electro-Optics Society and Optical Society of America* **1992,** *8th Optical Fiber Sensors Conference*, 313-319.

(14) Peterson, J. I.; Vurek, G. G. *Science* **1984,** *224*, 123-125.

(15) Callis, J. B.; Illman, D. L.; Kowalski, B. R. *Anal. Chem.* **1987,** *59*, 624A-637A.

(16) Janata, J. *Anal. Chem.* **1987,** *59*, 1351-1356.

(17) Harper, G. B. *Anal. Chem.* **1975,** *47*, 348-351.

(18) Mimms, L. T.; Mcknight, M. A.; Murray, R. W. *Anal. Chim. Acta* **1977,** *89*, 355-361.

(19) Boisde, G.; Biatry, B.; Magny, B.; Dureault, B.; Blanc, F.; Sebille, B. *SPIE* **1989,** *1172, Chemical, Biochemical, and Environmental Sensors*, 239-250.

(20) Jones, T. P.; Porter, M. D. *Anal. Chem.* **1988,** *60*, 404-406.

(21) Guthrie, A. J.; Narayanaswamy, R.; Welti, N. A. *Talanta* **1988,** *35*, 157-159.

(22) Stole, S. M.; Jones, T. P.; Chau, L. K.; Porter, M. D. In *Chemical Sensors and Microinstrumentation*; Murray, R. W., Dessy, R. E., Heineman, W. R., Janata, J., Seitz, W. R., Eds.; American Chemical Society, 1989; Vol. 403, pp 283-302.

(23) Porter, M. D.; Coldiron, S. J.; Vaidya, B. *SAE Technical Paper Series* **1993,** *932207*, 1-5.

(24) Edmonds, T. E.; Flatters, N. J.; Jones, C. F.; Miller, J. N. *Talanta* **1988,** *35*, 103-107.

(25) Collison, M. E.; Meyerhoff, M. E. *Anal. Chem.* **1990,** *62*, 425A-437A.

(26) Jones, T. P.; Coldiron, S. J.; Deninger, W. J.; Porter, M. D. *Applied Spectroscopy* **1991,** *45*, 1271-1277.

(27) Cardwell, T. J.; Cattrall, R. W.; Deady, L. W.; Dorkos, M.; O'Connell, G. R. *Talanta* **1993,** *40*, 765-768.

(28) Werner, T.; Wolfbeis, O. S. *Fresenius J Anal Chem* **1993,** *346*, 564-568.

(29) Saari, L. A.; Seitz, W. R. *Anal. Chem.* **1983,** *55*, 667-670.

(30) Munkholm, C.; Walt, D. R.; Milanovich, F. P.; Klainer, S. M. *Anal. Chem.* **1986,** *58*, 1427-1430.

(31) Offenbacher, H.; Wolfbeis, O. S.; Furlinger, E. *Sensors and Actuators* **1986,** *9*, 73-84.

(32) Fuh, M. R. S.; Burgess, L. W.; Hirschfeld, T.; Christian, G. D. *Analyst* **1987,** *112,* 1159-1163.

(33) Zhang, Z.; Seitz, W. R. *Anal. Chim. Acta* **1984,** *160,* 47-55.

(34) Zen, J.-M.; Patonay, G. *Anal. Chem.* **1991,** *63,* 2934-2938.

(35) Tan, W. H.; Shi, Z. Y.; Kopelman, R. *Anal. Chem.* **1992,** *64,* 2985-2990.

(36) Parker, J. W.; Laksin, O.; Yu, C.; Lau, M. L.; Klima, S.; Fisher, R.; Scott, I.; Atwater, B. W. *Anal. Chem.* **1993,** *65,* 2329-2334.

(37) Wolfbeis, O. S.; Offenbacher, H. *Sensors and Actuators* **1986,** *9,* 85-91.

(38) Zhang, Z.; Zhang, Y.; Ma, W.; Russell, R.; Shakhsher, Z. M.; Grant, C. L.; Seitz, W. R. *Anal. Chem.* **1989,** *61,* 202-205.

(39) Moreno, M. C.; Martinez, A.; Millan, P.; Camara, C. *J. Mol. Struct.* **1986,** *143,* 553-556.

(40) Ruzicka, J.; Hansen, E. H. *Anal. Chim. Acta* **1985,** *173,* 3-21.

(41) Woods, B. A.; Ruzicka, J.; Christian, G. D. *Anal. Chem.* **1986,** *58,* 2496-2502.

(42) Narayanaswamy, R.; III, F. S. *Anal. Chim. Acta* **1986,** *189,* 365-369.

(43) Kirkbright, G. F.; Narayanaswamy, R.; Welti, N. A. *Analyst* **1984,** *109,* 15-17.

(44) Woods, B. A.; Ruzicka, J.; Christian, G. D.; Rose, N. J.; Charlson, R. J. *Analyst* **1988,** *113,* 301-306.

(45) Shakhsher, Z.; Seitz, W. R.; Legg, K. D. *Anal. Chem.* **1994,** *66,* 1731-1735.

(46) Szmacinski, H.; Lakowicz, J. R. *Anal. Chem.* **1993,** *65,* 1668-1674.

(47) Thompson, R. B.; Lakowicz, J. R. *Anal. Chem.* **1993,** *65,* 853-856.

(48) Carey, W. P.; DeGrandpre, M. D. *Anal. Chem.* **1989,** *61*, 1674-1678.

(49) Ge, Z. F.; Brown, C. W.; Sun, L. F.; Yang, S. C. *Anal. Chem.* **1993,** *65*, 2335-2338.

(50) Lee, J. E.; Saavedra, S. S. *Anal. Chim. Acta* **1994,** *285*, 265-269.

(51) Jones, T. P.; Porter, M. D. *Applied Spectroscopy* **1989,** *43*, 908-911.

(52) Peterson, J. I.; Goldstein, S. R.; Fitzgerald, R. V. *Anal. Chem.* **1980,** *52*, 864-869.

(53) Jordan, D. M.; Walt, D. R. *Anal. Chem.* **1987,** *59*, 437-439.

(54) Kagedal, L.; Akerstrom, S. *Acta Chem. Scand.* **1971,** *25*, 1855-1859.

(55) Saari, L. A.; Seitz, W. R. *Anal. Chem.* **1982,** *54*, 821-823.

(56) Russell, D. A.; Narayanaswamy, R. *Anal. Chim. Acta* **1989,** *220*, 75-81.

(57) Bacci, M.; Baldini, F.; Cosi, F.; Conforti, G.; Scheggi, A. M. *Springer Proceedings in Physics*, Paris, France 1989; Springer-Verlag Berlin Heidelberg; 425-430.

(58) Chau, L. K.; Porter, M. D. *Anal. Chem.* **1990,** *62*, 1964-1971.

(59) Tromberg, B. J.; Sepaniak, M. J. *Anal. Chem.* **1987,** *59*, 1226-1230.

(60) Posch, H. E.; Leiner, M. J. P.; Wolfbeis, O. S. *Fresenius Z Anal Chem* **1989,** *334*, 162-165.

(61) Kawabata, Y.; Kamichika, T.; Imasaka, T.; Ishibashi, N. *Anal. Chim. Acta* **1989,** *219*, 223-229.

(62) Munkholm, C.; Walt, D. R. *Talanta* **1988,** *35*, 109-112.

(63) Lacan, P.; Gall, P. L.; Rigola, J.; Lurin, C.; Wettling, D.; Guizard, C.; Cot, L. *SPIE* **1992,** *1758*, 464-475.

(64) Binnig, G.; Rohrer, H.; Gerber, C.; Weibel, E. *Phys. Rev. Lett.* **1982,** *49*, 57.

(65) Binnig, G.; Quate, C. F. *Phys. Rev. Lett.* **1986,** *56*, 930-933.

(66) Neubauer, G.; Cohen, S. R.; McClelland, G. M.; Horne, D.; Mate, C. M. *Rev. Sci. Instrum.* **1990,** *61*, 2296-2308.

(67) Schönenberger, C.; Alvarado, S. F. *Rev. Sci. Instrum.* **1989,** *60*, 3131-3134.

(68) Meyer, G.; Amer, N. M. *Appl. Phys. Lett.* **1988,** *53*, 1045-1047.

(69) Overney, R. M.; Bonner, T.; Meyer, E.; Ruetschi, M.; Luthi, R.; Howald, L.; Frommer, J.; Guntherodt, H. J.; Fujihira, M.; Takano, H. *J. Vac. Sci. Technol. B* **1994,** *12*, 1973-1976.

(70) Green, J.-B. D.; McDermott, M. T.; Porter, M. D.; Siperko, L. M. *J. Phys. Chem.* **1995,** *99*, 10960-10965.

(71) Green, J.-B. D.; McDermott, M. T.; Porter, M. D. *J. Phys. Chem.* **1996,** *100*, 13342-13345.

(72) Porter, M. D.; Bright, T. B.; Allara, D. L.; Chidsey, C. E. D. *J. Am. Chem. Soc.* **1987,** *109*, 3559-3568.

(73) In *Standard Methods for the Examination of Water and Wastewater*; Greenberg, A. E., Trussel, R. R., Clesceri, L. S., Eds.; American Public Health Association: New York, 1985; Vol. 16.

(74) Himebaugh, R. R.; Smith, M. J. *Anal. Chem.* **1979,** *51*, 1085-1087.

(75) Gibbs, C. R. In *Technical Information Series-Booklet No. 8*; Hach Company, 1993.

(76) Moore, W. A.; Kroner, R. C.; Ruchhoft, C. C. *Anal. Chem.* **1949,** *21*, 953-957.

(77) Moore, W. A.; Ludzack, F. J.; Ruchhoft, C. C. *Anal. Chem.* **1951,** *23*, 1297-1300.

(78) Moore, W. A.; Walker, W. W. *Anal. Chem.* **1956,** *28*, 164-167.

(79) Dobbs, R. A.; Williams, R. T. *Anal. Chem.* **1963,** *35*, 1064-1067.

(80) Bauman, F. J. *Anal. Chem.* **1974,** *46*, 1336-1338.

(81) Jirka, A. M.; Carter, M. J. *Anal. Chem.* **1975,** *47*, 1397-1402.

(82) Lloyd, A. *Analyst* **1982,** *107*, 1316-1319.

(83) Ballinger, D.; Lloyd, A.; Morrish, A. *Analyst* **1982,** *107*, 1047-1053.

(84) Pitrebois, L.; Schepper, H. D. *Trib. Cebedeau* **1984,** *37*, 83-86.

(85) Casseres, K. E. d.; Best, D. G.; May, B. D. In *Wat. Pollut. Control*, 1984, pp 416-419.

(86) Jones, B. M.; Sakaji, R. H.; Daughton, C. G. *Anal. Chem.* **1985,** *57*, 2334-2337.

(87) Thompson, K. C.; Mendham, D.; Best, D.; Casseres, K. E. d. *Analyst* **1986,** *111*, 483-485.

(88) Gonzalez, J. F. *Environmental Technology Letters* **1986,** *7*, 269-272.

(89) Soto, M.; Veiga, M. C.; Méndez, R.; Lema, J. M. *Environmental Technology Letters* **1989,** *10*, 541-548.

(90) Dasgupta, P. K.; Petersen, K. *Anal. Chem.* **1990,** *62*, 395-402.

(91) Belkin, S.; Brenner, A.; Abeliovich, A. *Wat. Res.* **1992,** *26*, 1583-1588.

(92) Belkin, S.; Brenner, A.; Abeliovich, A. *Wat. Res.* **1992,** *26*, 1577-1581.

(93) Wagner, V. R.; Ruck, W. *Z. Wasser Abwasser Forsch* **1981,** *14*, 145-151.

(94) Wagner, V. R.; Ruck, W. *Z. Wasser Abwasser Forsch* **1982,** *15*, 287-290.

(95) Green, J.-B. D., Ph.D dissertation, Iowa State University, Ames, 1996.

CHAPTER 1. AN OPTICAL SENSOR WITH EXTENDED PH SENSITIVITY BASED ON THE CO-IMMOBILIZATION OF FLUORESCEINAMINE AND CONGO RED AT A POROUS CELLULOSIC FILM

A paper to be submitted to *Applied Spectroscopy*

Jianhong Wang, Shelley J. Coldiron, Bikas Vaidya, Steve W. Watson, and Marc D. Porter

Abstract

A new approach to the design and construction of an optical pH sensor has been developed by co-immobilizing two indicators at a porous cellulosic polymer film. This sensor was fabricated by covalently binding Congo Red and fluoresceinamine to a cellulose acetate film that had previously been subjected to an exhaustive base hydrolysis. The advantages of the sensor include a rapid response time (< 30 s), a large dynamic range (~9 pH units) and exceptional long-term stability. The rapid response results from the porous structure of the hydrolyzed polymeric support, which minimizes barriers to mass transport. The large dynamic range results from both the polyprotic acid-base reactivity of Congo Red and fluoresceinamine, and the high optical absorptivity of their various ionic forms. The stability of the sensor results from the strong covalent forces formed between the dye and the substrate. An absorbance-based internal calibration scheme, which takes advantage of the

optical properties of each of the reactive forms of the immobilized indicators, is presented. The response characteristics of the two fluoresceinamine sensors, including response time and reversibility, ionic strength and temperature effects, metal-ion interference, and their fluorescence properties vs. pH are evaluated.

Introduction

Several studies have recently described the immobilization of colorimetric reagents at optical fibers as an effective approach to the construction of sensors for pH determinations.[1-9] To date, fabrication schemes have principally focused on the immobilization of chemically selective reagents at a variety of polymeric materials[3-5, 8, 10] and sintered glasses,[8, 11] and on attaching polymeric dyes directly to the distal end of the fiber.[1, 2, 12, 13] For example, a fluorescent indicator was covalently immobilized in photodeposited polymer matrices on optical imaging fibers.[1] Although demonstrating fast response time, approaches to the design and construction of sensors that extend performance over a broader pH range, and minimize calibration frequency, would greatly facilitate usage. This paper presents the results of a series of investigations that address both performance attributes.

In the following sections, we present the results of a series of studies on the performance evaluation of optical sensors for pH determinations based on two fabrication schemes, direct and indirect covalent immobilization of an indicator at a base-hydrolyzed cellulose acetate film. The construction of a two-component pH sensor, which is based on the co-immobilization of two indicators at a porous cellulosic film, is also presented. Unlike

most immobilization techniques, water was used as the solvent during activation of the support.

Several advantages of these sensors include a rapid response time (< 30 s), a large dynamic range (> 7 pH units), and exceptional long-term stability. The rapid response results from the porous structure of the hydrolyzed polymeric support, which minimizes barriers to mass transport between the analyte and immobilized indicator. The large dynamic range results from both the polyprotic acid-base reactivity of the indicators and the high optical absorptivity of the various ionic forms, which gives rise to the high pH sensitivity for measurement in the UV-visible range The stability of the sensors results from both the strong covalent and interactive forces formed between the dye and the substrate, and the internal calibration scheme, which not only compensates for the instrumental fluctuations, but also minimizes the changes in the amount of the immobilized dye. The optical and chemical properties of the sensors as a function of pH were evaluated by conventional transmission spectroscopy.

Experimental Section

Dye Immobilization Procedures. (i) Direct Immobilization. A. Polymer film preparation: The support coatings were fabricated by spin-coating (Photo Resist Spinner 1-EC101DT-R485, Headway Research Inc., Garland, TX) a 14% (w/v) solution of cellulose acetate in cyclohexanone at 1000 rpm for 60 s onto precleaned glass microscope slides. After drying for 12-24 h, the films were hydrolyzed in 0.1 M KOH for 24 h, a process that yields a

porous, high-surface-area cellulosic film.[14] The film thickness, after hydrolyzation, was ~10 μm, as measured with a Dektak IIA Surface Profiler (Sloan Tech, Santa Barbara, CA).

B. Cyanogen bromide (CNBr) activation: The hydrolyzed cellulose acetate films were placed in 20 mL of deionized water. To this, 0.5 g of CNBr was slowly added while stirring the solution at room temperature and maintaining the pH between 10-11 with 2 M Na_2CO_3. The reaction time was limited to 5 min. The activated film was then rinsed with deionized water to remove any residual CNBr, and placed into a fluoresceinamine dye bath at room temperature for 24 h for covalent dye immobilization. The aqueous dye bath was prepared by dissolving 1 mM fluoresceinamine into sodium borate buffer (pH 9).

(ii) Indirect Immobilization. A. Immobilization of fluoresceinamine onto epoxy beads: The epoxide beads were pulverized into a powder to minimize particle aggregation in solution. The particle size ranges from 0.5~1 μm after pulverization. 1:10 (w/w) of fluoresceinamine to the pulverized epoxy beads were weighed and immersed in 1 M Na_2HPO_4. The solution was stirred for 48 h at room temperature. The excess dye was filtered and rinsed with 0.1 M Na_2HPO_4. The dyed beads were dried at 70 °C for ~12 h.

B. Sensing film preparation: The dried bead product was homogeneously dispersed in 14% cellulose acetate/cyclohexanone. The sensor film was fabricated by spin-coating the suspension onto cleaned glass microscope slides at 1000 rpm for 60 s. After drying for 12 h at 70 °C, the film was hydrolyzed in 0.1 M KOH for 24 h. The film thickness was ~15 μm.

(iii) Co-Immobilization. A hydrolyzed cellulose acetate film was activated using CNBr, as described in the above section. The activated film was placed into a Congo Red-fluoresceinamine dye bath (1:10 molar ratio) of pH ~9 at room temperature for 24 h.

Flow Cell Experiments. An operational diagram of the flow cell used for absorbance measurements is shown in Figure 1. The pH of the solutions were measured with an Orion Research 720A pH meter (Boston, MA). A solution flow of 0.48 mL/s was maintained by using a Cole Parmer 7518-00 Peristaltic pump (Chicago, Illinois). The optical properties of the sensor were characterized as a function of pH in a conventional transmission mode with a Hewlett Packard HP 8452A UV-Vis spectrophotometer (Santa Clara, CA). The fluorescence properties of fluoresceinamine were characterized as a function of pH in both solution and immobilized form with a SPEX Fluorolog 2-F112AI double monochromator spectrofluorometer (Metuchen, NJ) equipped with a 450 W xenon lamp. Solution pH was controlled either by varying the concentration of HCl or NaOH or by buffering with citrate and phosphate solutions. All solutions were prepared with deionized water (Millipore Corp., Bedford, MA).

Chemical Reagents. Powdered cellulose acetate (acetyl content 39.8%), fluoresceinamine (isomer I) and CNBr were purchased from Aldrich (Milwaukee, WI). Cyclohexanone (purified grade) and Na_2CO_3 were purchased from Fisher Scientific (Pittsburgh, PA). Polymer carrier VA-epoxy beads were purchased from Crescent Chemicals (Hauppauge, NY). These beads range in size from 50 to 200 μm, with average pore diameters of 30 nm and a surface area of 140 m^2/g.

Results and Discussion

Immobilization of Fluoresceinamine. (i) CNBr Activation Process. The first step in the reaction of CNBr with the hydroxyl groups of the hydrolyzed cellulose acetate

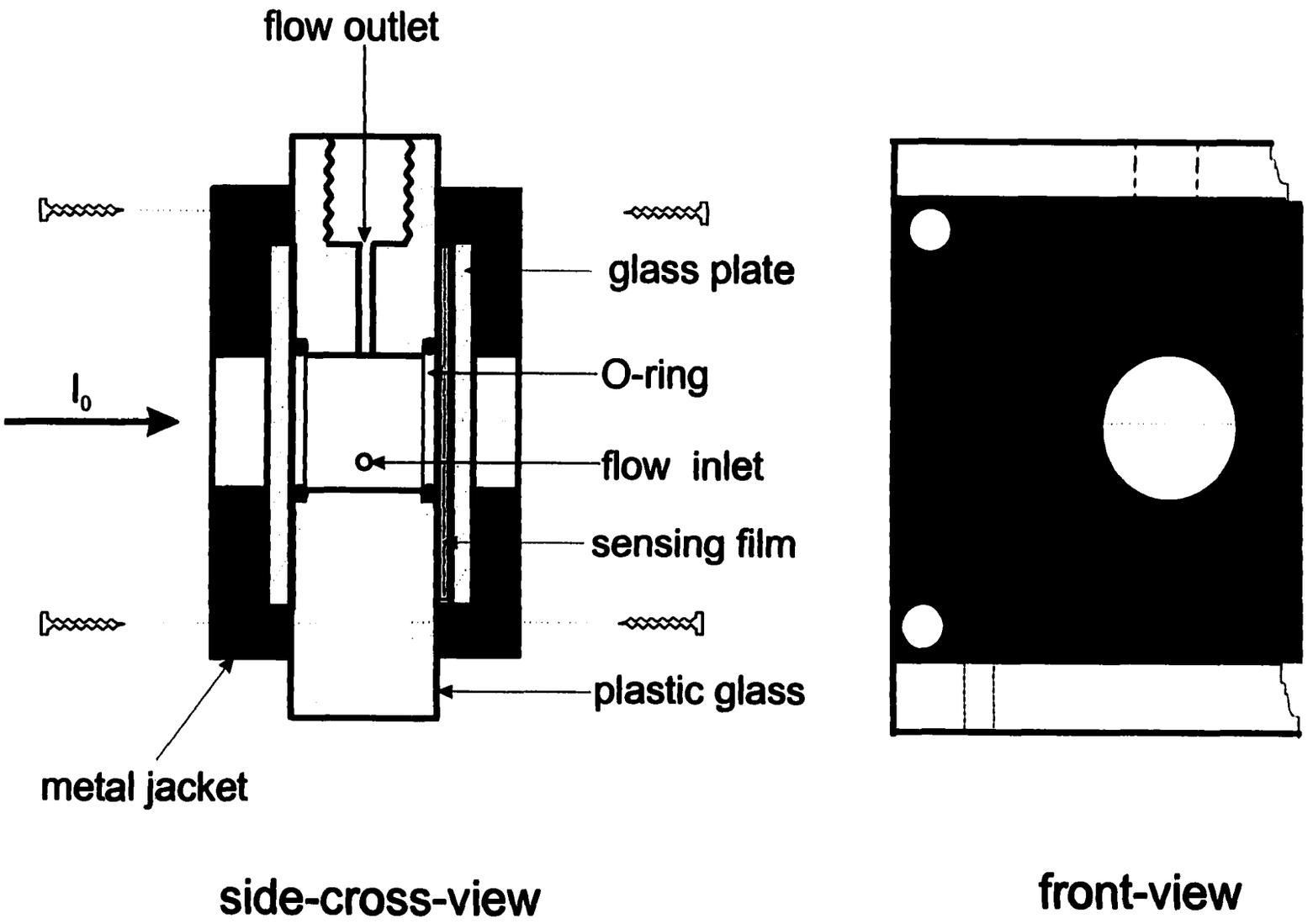

Figure 1. Schematic diagram of the flow cell.

(Scheme 1) yields cyanate esters which are unstable intermediates.[15, 16] In water, the reaction proceeds to a reactive imidocarbonate product and an unreactive carbamate product. The imidocarbonates are viewed as the active groups for subsequent coupling with amine groups of a variety of dyes.

A strongly basic reaction medium (pH 11.0-12.5) was employed during the activation to increase the coupling capacity of the polymer.[15] Unfortunately, these conditions lead to the rapid hydrolysis of CNBr to the inert cyanate ion (OCN^-)[15, 16] before CNBr reacts with the polymer. This undesirable side reaction cannot be avoided but can be suppressed by optimizing the conditions for imidocarbonate formation, e.g., using low reaction temperatures or relatively short reaction times. In our experiments, the reaction time was limited to 5 min.

(ii) Coupling of Fluoresceinamine To CNBr-Activated Cellulose Acetate. The coupling of fluoresceinamine occurs through the free amino groups (Scheme 2). Isourea, N-substituted imidocarbonate, and N-substituted carbamate are believed to be the immobilization products.[15, 16] Due to the large background contribution from the cellulose acetate matrix, we have been unable to identify the products using IR spectrometry of the immobilized fluoresceinamine. An alkaline reaction medium was used for the coupling reaction and the pH is lower than that in the activation process.

(iii) Indirect Immobilization. Under alkaline conditions, the epoxy polymer beads react with fluoresceinamine via the primary amine group (Scheme 3).[17] Chemically, these polymer beads are copolymers based on vinyl acetate and divinylethylene-urea. The surface is modified with oxirane groups after hydrolysis of the acetate groups.[18] These epoxide

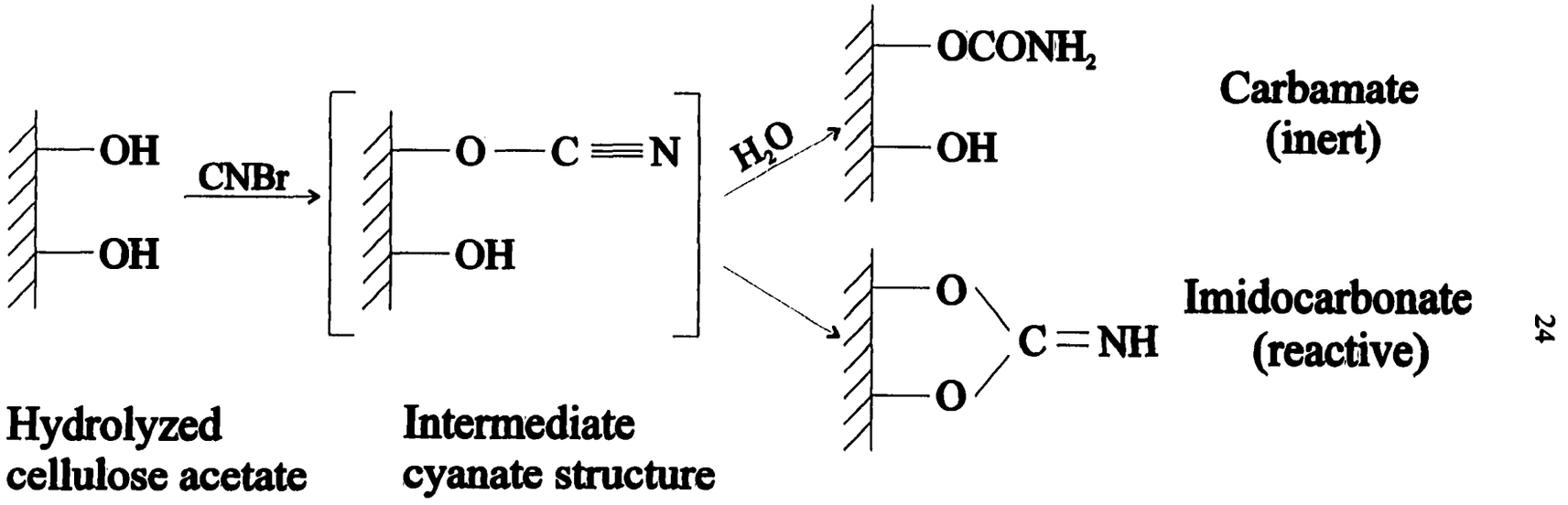
OH
OH
CNBr
O — C ≡ N
OH
H2O
OCONH2
OH
Carbamate
(inert)
O
O
C = NH
Imidocarbonate
(reactive)
Hydrolyzed
cellulose acetate
Intermediate
cyanate structure

Scheme 1

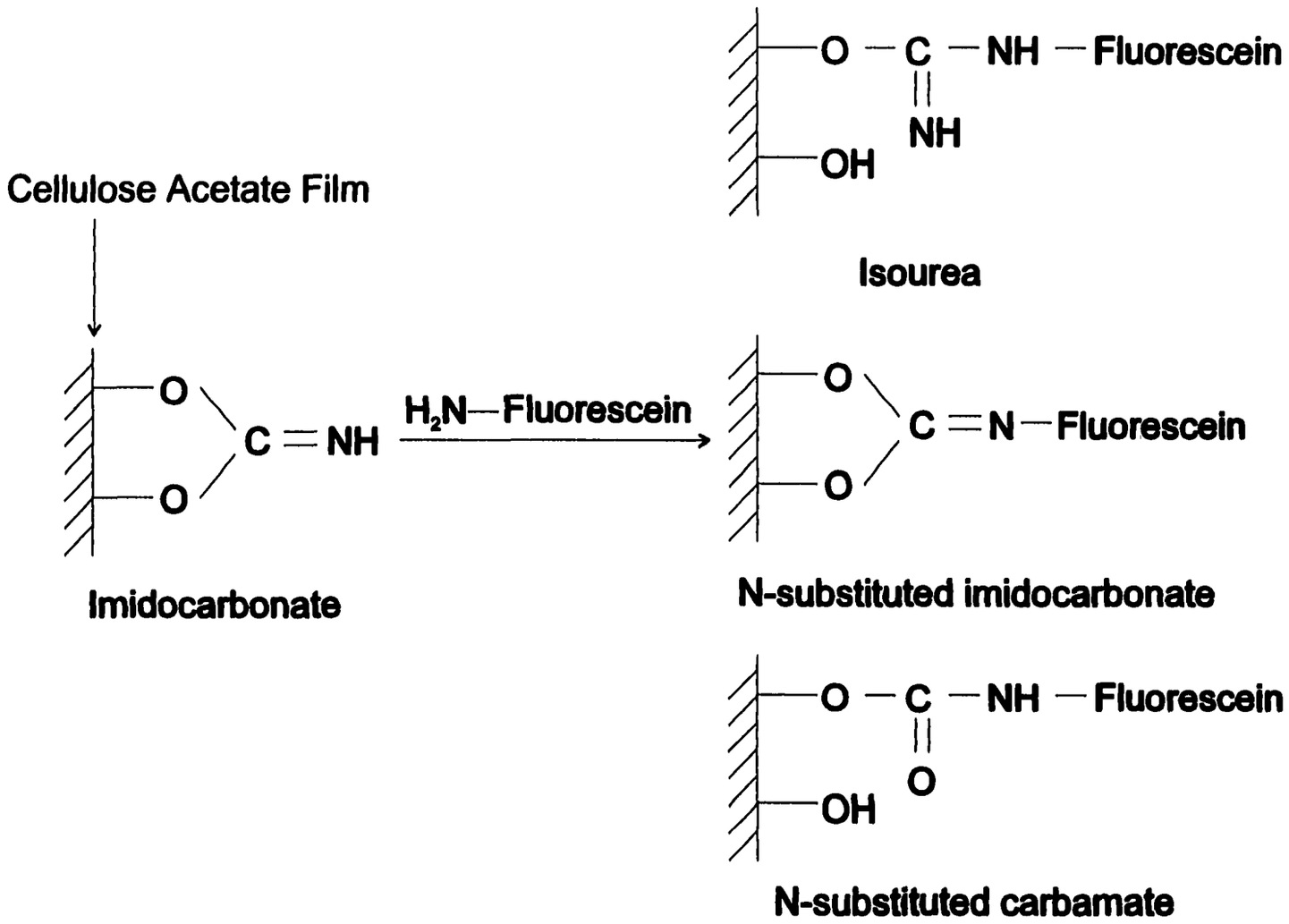
Cellulose Acetate Film
O
C = NH
O
Imidocarbonate
H2N—Fluorescein
O — C — NH — Fluorescein
NH
OH
Isourea
O
C = N — Fluorescein
O
N-substituted imidocarbonate
O — C — NH — Fluorescein
O
OH
N-substituted carbamate

Scheme 2

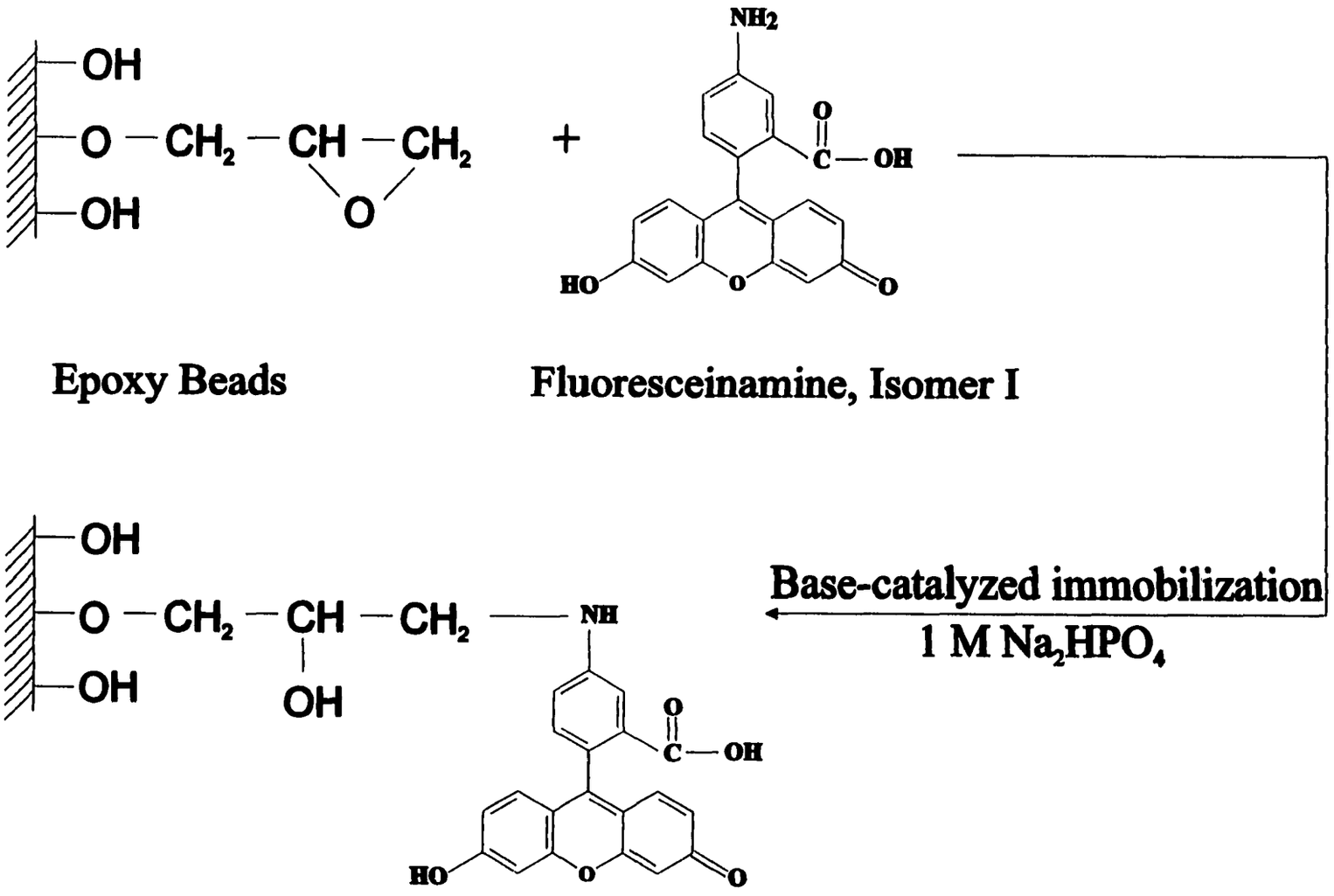
OH
O — CH2 — CH — CH2
OH
O
+
NH2
O
C — OH
HO
O
O
Epoxy Beads
Fluoresceinamine, Isomer I
Base-catalyzed immobilization
1 M Na2HPO4
NH
OH

Scheme 3

linkages are highly reactive and can be utilized to couple various compounds. Advantageous properties of the beads include: high structural stability, chemical stability over a wide pH range, and negligible swelling or shrinking with changing pH or salt concentration.

Response Characteristics of the Sensors. (i) Optical Properties of the Fluoresceinamine Sensors vs. pH. The absorption spectra of fluoresceinamine in solution and immobilized both directly and indirectly at a hydrolyzed cellulose acetate film are shown as a function of pH in parts A, B and C of Figure 2, respectively. The spectra in Figure 2A indicate that the solution form of fluoresceinamine behaves as a polyprotic dye, undergoing a succession of protonation steps between a pH of ~0 and 9. These transformations result in the observed differences in the solution spectra where, for example, the dye has an absorption maximum of 440 nm at a pH of 0.1 and of 488 nm at a pH of 9.0. These spectra, together with that for fluorescein,[19] indicate that there are four acid-base equilibria in this pH range.

The optical response of fluoresceinamine pH sensors are shown in Figure 2B and 2C for direct and indirect immobilization, respectively. It is noted that in Figure 2C, there is a baseline shift. This shift is due in part to light scattering and absorption by the epoxy beads in cellulose acetate matrix, as indicated by non-dyed, bead-dispersed blank film samples.[17] This shift can be compensated for by subtracting the background spectra of cellulosic film and crushed epoxy beads from the fluoresceinamine absorption spectra.

These spectra indicate that the sensors exhibit a dynamic range of more than 7 pH units. It is evident that the immobilized and solution forms of fluoresceinamine exhibit similar optical properties and acid-base reactivities. This similarity indicates that the acid-base reactivities of fluoresceinamine are only slightly affected by the immobilization process.

Figure 2. Absorption spectra for fluoresceinamine in solution (A), immobilized directly (B) and indirectly (C) at hydrolyzed cellulose acetate films at several pH values: A. (a) 0.1, (b) 1.1, (c) 1.4, (d) 2.0, (e) 2.6, (f) 3.4, (g) 4.2, (h) 4.7, (I) 5.4, (j) 6.0, (k) 6.3, (l) 6.6, (m) 6.9, and (n) 9.4; B. (a) 0.0, (b) 0.9, (c) 1.4, (d) 2.1, (e) 2.7, (f) 3.3, (g) 3.7, (h) 4.3, (I) 4.9, (j) 5.6, (k) 6.1, (l) 6.5, (m) 6.9, (n) 7.4, and (o) 9.5; C. (a) 1.0, (b) 1.5, (c) 2.0, (d) 2.5, (e) 3.0, (f) 3.5, (g) 4.5, (h) 5.5, (I) 6.0, (j) 6.5, (k) 7.0, (l) 7.5, and (m) 9.5.

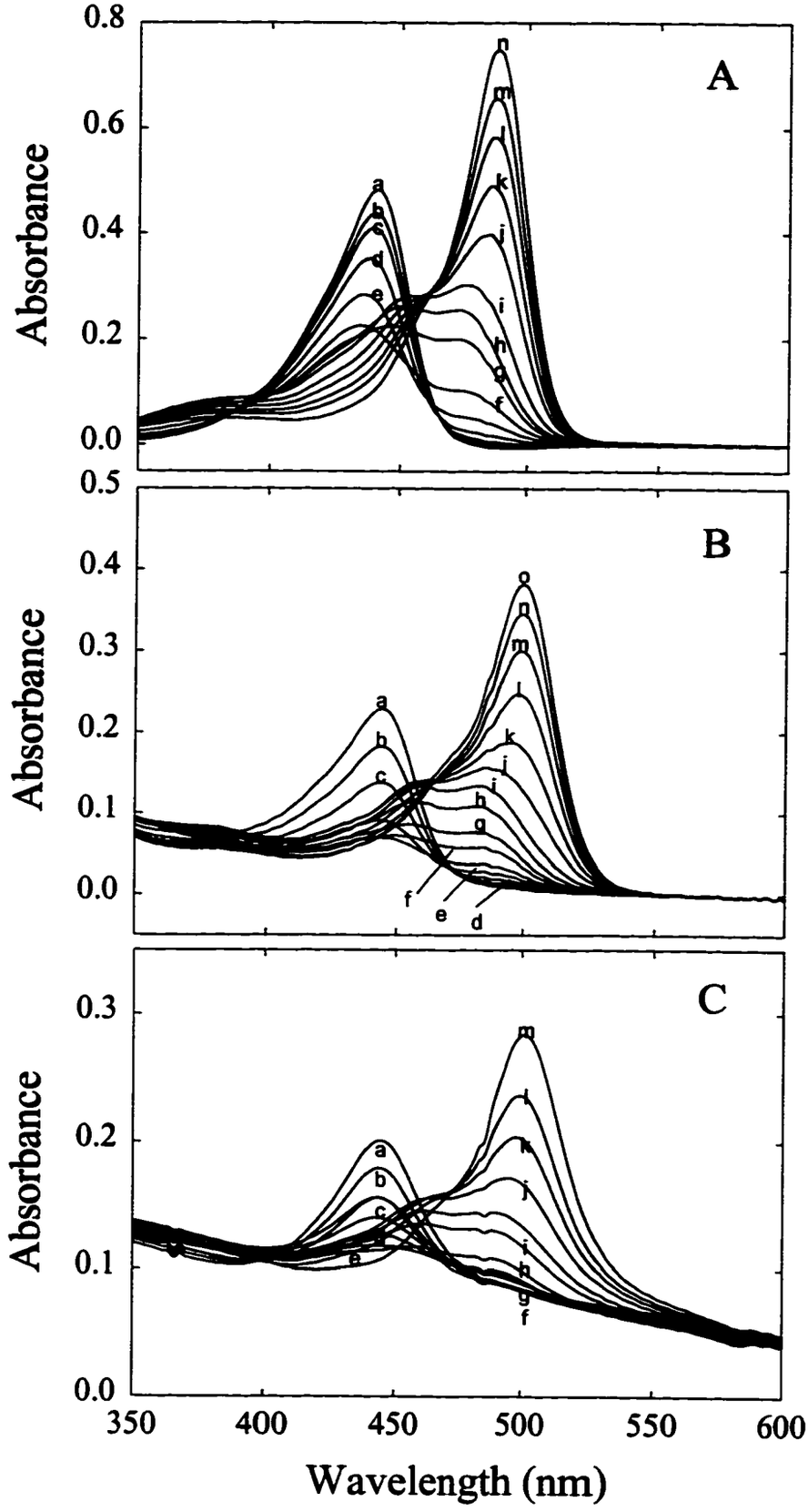
A
B
C
Absorbance
Absorbance
Absorbance
Wavelength (nm)
0.8
0.6
0.4
0.2
0.0
0.5
0.4
0.3
0.2
0.1
0.0
0.3
0.2
0.1
0.0
350
400
450
500
550
600

It has been assumed that the derivatization reactions of the fluorescein molecule have little effect on the indicator properties of the parent molecule, provided the xanthene ring remains unsubstituted.[20] Therefore, this result confirms that the immobilization occurred through the amino-group and that the parent molecule, which is responsible for the indicator properties,[19] was essentially unaffected by the immobilization procedure.

Dye losses due to bleeding and photobleaching present problems for sensor calibration stability if absolute absorbance measurements are used for pH determinations. This problem was minimized by utilizing an internal calibration scheme. An acid-base indicator which has strong chromophoric properties in its various reactive forms can be used to determine the pH of a solution by comparing the absorbance at two appropriate wavelengths. Figure 3 shows the absorbance change of fluoresceinamine solution at the absorption maximum of 440 and 488 nm as a function of pH. It can be seen that the absorbance at both wavelengths undergo extensive change with pH. At 440 nm, the absorbance falls rapidly as the pH increases from 0.12, reaches a minimum at pH 3.72, rises to a maximum at pH 5.12, and then falls to a constant value at pH 7.63. In contrast, the absorbance at 488 nm continuously increases as pH increases and reaches a steady value at pH 7.94. Based on these dependencies, the ratio of the absorbance at 488 nm to that at 440 nm (A_{488}/A_{440}) versus pH was utilized to calibrate the sensor. A typical calibration curve of the fluoresceinamine solution is presented in Figure 4. This calibration curve shows that fluoresceinamine responds to the pH change of the solution from pH 2 to 9, and that the pH 6-8 region is the most sensitive range.

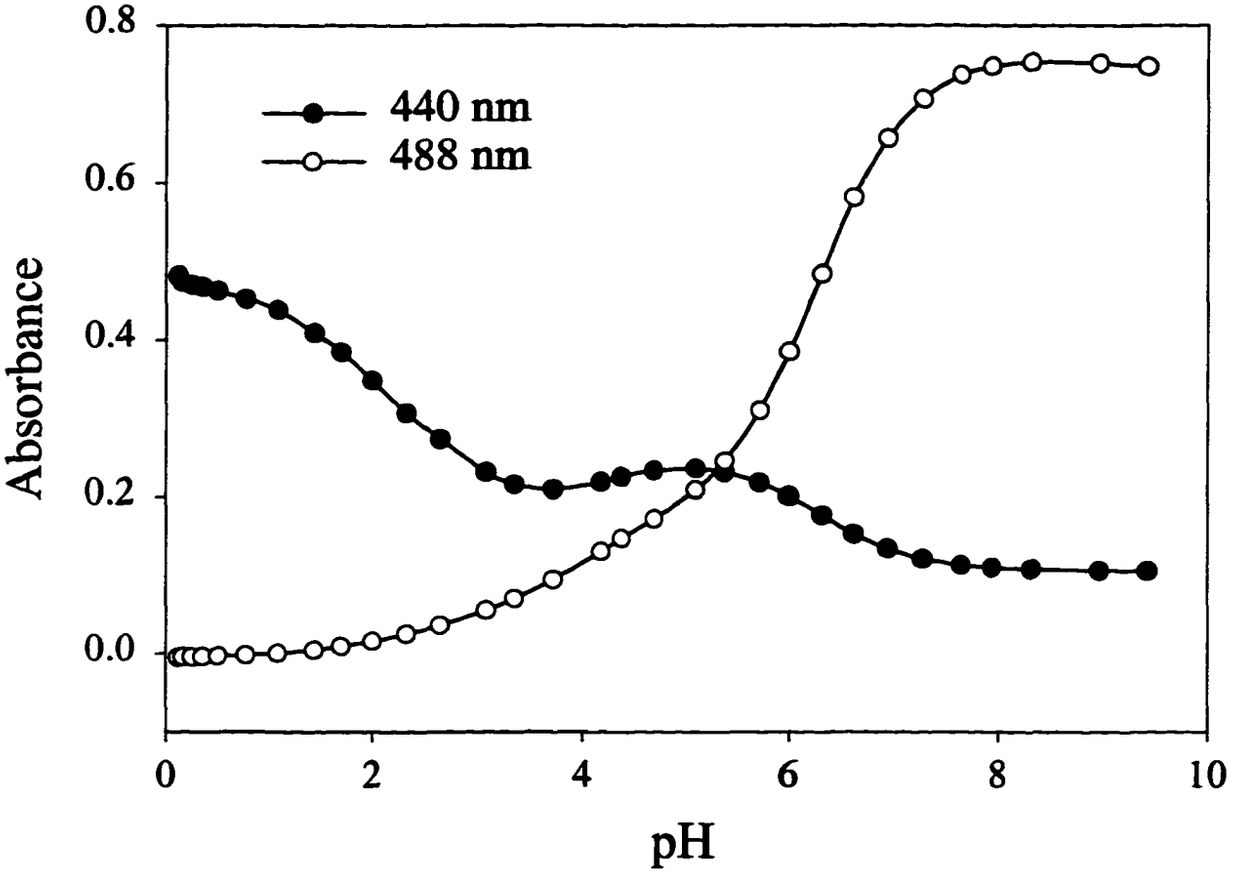

Figure 3. Absorbance change vs. pH at 440 and 488 nm for fluoresceinamine solution.

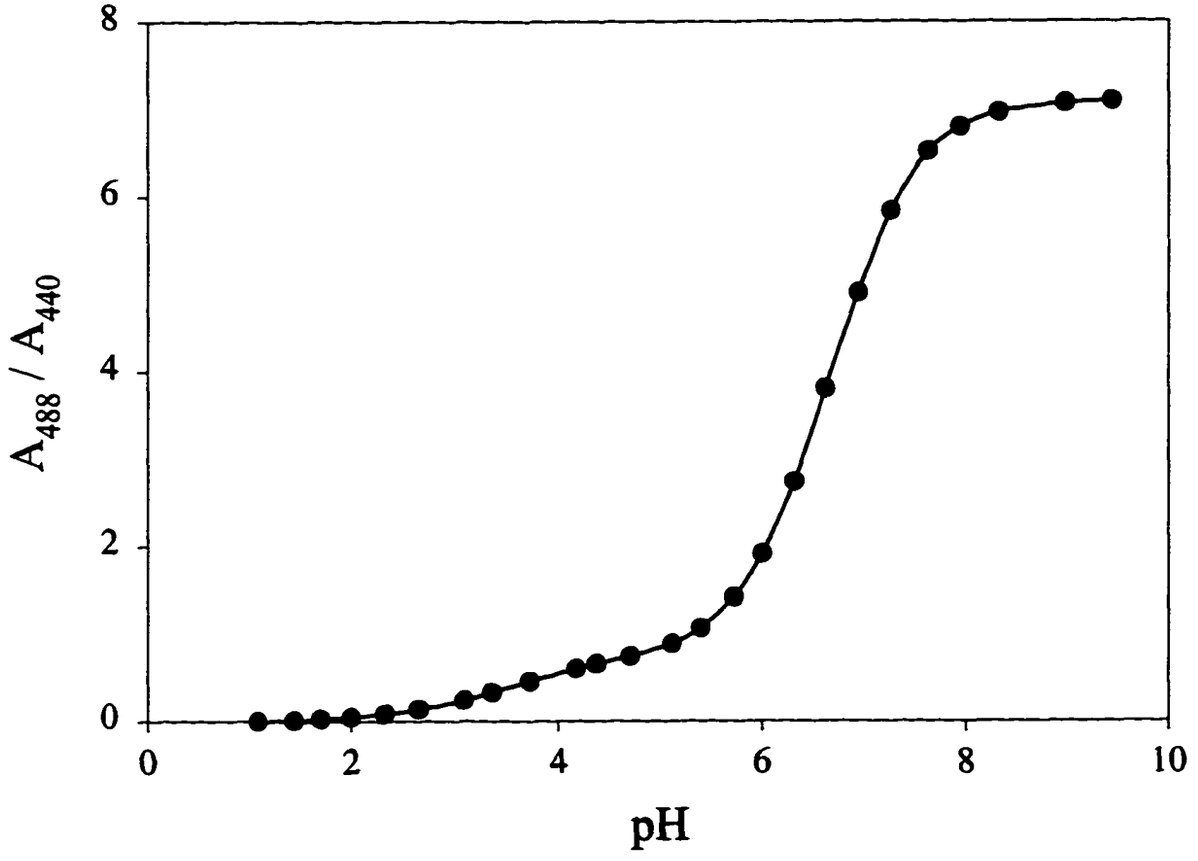

Figure 4. Absorbance ratio calibration curve for fluoresceinamine solution.

It is also important to note that the absorption spectra of the immobilized dye are red-shifted in comparison to those of its solution form, having a maximum at 444 and 499 nm at respective pH values of 0.0 and 9.5. This could be due in part to the different solvent environments before and after immobilization or the structural conformation changes of the dye after immobilization.

(ii) Response Time and Reversibility. The optical response to a rapid change in pH and reversibility of the sensor membranes are shown in parts A and B of Figure 5 for direct and indirect immobilization, respectively. The wavelength monitored for these measurements was 500 nm with the flow cell operating in a transmission configuration. The buffers of pH 2.0 and 10.2 were alternatively pumped through the flow cell. Both sensors respond rapidly to a change in pH. Equilibration (90% completion) is achieved in less than 30 s. For the directly immobilized fluoresceinamine sensor, the average equilibration time for three successive injections was 28 ±1 s when the pH was changed from 2.0 to 10.2 and 21 ±0.6 s when the pH was changed from 10.2 to 2.0. The indirectly immobilized fluoresceinamine sensor responds slightly faster to changes in pH, which was 23 ±2 s and 16 ±0.6 s, respectively.

It is noticed that both sensors showed a shorter response time when the solution was changed from base to acid than that of the other direction. This may be due in part to the faster diffusion of hydrogen ions into the polymer matrix from the solution relative to that of hydroxyl ions since the response time is mainly determined by the diffusion of ions through the polymer matrix. As expected, studies also indicate that reduction in film thickness results

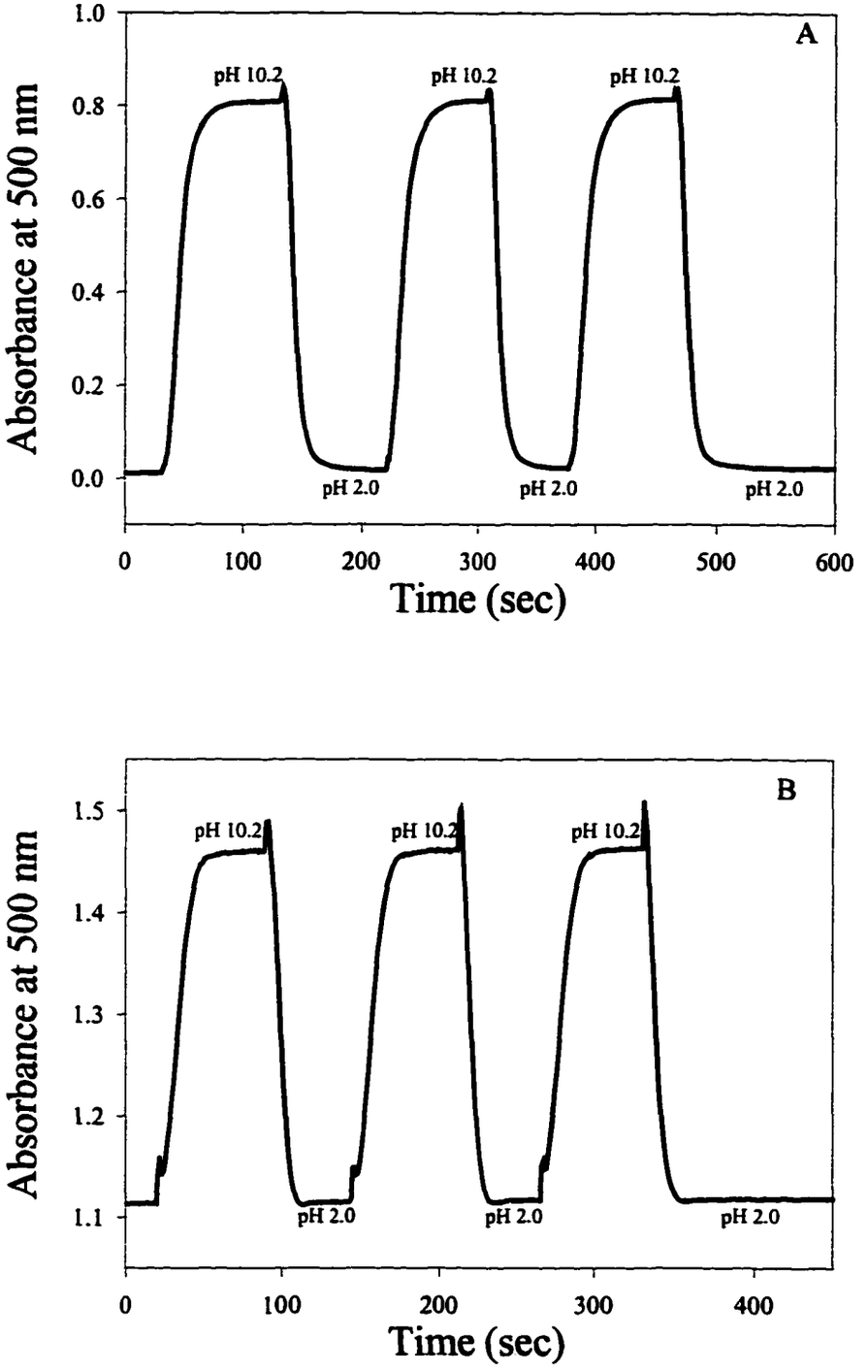

Figure 5. Dynamic response of the directly (A) and indirectly (B) immobilized fluoresceinamine sensors.

in faster response times.[14] The plots of Figure 5 indicate that the signal changes are fully reversible.

(iii) Effect of Ionic Strength and Temperature. The pH-dependence of the indicator films is affected by the ionic strength (IS) of the buffered solutions.[21] For example, by increasing the IS of a pH 8.0 buffer solution from 0.1 M to 0.5 M, the absorbance of the sensor in contact with this solution increases by ~30%. This is caused by a shift of the pK_a by ~0.43 units to a lower value as a result of increasing the IS. This IS anomaly cannot readily be distinguished from signal changes by pH and introduces an error common to most optical pH-sensors.

The temperature coefficient of the sensor film was measured in the flow cell by recording the response of the indicator dye while varying the temperature of buffered solutions between 5 °C and 40 °C. The temperature coefficient of the immobilized fluoresceinamine expressed as change of pH per °C temperature change was found to be 0.012 ± 0.003 pH units/°C over this temperature range.

(iv) Long-Term Stability. The long-term stability of the sensing membranes was examined by exposing the films to a buffer of pH 6.0 and monitoring the optical response for a period of two months. The change of the ratio of absorbance at 500 and 440 nm was plotted with time and the results are shown in Figure 6. For the sensor film with directly immobilized fluoresceinamine, the calibration ratio drifted slowly with time and the final value was ~89% of the original value after two months. There was a noticeable bleeding of the dye from the support. The absorbance at 500 and 440 nm decreased by 72% and 67%, respectively, after two months. The ratioing method minimizes these decreases to ~10%.

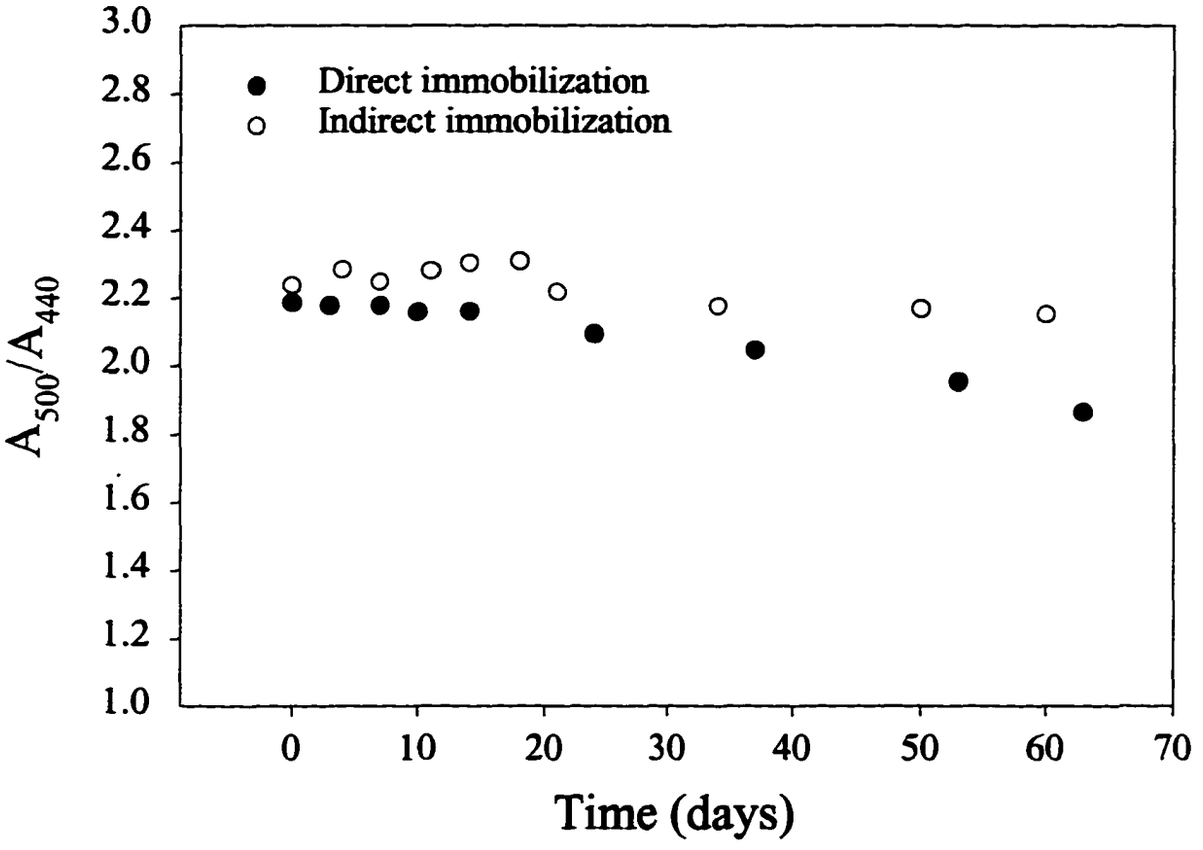

Figure 6. Long-term stability of the two pH sensors in a buffer with pH ~6.0.

For the indirectly immobilized fluoresceinamine sensor, there was no significant drift in the ratio and its value varied by < 2.5% during the two months. This exceptional stability is due to the strong covalent bond between the dye and the beads, and the strength and durability that the epoxy beads lend to the film.

(v) Metal-Ion Interference. The interference of metal ion complexation with the optical response of the sensor was examined for Na^+, Li^+, Mg^{2+}, Ca^{2+} and Mn^{2+}. The absorbance spectra for each metal ion were taken while maintaining a constant pH (~9) with buffered solutions. No significant spectral shifts were observed when compared with spectra taken of a buffered blank solution.

(vi) Fluorescence Properties of the Sensors vs. pH. Fluorescein is used in many applications because of its pH sensitivity and high fluorescence quantum yield.[22] Fluoresceinamine, however, has a markedly quenched fluorescence due to the excited-state electron transfer from inter- and intramolecular amines.[20, 23] The titration of fluorescein and fluoresceinamine aqueous solutions as a function of fluorescence emission intensity are shown in part A and B of Figure 7, respectively. The emission intensity of fluoresceinamine solution is ~two orders of magnitude lower than that of fluorescein of the same concentration. The changes in the titration curve of fluoresceinamine reflect the influence of the nitrogen electron pair on the fluorescence of the molecule. Earlier work indicated that the quenching process can be reversed by either covalent bonding or electrostatic processes.[24, 25] Thus, fluorescence properties of immobilized fluoresceinamine were also studied and the results are shown in A and B of Figure 8 for the direct and indirect immobilization techniques, respectively. These results show that after immobilization, the quenching is not

Figure 7. Fluorescence titrations of fluorescein (A) and fluoresceinamine (B) solution. Concentrations (10^{-5} M) and excitation energies were identical; $\lambda_{exc} = 490$ nm, $\lambda_{em} = 520$ nm.

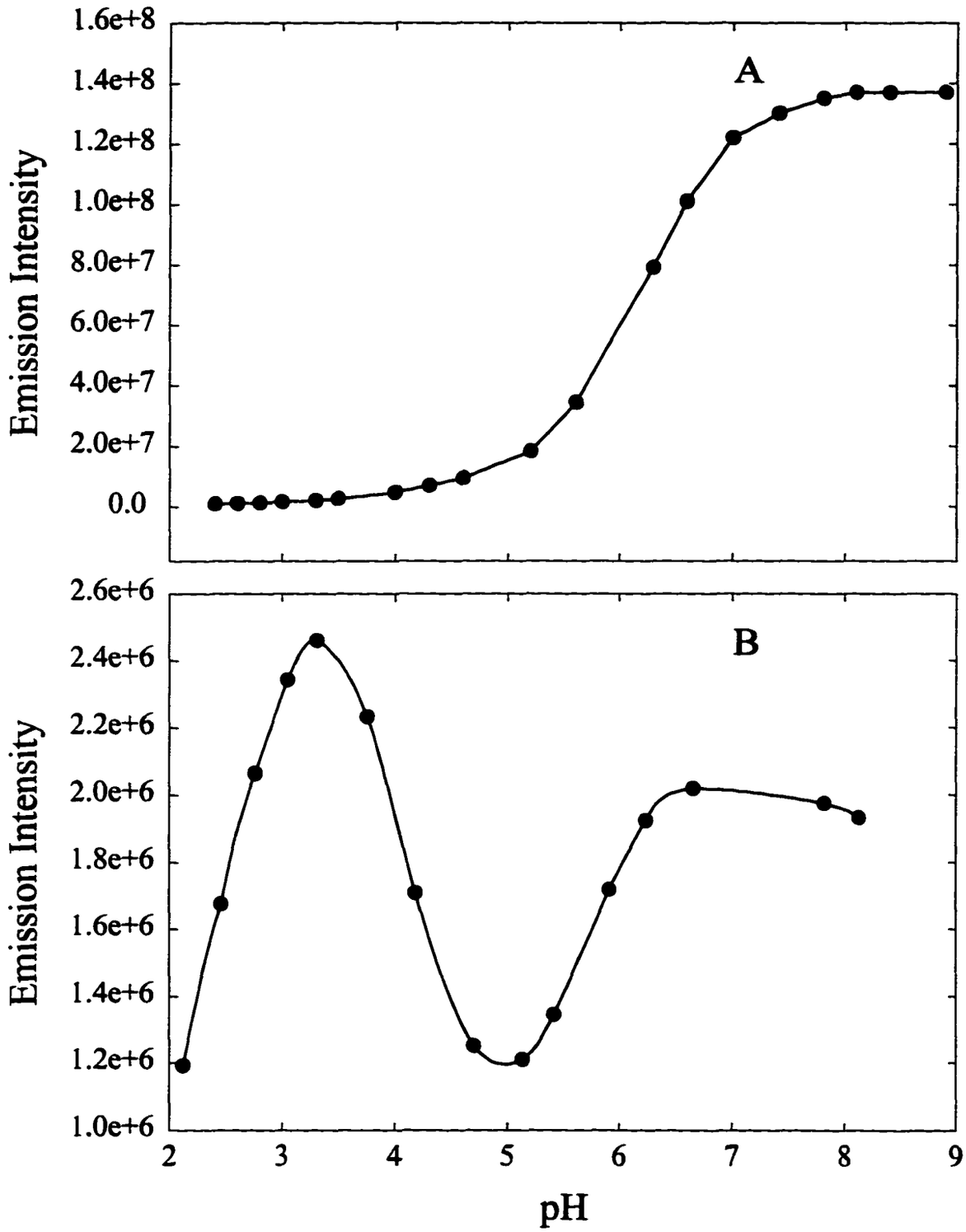
A
B
Emission Intensity
Emission Intensity
1.6e+8
1.4e+8
1.2e+8
1.0e+8
8.0e+7
6.0e+7
4.0e+7
2.0e+7
0.0
2.6e+6
2.4e+6
2.2e+6
2.0e+6
1.8e+6
1.6e+6
1.4e+6
1.2e+6
1.0e+6
2
3
4
5
6
7
8
9
pH

Figure 8. Fluorescence titrations of directly (A) and indirectly (B) immobilized fluoresceinamine sensors. λ_{exc} = 500 nm, λ_{em} = 520 nm.

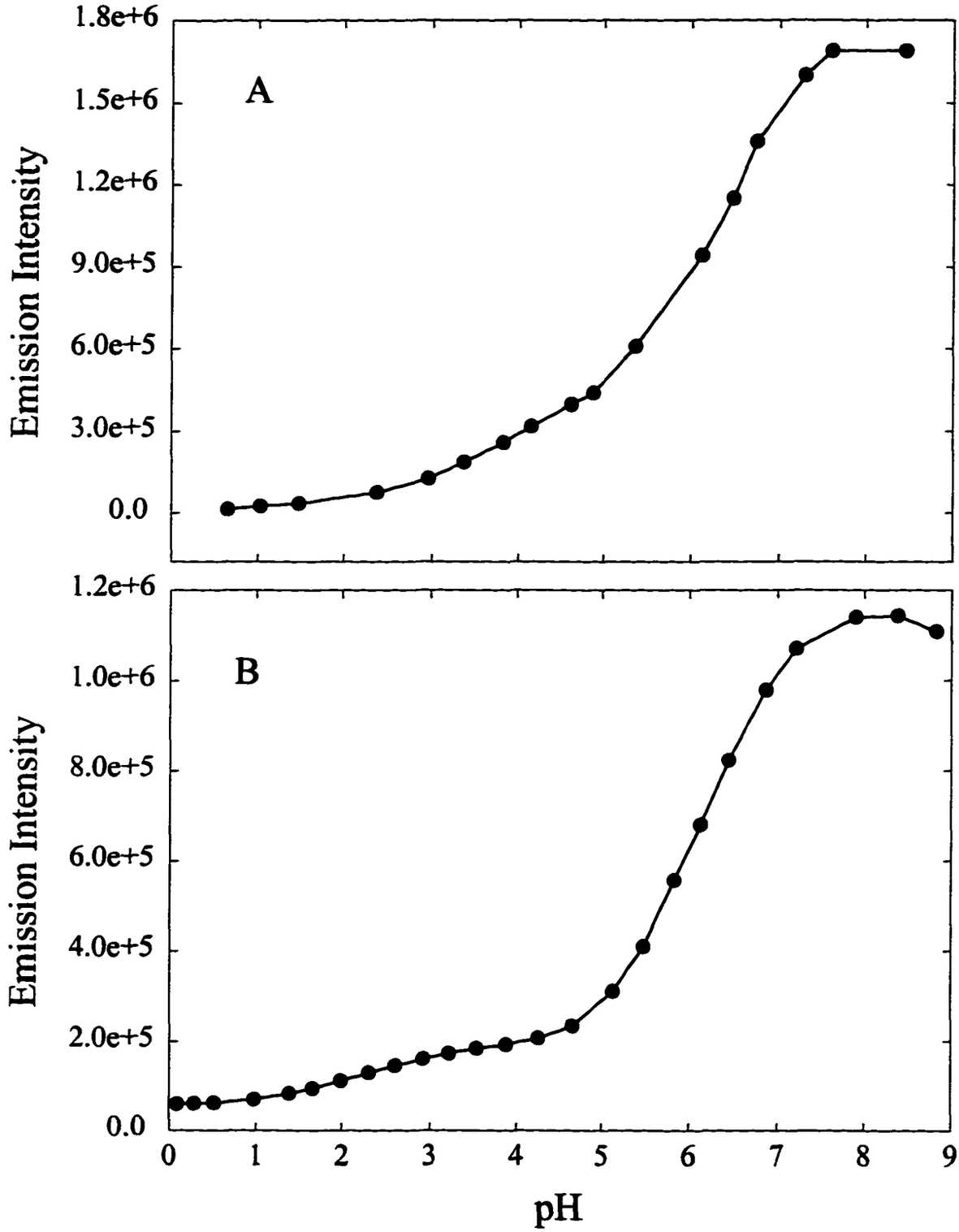
A
B
Emission Intensity
Emission Intensity
1.8e+6
1.5e+6
1.2e+6
9.0e+5
6.0e+5
3.0e+5
0.0
1.2e+6
1.0e+6
8.0e+5
6.0e+5
4.0e+5
2.0e+5
0.0
0
1
2
3
4
5
6
7
8
9
pH

observed and the emission intensity shows a similar spectral profile to pH change as that for fluorescein. These results provide evidence that fluoresceinamine is covalently immobilized via the amine group during the direct and indirect immobilization process.[8]

Multiple-Component pH Sensor. The goal of our research was to co-immobilize several different dyes at a hydrolyzed cellulose acetate film for the construction of a pH sensor which would exhibit a broad response, i.e., something akin to "optically transparent litmus paper." Earlier work in our group examined a pH sensor based on the immobilization of Congo Red with a dynamic range of pH 0 to 5.[26] In order to expand the pH dynamic range of a single-component sensor, a multi-component pH sensor based on the co-immobilization of Congo Red and fluoresceinamine (1:10 molar ratio) was constructed using the direct immobilization scheme. The absorption spectra of this film is shown in Figure 9. It can be seen that at acidic pH, the absorbance at 600 nm, which corresponds to the acidic forms of Congo Red, changes with pH, which means that Congo Red was the one that was effective at this pH range. When pH is above 5.0, the absorbance at 500 nm, which corresponds to the basic forms of fluoresceinamine, started to increase with pH. The calibration curves for this two-component pH sensor is shown in Figure 10. The ratio of the absorbance at 600 nm to that of 526 nm was used for pH range of 0.0-4.5, while A_{500}/A_{440} was used for pH 4.5-9.0. Thus, the pH dynamic range was expanded to 9 pH units through co-immobilization of Congo Red and fluoresceinamine.

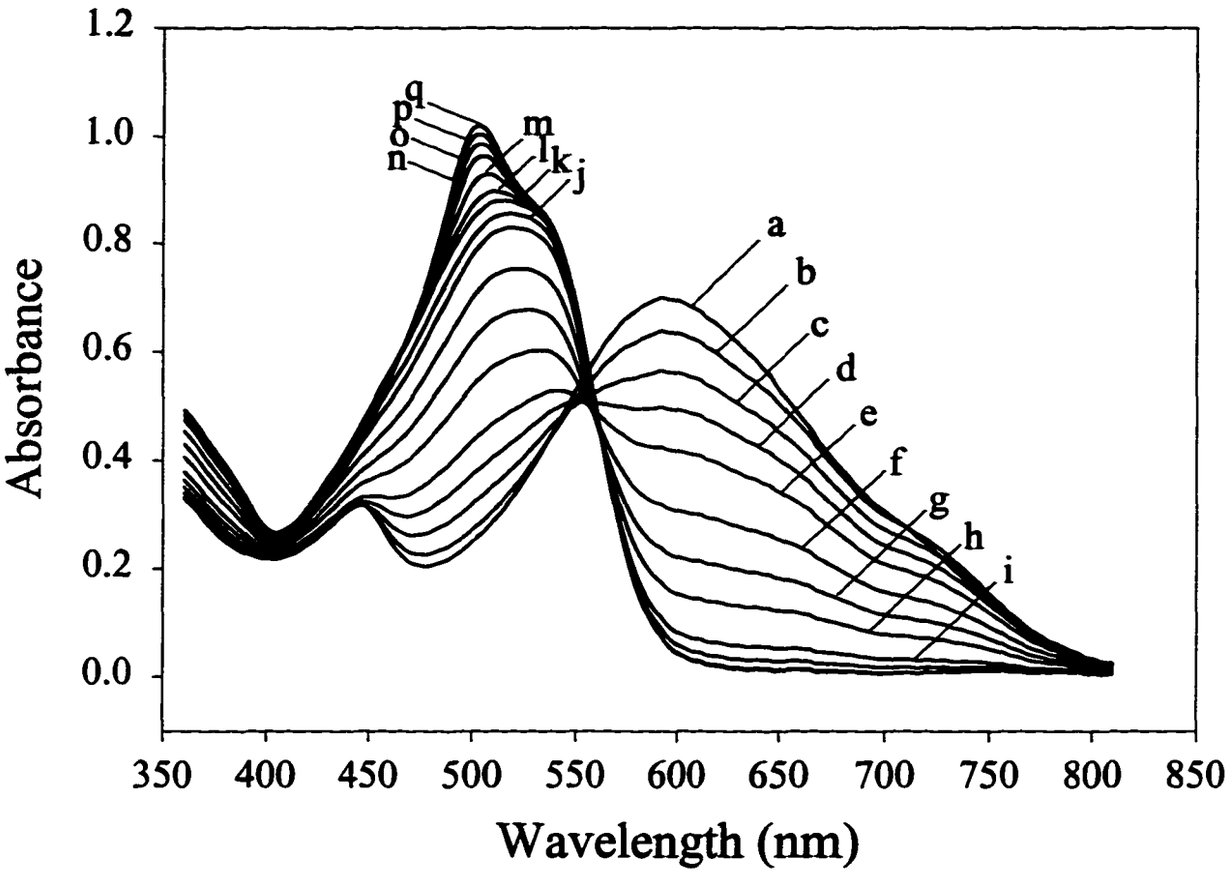

Figure 9. Absorption spectra for the co-immobilized Congo Red-fluoresceinamine pH sensor at several pH values: (a) 0.0, (b) 0.5, (c) 1.2, (d) 1.5, (e) 1.9, (f) 2.3, (g) 2.7, (h) 3.1, (I) 3.5, (j) 3.9, (k) 5.1, (l) 5.6, (m) 6.1, (n) 6.6, (o) 7.0, (p) 7.6, and (q) 9.0.

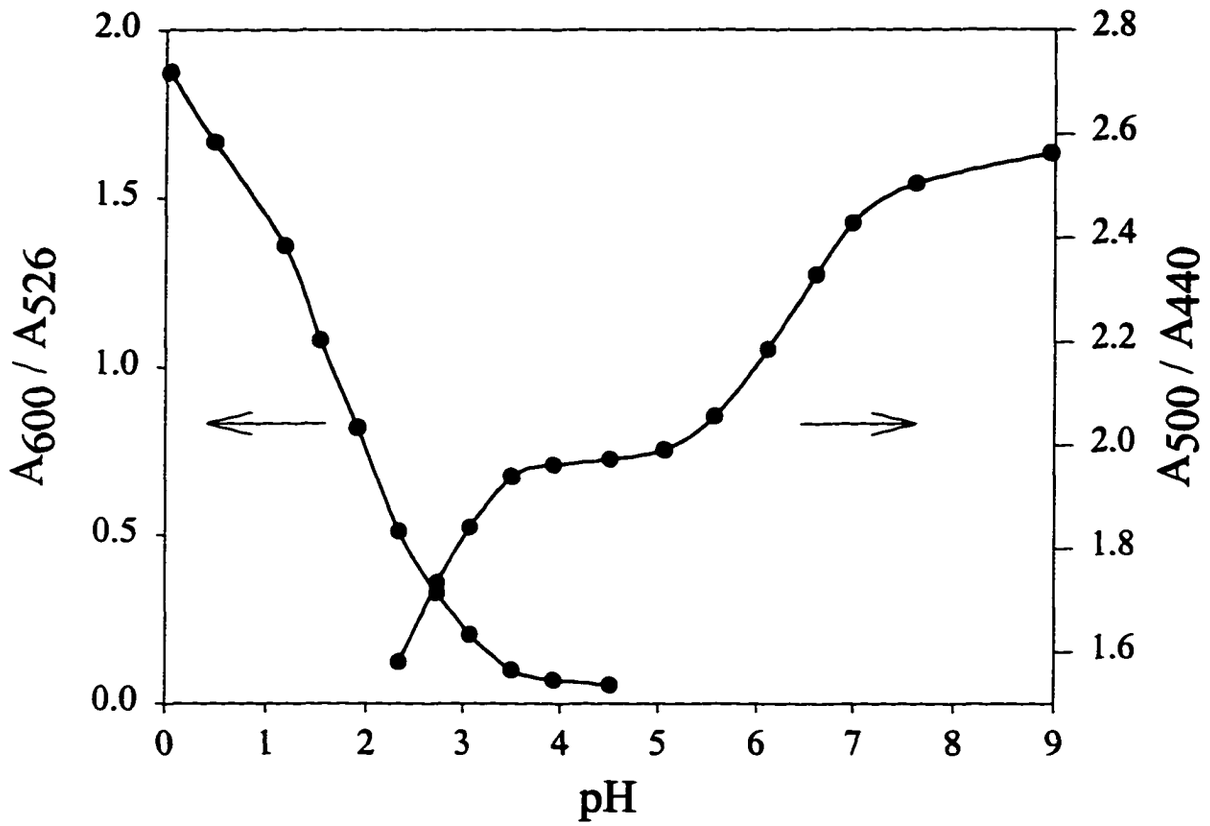

Figure 10. Absorbance ratio calibration curve for Congo Red - fluoresceinamine pH sensor.

Conclusions

This study has demonstrated that the pH sensors based on the covalent immobilization of fluoresceinamine at hydrolyzed cellulose acetate film showed a rapid response time, a large dynamic range and relatively exceptional long-term stability. The immobilization schemes are both simple and free of organic solvents. Compared with the indirect immobilization scheme, the direct immobilization procedure is simpler, and the large background due to light scattering by the beads is minimized. However, the sensor film prepared through the indirect immobilization scheme shows better mechanical strength and provides better long-term stability than the one that was prepared through the direct immobilization scheme, and the indirect immobilization technique is less hazardous than the direct immobilization technique. Temperature dependence can be compensated by applying the temperature coefficient, which can be calibrated for each individual sensor. The pH sensitivity of the sensor was further extended to ~9 pH units through co-immobilization of Congo Red and fluoresceinamine at a porous cellulosic film using the direct immobilization technique. Future work includes identifying additional indicators which can be co-immobilized with fluoresceinamine and Congo Red to extend the pH dynamic range of the sensor to higher pH values, and examining schemes for compensating ionic strength dependence.

Acknowledgments

The authors would like to expresses appreciation for the support of a NASA/Iowa Space Grant Fellowship given to Shelley Coldiron through the College Consortium under the

NASA Space Grant Program. Also, this work was supported in part by the Center for Advanced Technology Development at Iowa State University under USDOC Grant ITA 87-02, by the Office of Basic Energy Research-Chemical Sciences Division of USDOE, ISCO, and the Microanalytical Instrumentation Center of Iowa State University. The Ames Laboratory is operated for the U.S. Department of Energy by Iowa State University under Contract No. W-7405-eng-82.

References

(1) Healey, B. G.; Walt, D. R. *Anal. Chem.* **1997,** *69*, 2213-2216.

(2) Bronk, K. S.; Walt, D. R. *Anal. Chem.* **1994,** *66*, 3519-3520.

(3) Cardwell, T. J.; Cattrall, R. W.; Deady, L. W.; Dorkos, M.; O'Connell, G. R. *Talanta* **1993,** *40*, 765-768.

(4) Parker, J. W.; Laksin, O.; Yu, C.; Lau, M. L.; Klima, S.; Fisher, R.; Scott, I.; Atwater, B. W. *Anal. Chem.* **1993,** *65*, 2329-2334.

(5) Werner, T.; Wolfbeis, O. S. *Fresenius J Anal Chem* **1993,** *346*, 564-568.

(6) Tan, W. H.; Shi, Z. Y.; Kopelman, R. *Anal. Chem.* **1992,** *64*, 2985-2990.

(7) Fuh, M. R. S.; Burgess, L. W.; Hirschfeld, T.; Christian, G. D. *Analyst* **1987,** *112*, 1159-1163.

(8) Saari, L. A.; Seitz, W. R. *Anal. Chem.* **1982,** *54*, 821-823.

(9) Peterson, J. I.; Vurek, G. G. *Science* **1984,** *224*, 123-125.

(10) Zhang, Z.; Seitz, W. R. *Anal. Chim. Acta* **1985,** *171*, 47-55.

(11) Offenbacher, H.; Wolfbeis, O. S.; Furlinger, E. *Sensors and Actuators* **1986,** *9*, 73-84.

(12) Munkholm, C.; Walt, D. R.; Milanovich, F. P.; Klainer, S. M. *Anal. Chem.* **1986,** *58*, 1427-1430.

(13) Jordan, D. M.; Walt, D. R. *Anal. Chem.* **1987,** *59*, 437-439.

(14) Stole, S. M.; Jones, T. P.; Chau, L. K.; Porter, M. D. In *Chemical Sensors and Microinstrumentation*; Murray, R. W., Dessy, R. E., Heineman, W. R., Janata, J., Seitz, W. R., Eds.; American Chemical Society, 1989; Vol. 403, pp 283-302.

(15) Axén, R.; Ernback, S. *Eur. J. Biochem.* **1971,** *18*, 351-360.

(16) Kohn, J.; Wilchek, M. *Enzyme Microb. Technol.* **1982,** *4*, 161-163.

(17) Porter, M. D.; Coldiron, S. J.; Vaidya, B. *SAE Technical Paper Series* **1993,** *932207*, 1-5.

(18) Burg, K.; Mauz, O.; Noetzel, S.; Sauber, K. *Die Angewandte Makromolekulare Chemie* **1988,** *157*, 105-121.

(19) Diehl, H.; Morris, N. H. *Talanta* **1987,** *34*, 739-741.

(20) Munkholm, C.; Parkinson, D.-R.; Walt, D. R. *J. Am. Chem. Soc.* **1990,** *112*, 2608-2612.

(21) Wolfbeis, O. S.; Rodriguez, N. V.; Werner, T. *Mikrochim. Acta* **1992,** *108*, 133-141.

(22) Martin, M. M.; Lindqvist, L. *Journal of Luminescence* **1975,** *10*, 381-390.

(23) Okada, T.; Fujita, T.; Kubota, M.; Masaki, S.; Mataga, N. *Chemical Physics Letters* **1972,** *14*, 563-568.

(24) Blough, N. V.; Simpson, D. J. *J. Am. Chem. Soc.* **1988,** *110*, 1915-1917.

(25) Huston, M. E.; Haider, K. W.; Czarnik, A. W. *J. Am. Chem. Soc.* **1988,** *110*, 4460-4462.

(26) Jones, T. P.; Porter, M. D. *Anal. Chem.* **1988,** *60*, 404-406.

CHAPTER 2. NANOSCALE IN-SITU MONITORING OF THE BASE-HYDROLYSIS OF A DITHIO-BIS(SUCCINIMIDYLUNDECANOATE) MONOLAYER AT GOLD USING SCANNING FORCE MICROSCOPY (SFM)

A paper to be submitted to *Langmuir*

Jianhong Wang, Jeremy R. Kenseth, Vivian W. Jones, and Marc D. Porter

Abstract

This paper demonstrates the in situ monitoring of the chemical transformation of a surface-bound species using SFM-based compositional mapping. The base-catalyzed hydrolysis of a dithio-bis(succinimidylundecanoate) (DSU) monolayer chemisorbed at a Au(111) surface was followed under aqueous base (10 mM KOH) with SFM using an unmodified Si_3N_4 probe tip. With this tip-sample combination, the conversion of the ester group to an immobilized carboxylate ion results in an increase in the friction at the microcontact formed by the two different surfaces. Using surface tension arguments, this change is attributed to the increase in the effective miscibility at the microcontact as a consequence of the transformation of the ester group to the carboxylate ion. Issues related to the study of the microscopic surface reactivities and a comparison of the macroscopic and the microscopic data are discussed.

Introduction

The scanning force microscope (SFM) has been increasingly used in studying the surface structures of a wide variety of materials.[1-3] Recent efforts in several laboratories,[4-15] including our own,[16-18] have focused on extending the capabilities of SFM to increase the chemical content gained from the imaging process. Several approaches have been explored, including the use of SFM in its friction and adhesion modes as probes of the compositional transformations of interfaces at nanometer length scales. The underlying basis of these approaches is the dependence of both the adhesive and frictional interactions of the chemical functional groups at the outermost few angstroms of the two surfaces that form the microcontact. Compositional maps of a variety of chemically[10-12, 16] and biochemically[19-22] important interfaces have been developed, with a spatial resolution as high as 10 nm.[16]

In this paper, we demonstrate the application of SFM-based compositional mapping to the in situ monitoring of the chemical transformation of a surface-bound species. The base-catalyzed hydrolysis of a dithio-bis(succinimidylundecanoate) (DSU) monolayer chemisorbed at a Au(111) substrate was followed under aqueous base (10 mM KOH) with SFM using an unmodified Si_3N_4 probe tip. With this tip-sample combination, we show that changes in the friction are the result of the transformation of an ester end group to a carboxylate end group during the hydrolysis of DSU. We also explore the application of SFM as an analytical technique to study the microscopic reactivities of the surface. The macroscopic data obtained with infrared reflection spectroscopy (IRS) and the microscopic data obtained by SFM are also compared.

Experimental Section

Sample Preparation. Substrates were prepared by the deposition of 300 nm of gold onto freshly cleaved mica sheets. The gold-coated substrates were then annealed in an oven at 300 °C for 5 h. This processing results in a film with a predominant Au(111)-surface crystallinity.[16]

The monolayer samples were formed by the immersion of the Au(111) substrates into a dilute (0.1 mM) ethanolic solution of DSU for 24 h. Upon removal from solution, the samples were rinsed thoroughly with ethanol and dried in air. The synthesis of DSU followed literature procedures[23, 24] and will be detailed elsewhere.[25]

Instrumentation. (i) Scanning Force Microscopy (SFM). A MultiMode Nanoscope III atomic force microscope (AFM) (Digital Instruments, Santa Barbara, CA) that was equipped with a 12 μm scanner and an SFM fluid cell was utilized. All images were collected with the sample mounted in the fluid cell under liquid at room temperature (23±2 °C) and scanned relative to a stationary tip. The force constant of the triangular Si_3N_4 cantilevers (Digital Instruments) for normal bending was ~0.06 N/m and for torsional bending was ~80 N/m.[16] Unless noted otherwise, all images (512 x 512 pixels) were collected in situ in either 10 mM KOH or in deionized water (pH 6.2) in the constant force mode at a load of ~25 nN and scan rate of 10.2 Hz. Topographic and lateral force images were collected concurrently. The instrument was allowed to equilibrate thermally under water (pH ~6.2) for ~3 h after mounting the sample. Vertical displacements were calibrated using the heights of single atomic steps at Au(111).

(ii) Infrared Reflection Spectroscopy (IRS). The progression of the base-hydrolysis of the DSU monolayers at Au(111) was determined using IRS. Ex situ infrared reflection spectra of the samples were acquired with a Nicolet 750 FT-IR interferometer following immersion into a 10 mM KOH solution for varied periods of time. The emersed samples were rinsed with ethanol prior to mounting in the spectrometer. Monolayer spectra were obtained using *p*-polarized light incident at 82° with respect to the surface normal and are reported as $-\log(R/R_0)$, where R is the reflectance of the sample and R_0 is the reflectance of a "reference" octadecanethiolate-d_{37} monolayer on a Au coated substrate. All spectra are the average of 512 scans of both the sample and reference, and were collected at 2-cm^{-1} resolution (one level zero-filled) with Happ-Genzel apodization. A liquid N_2 cooled HgCdTe detector was used. The spectrometer and sample chamber were purged with boil-off from liquid N_2.

Reagents. Absolute ethanol (Quantum) and KOH (Aldrich, 99.99%) were used as received. Dithio-bis(succinimidylundecanoate) was synthesized based on earlier reports.[23, 24]

Results and Discussion

Infrared Reflection Spectroscopy (IRS). (i) General Observations. Scheme 1 shows idealized molecular architectures for the base-hydrolyzed transformation of a DSU monolayer at Au(111). Upon exposed to an alkaline solution, the ester functionality of DSU is converted to an immobilized carboxylate functionality with N-hydroxysuccinimide (NHS) as the solubilized leaving group. As a starting point, the composition of the DSU monolayer at Au(111) was characterized using IRS, and the resulting spectrum is presented in Figure

Scheme 1

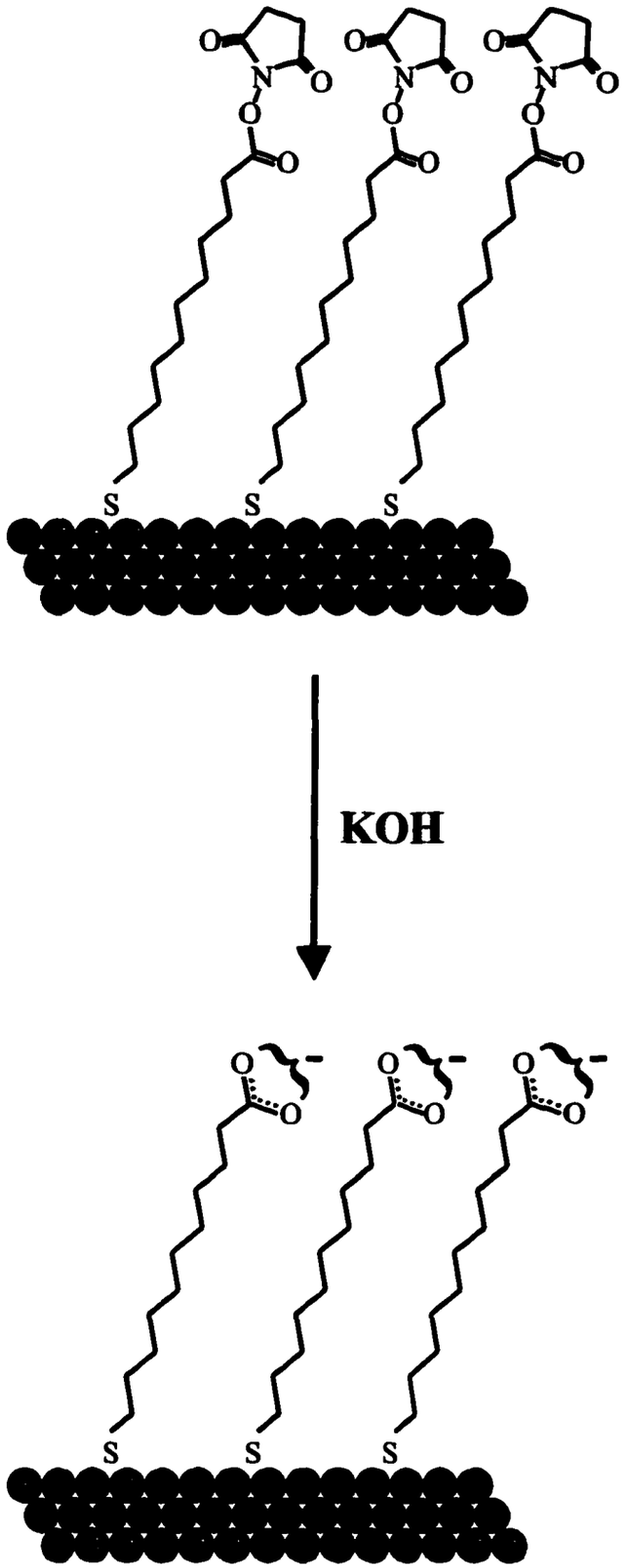

1A. For comparison, the spectrum for DSU dispersed in KBr and determined via measurements is presented in Figure 1B. Peak positions and mode assignments for Figure 1 are listed in Table 1, and are based, in part, on earlier studies.[26] Spectrum A exhibits the characteristic asymmetric ($\nu_a(CH_2)$) and symmetric ($\nu_s(CH_2)$) methylene stretching modes of the polymethylene spacer chain at 2920 and 2850 cm^{-1}, respectively. These frequencies are similar to those observed for *n*-alkanethiolate monolayers at Au(111),[27] where the chains are reasonably well ordered.[27] However, these positions are slightly higher in energy (i.e., 2-4 cm^{-1}) than found for longer chain n-alkanethiolate monolayer, suggesting a lower, but not quantifiable ordering of the chains.[27]

Table 1. Peak Positions and Mode Assignments for Dithio-Bis(succinimidylundecanoate) in KBr and Chemisorbed at Au(111)

	Peak Positions (cm^{-1})	
Mode Assignment	in KBr	at gold
asymmetric CH_2 C-H stretch ($\nu_a(CH_2)$)	2923	2920
symmetric CH_2 C-H stretch ($\nu_s(CH_2)$)	2852	2850
asymmetric stretch of the NHS carbonyls ($\nu_a(C=O)$)	1820	1817
symmetric stretch of the NHS carbonyls ($\nu_s(C=O)$)	1788	1788
carbonyl stretch of the ester ($\nu(C=O)$)	1743, 1728	1752
symmetric CNC stretch ($\nu_s(C-N-C)$)	1370	1379
asymmetric CNC stretch ($\nu_a(C-N-C)$)	1210	1218
NCO stretch ($\nu(N-C-O)$)	1071	1077

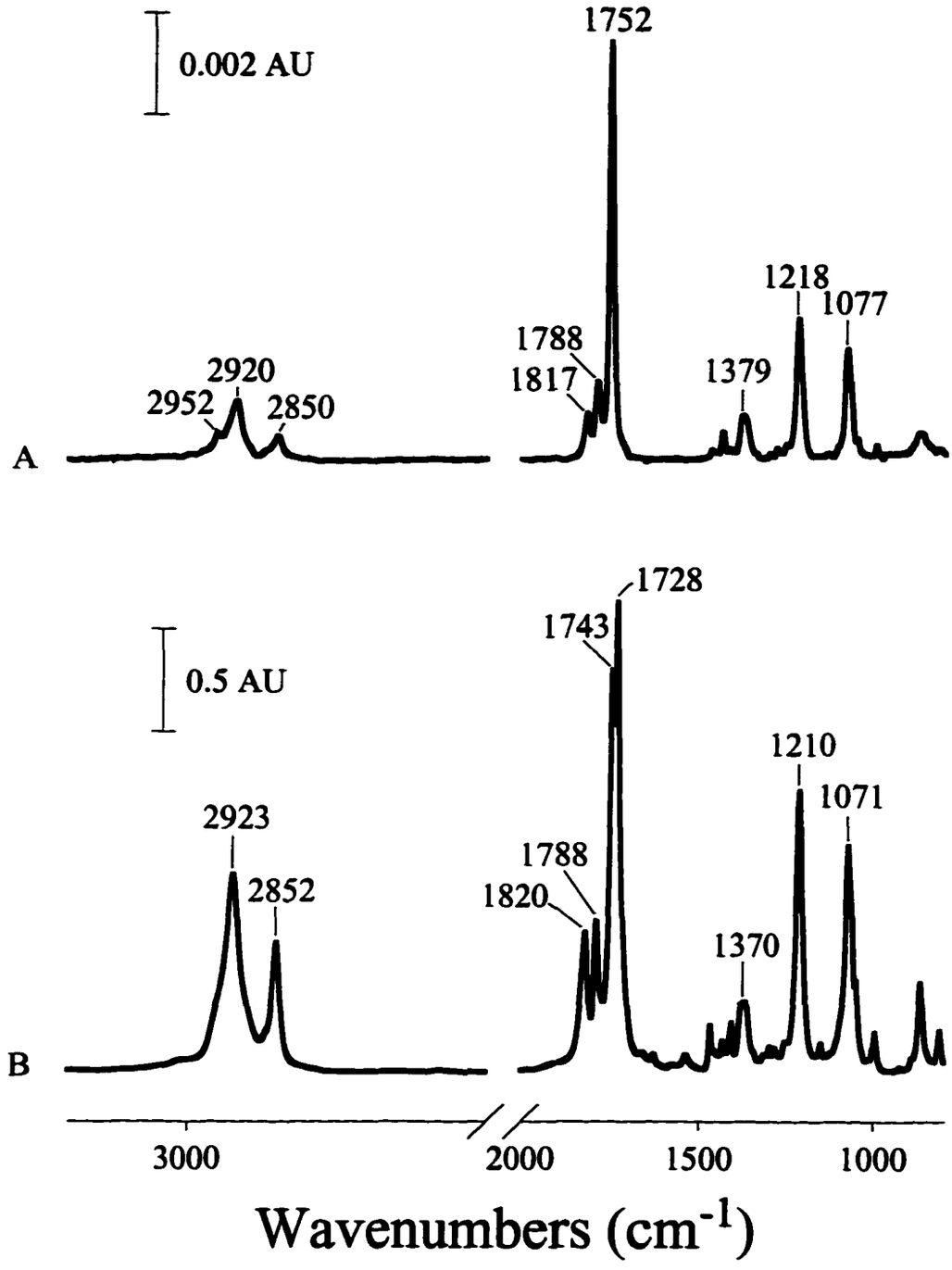

Figure 1. IR spectra of a DSU monolayer at Au(111) (A) and dispersed in KBr pellet (B).

The spectrum also shows the symmetric (ν_s(C=O)) and asymmetric (ν_a(C=O)) stretch of the NHS carbonyl groups at 1788 and 1817 cm^{-1}, respectively. The carbonyl stretching mode of the ester linkage appears at 1752 cm^{-1}. Figure 1B shows similar band frequencies for the symmetric and asymmetric stretch of the NHS carbonyl groups at 1788 and 1821 cm^{-1}, respectively, but a double peak at 1743 and 1728 cm^{-1} for the carbonyl stretch of the NHS ester. The high frequency feature at 1743 cm^{-1} is attributed to free, non-hydrogen-bonded NHS esters, whereas the feature at 1728 cm^{-1} reveals the presence of a side-to-side dimeric structure usually found in hydrogen-bonded esters. The absence of the low-energy band and the shift of the carbonyl stretch for the ester moiety from 1744 to 1752 cm^{-1} indicates that there is less interaction between neighboring ester groups of the monolayer, which we attribute to the packing limitation imposed by the bulky end group. Taken together the strong similarities of the features in both spectra indicates that a monolayer of DSU is formed on the gold substrate.

Figures 2A-H show the IRS spectra obtained after the DSU monolayer was immersed into an alkaline (10 mM KOH) aqueous solution for 0, 10, 20, 30, 40, 50, 60 and 70 min, respectively. The spectra show that as the immersion time increases, the magnitudes of the NHS carbonyl bands at 1817 and 1788 cm^{-1} decrease, whereas the magnitudes of the symmetric and asymmetric stretches of the carboxylate modes at 1446 cm^{-1} and 1590 cm^{-1}, respectively, increase. These changes are diagnostic of the hydrolysis of the terminal succinimidyl ester moieties of the DSU monolayer to an immobilized carboxylate species. Furthermore, the process requires more than 2 h to approach completion.

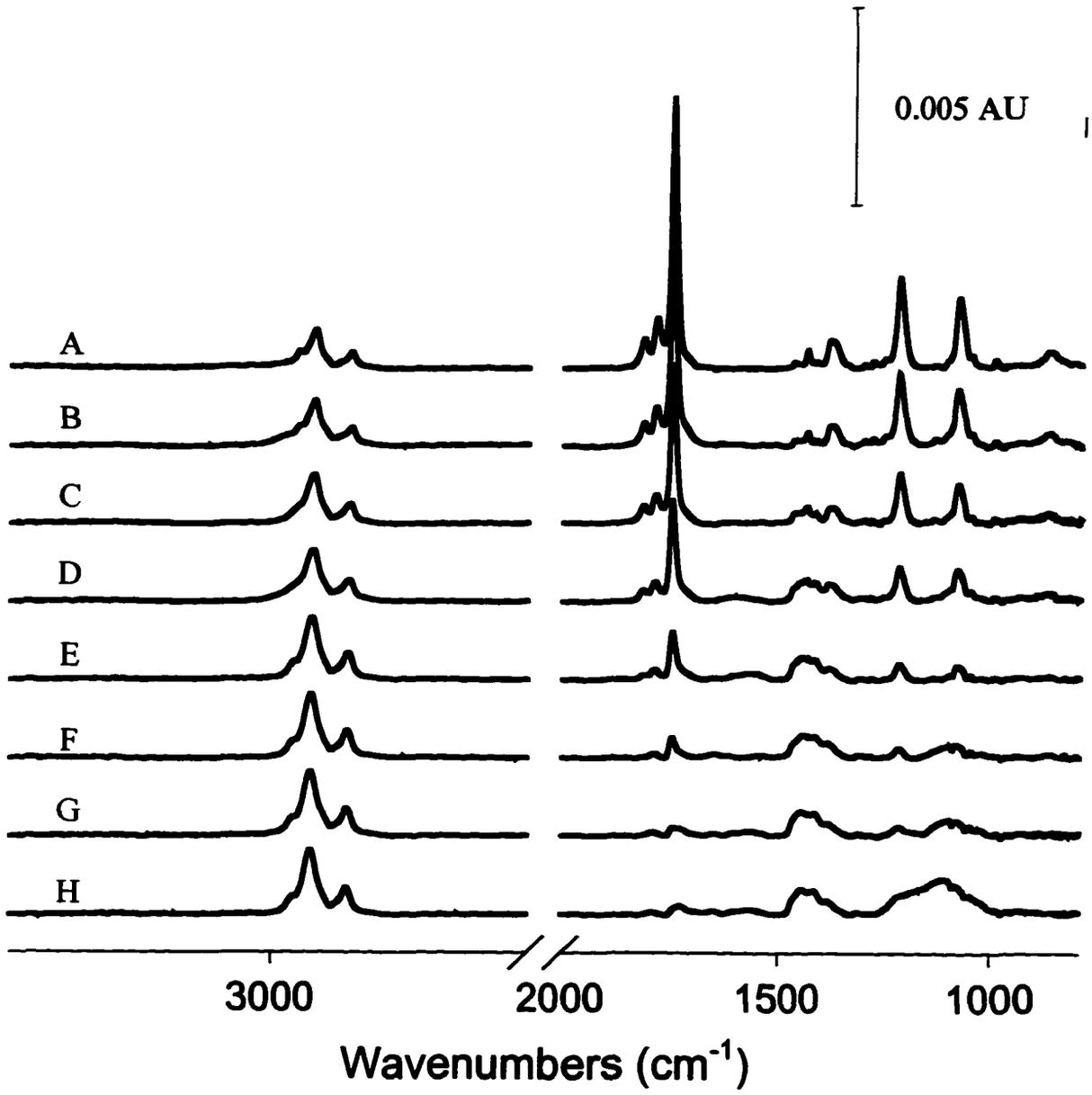

Figure 2. Ex situ IRS spectra of a DSU monolayer at Au(111) in aqueous 10 mM KOH: A) 0 min; B) 10 min; C) 20 min; D) 30 min; E) 40 min; F) 50 min; G) 60 min; and H) 70 min.

The data also show that both the symmetric and asymmetric methylene stretching modes of the polymethylene spacer chain gradually shift towards higher energy during hydrolysis, i.e., from 2850 and 2920 cm^{-1} before hydrolysis to 2858 and 2926 cm^{-1} after 70 min immersion, respectively. There is an increase of ~65% for the $\nu_s(CH_2)$ and ~54% for the $\nu_a(CH_2)$ in magnitude after 70 min of immersion in 10 mM KOH. These changes indicate evolution towards a higher degree of disorder in the chain structure of the adlayer as the extent of hydrolysis increases. This disordering reflects the increase in void volume as the bulky succinimidyl group is transformed to the smaller carboxylate ion.

(ii) Kinetics of the Base Hydrolysis of DSU. A pseudo first-order kinetic plot for the base-hydrolysis of the DSU monolayer based on Figure 2 is shown in Figure 3. For the y-axis, A_t is the absorbance of the ester carbonyl stretch at 1752 cm^{-1} at time t, and A_i is its absorbance before hydrolysis. The data shows a curve that the rate of the hydrolysis increases with hydrolysis time. For discussion purposes, the plot can be fit to two straight lines that intersect at $A_t/A_i \cong 0.40$ ($-\ln (A_t/A_i) = 0.91$), which is shown in the inset. This linearity shows that the hydrolysis of the DSU monolayer consists of two pseudo first-order reaction steps of different rate constants. That is, the reaction commences via a slow initiation step with a rate constant of 0.0755 $M^{-1}S^{-1}$, followed by a faster step with a rate constant of 0.175 $M^{-1}S^{-1}$. This reaction rate is ~1000 times slower than found for solution-phase analogs.[28]

As discussed in investigations of similar systems,[29, 30] this slow rate of conversion reflects, in part, a steric hindrance that is imposed by neighboring adsorbates upon the attack of hydroxide ions on the acyl carbon of the buried ester groups.[29] In other words, the cross

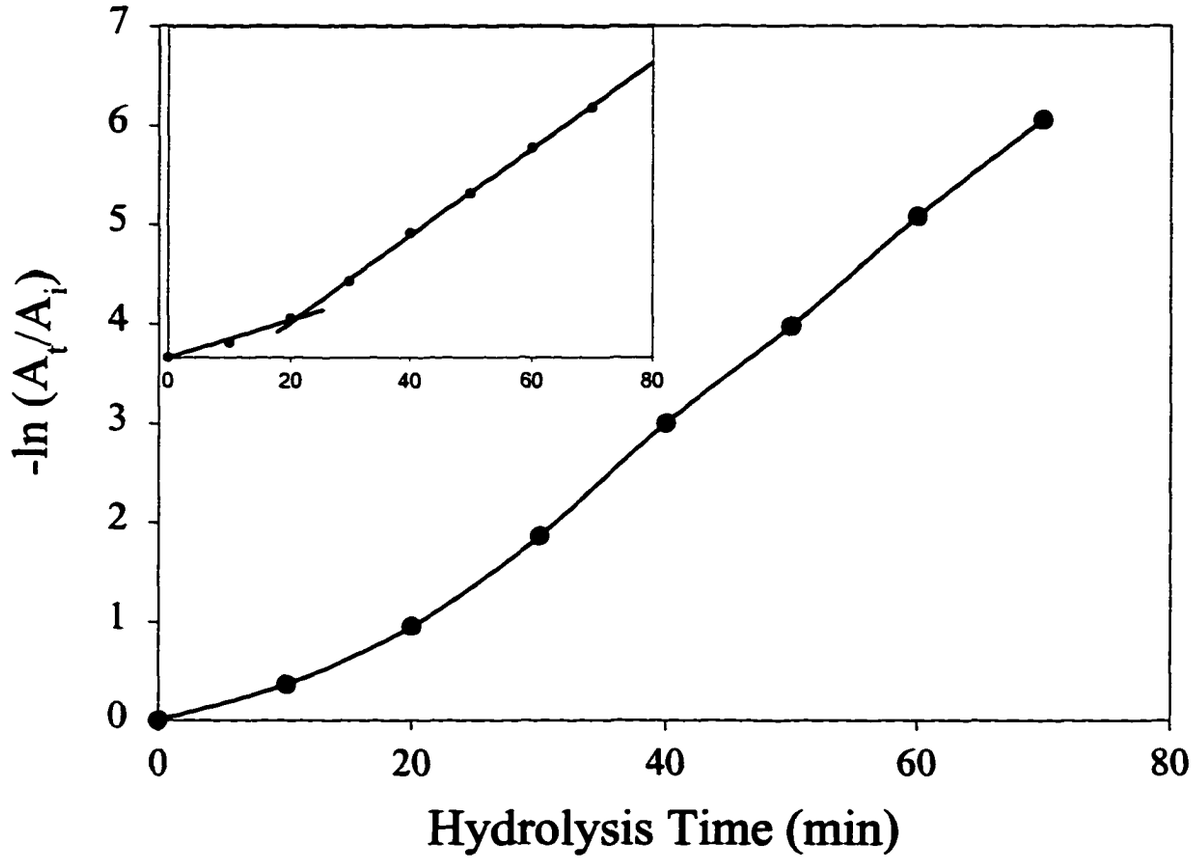

Figure 3. Pseudo first-order kinetic plot for the base-hydrolysis of a DSU monolayer at Au(111) in alkaline aqueous solution (10 mM KOH). A_i and A_t are the IRS absorbance of the ester carbonyl stretching mode (ν(C=O)) at 1752 cm^{-1} before hydrolysis and after time t, respectively.

section of the succinimidoxy group is ~20 Å^2, while that of the polymethylene chain is ~14 Å^2.[24] The bulky, large NHS group at the ω-position of the DSU molecule will therefore interfere with a regular packing of the hydrocarbon chains of DSU and thus cause difficulty for its polymethylene chain to achieve its closest-packed structure. Earlier studies show that the packing density of DSU on Au(111) is 75% of the maximum packing density of nonfunctionalized alkanethiols, which strongly suggests that the density of DSU on Au(111) is relatively high.[23] The bulky terminal succinimidyl groups, however, form a hydrophobic (in contrast to reactions in solution) layer at the monolayer-water interface, which results in a resistant hydrophobic barrier that reduces access of hydroxide ion to the underlying acyl carbon. Therefore, the hydrolysis process is initially impeded because of the slower penetration of hydroxide ions into the adlayer. Since the end groups of the DSU monolayer appear tightly packed, we speculate that the hydroxide ions must first penetrate into the monolayer through structural defects in the adlayer (e.g., domain boundaries) to initiate the reaction. As a consequence, the removal of some of the succinimidyl moieties on the surface not only decreases the steric hindrance of the monolayer, but also causes an increase in wettability (decrease of the contact angle) and hydrophilicity of the interface due to the conversion of the succinimidyl group (θ=50°) to the more hydrophilic carboxylate group (θ=0° at 100% carboxylate surface).[23] These effects result in an increase in the accessibility of the hydroxide ions to the monolayer chain and an acceleration of the reaction rate.

In our experiments, annealed gold on mica was used as the substrate to form the DSU monolayer. Defects like grain boundaries account for effectively all the defects at the smoother annealed samples. The domain boundaries are formed when neighboring domains

of a monolayer grow together. Figure 4 generalizes the proposed mechanism for the two-step hydrolysis of a DSU monolayer. In the first step, the hydroxide ions penetrate into the monolayer through defects and attack the ester carbonyl carbon. The initial rate constant, however, certainly varies from defect to defect depending on the size of the defect. Therefore, this initiation step is defect-controlled and the "local" rate constant k_i depends on the size of each defect.

This initial step results in the removal of the terminal NHS groups from the DSU molecules which are near the defect, and enhances the access of hydroxide ions. Next, the hydroxide ions can penetrate into the chain not only through the surface defects, but also through the open channels near the defects to attack the acyl carbon. Therefore, the reaction rate of this step is not defect-controlled and can be represented by k_2. Finally, all the succinimidyl end groups are converted to carboxylate ions at this larger rate.

Microscopic Characterization by SFM. As demonstrated in our[16] and other laboratories,[10, 31-33] friction imaging is sensitive to the chemical composition of the outermost few angstroms of an interface. The observed friction at the microcontact formed between a SFM probe tip with a high surface free energy (e.g., uncoated Si_3N_4) and a sample with a high surface free energy is greater than that for a sample with a low surface free energy.[16] The ability to do chemical functionality imaging with SFM can be utilized to monitor interfacial chemical reactions in real time if the chemical transformation will induce a detectable frictional contrast. Wetting characterizations using water as a probe liquid yield an advancing contact angle for a DSU monolayer and fully hydrolyzed DSU monolayer of 50° and ~0°, respectively.[23] It then follows that the friction measured when an uncoated

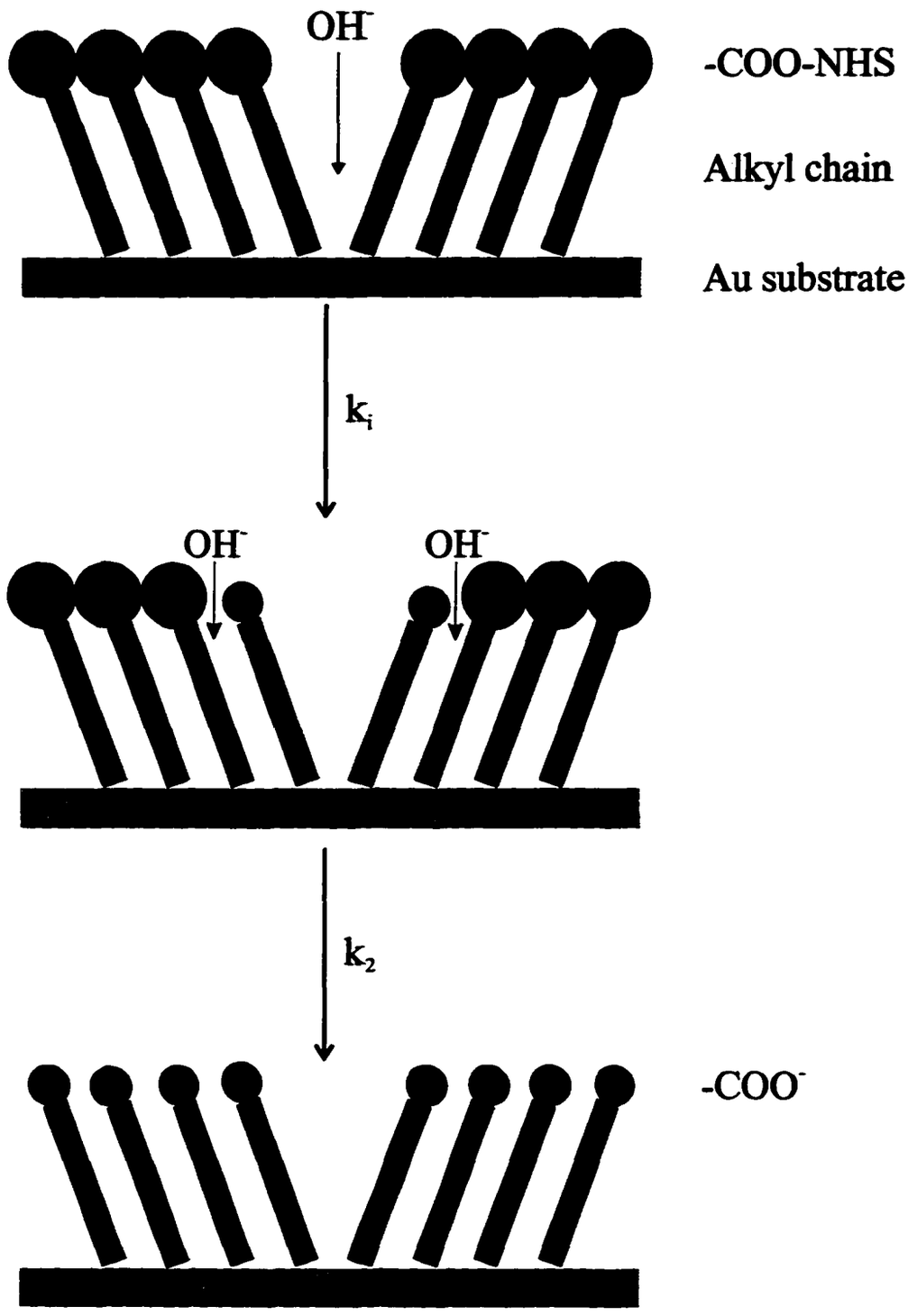

Figure 4. Schematic of the mechanism for the defect-nucleated base hydrolysis of a DSU monolayer at Au(111). k_i is the rate constant of an initiation step and k_2 is the rate constant of the faster reaction step.

Si_3N_4 tip is in contact with a DSU adlayer should be lower than that when an uncoated Si_3N_4 tip is in contact with a fully hydrolyzed DSU adlayer. The in situ image of the compositionally patterned DSU and fully hydrolyzed DSU sample, which was reported earlier by us,[18] showed that the observed friction for the DSU monolayer is ~10 nN lower than that for the fully hydrolyzed DSU adlayer at a load of ~25 nN. Furthermore, an analysis of friction loops reveals that the friction between an uncoated Si_3N_4 probe tip and unhydrolyzed DSU monolayer is ~30 nN, whereas that between an uncoated Si_3N_4 probe tip and fully hydrolyzed DSU monolayer is ~40 nN. These observations are consistent with the earlier predictions based on considerations of the differences in the surface free energy of the two types of samples.

Figures 5A-F show the in situ friction images (300 nm x 300 nm) and cross-sections of a DSU monolayer at Au(111) as a function of immersion time in an alkaline (10 mM KOH) aqueous solution. These images were acquired at the same location on the surface at a contact load of ~25 nN. Figure 5A was taken under deionized water (pH 6.2). A large terrace is evident in the middle of the image. The terrace has a relatively low and homogeneous friction (~30 nN). Figure 5B was obtained after the sample was exposed to the alkaline aqueous solution for 20 min. Small, localized regions of high friction (~40 nN) interspersed among regions of low friction (~30 nN) are present. Based on the noted control experiment with the patterned sample,[18], we attributed this difference to the partial hydrolysis of the DSU monolayer in the alkaline aqueous solution. That is, the regions of high friction correspond to domains in the adlayer composed largely of carboxylate end groups, and the regions of low friction correspond to domains comprised largely of the ester terminus of the

Figure 5. In situ friction images (300 nm x 300 nm) and cross sections of a DSU monolayer chemisorbed at Au(111) in the SFM liquid cell in (A) deionized water (pH 6.2) and after exposing the sample to an alkaline (10 mM KOH) aqueous solution for (B) 20 min; (C) 40 min; (D) 70 min; (E) 100 min; and (F) 120 min, respectively. These images were acquired at a load of ~25 nN and scan rate of 10 Hz.

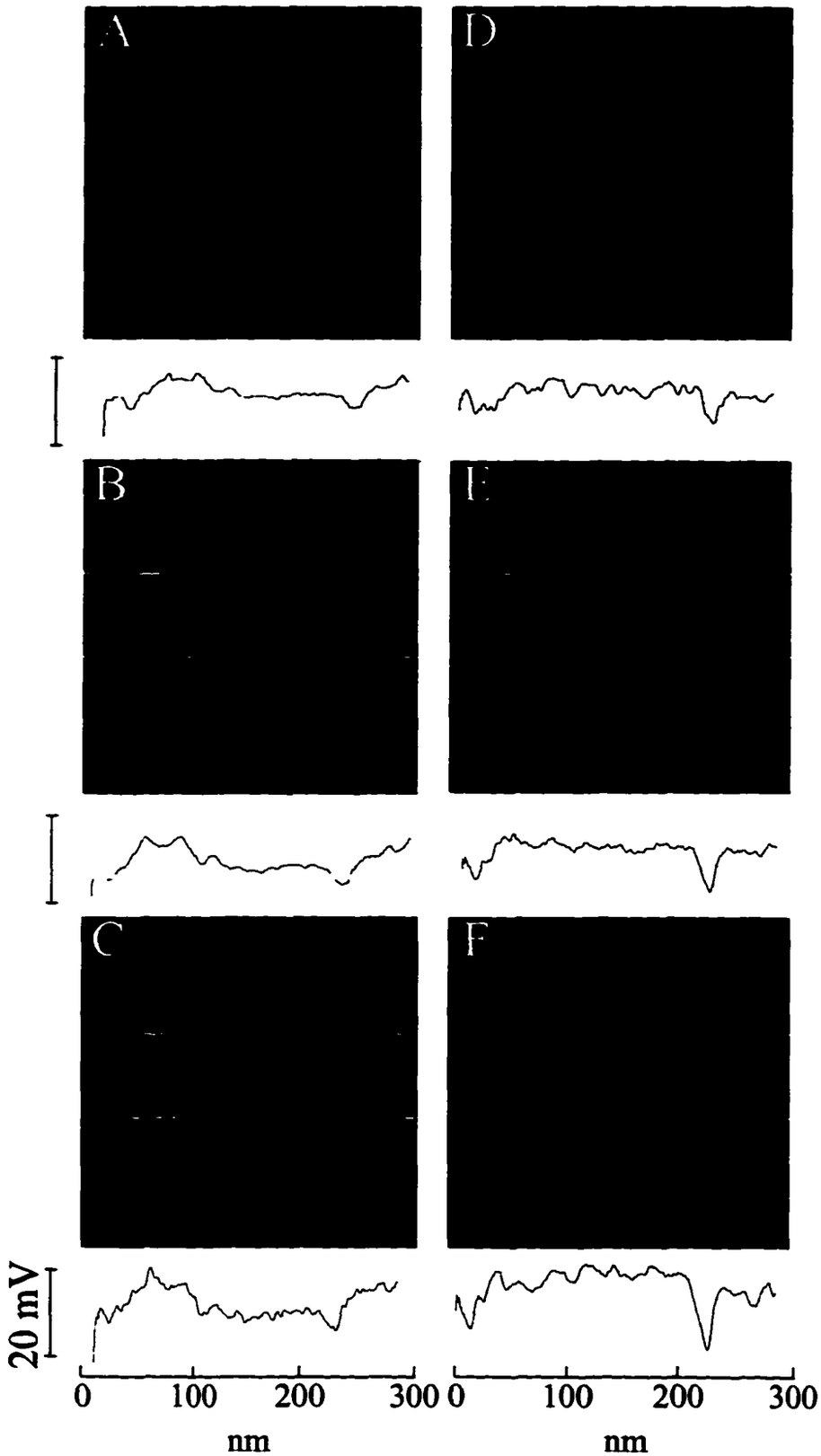
A
D
B
E
C
F
20 mV
0
100
200
300
nm
0
100
200
300
nm

unhydrolyzed DSU adlayer. The friction images in Figures 5C-F were obtained following exposure of the sample to 10 mM KOH for 40, 70, 100 and 120 min, respectively. These images clearly show that the area of high friction grows larger with longer exposure time, indicating the extent of the hydrolysis as a function of immersion time can be followed microscopically via SFM.

Data Analysis. It is important to establish the level at which the observed friction changes can be correlated with the extent of the compositional change induced by the base-hydrolysis of the DSU adlayer. As such, the macroscopic compositional changes were followed using IRS via the growth of the symmetric and asymmetric carboxylate stretching modes, and the microscopic compositional changes were determined from the in situ images shown in Figures 5A-F by using the Bearing Analysis resident in the Nanoscope III software. This analysis sets a threshold in the magnitude of a z-displacement (i.e., height or friction) and calculates the total percentage of the surface above the reference plane set by the threshold. The Bearing Analysis was carried out at a 100 nm x 100 nm area on the terrace at different hydrolysis times.

The comparison of the macroscopic and microscopic results is shown in Figure 6. The percentage of the conversion for the macroscopic data was calculated by ratioing the IR absorbance of the symmetric carboxylate band at 1446 cm^{-1} at immersion time t to that of the band after full reaction. The data indicated that the extent of the transformation determined using the two different techniques differed by no more than 10% for all immersion times, and both curves show the similar trend as a function of hydrolysis time. However, the extent of the conversion based on the microscopic data is always less than that from the macroscopic

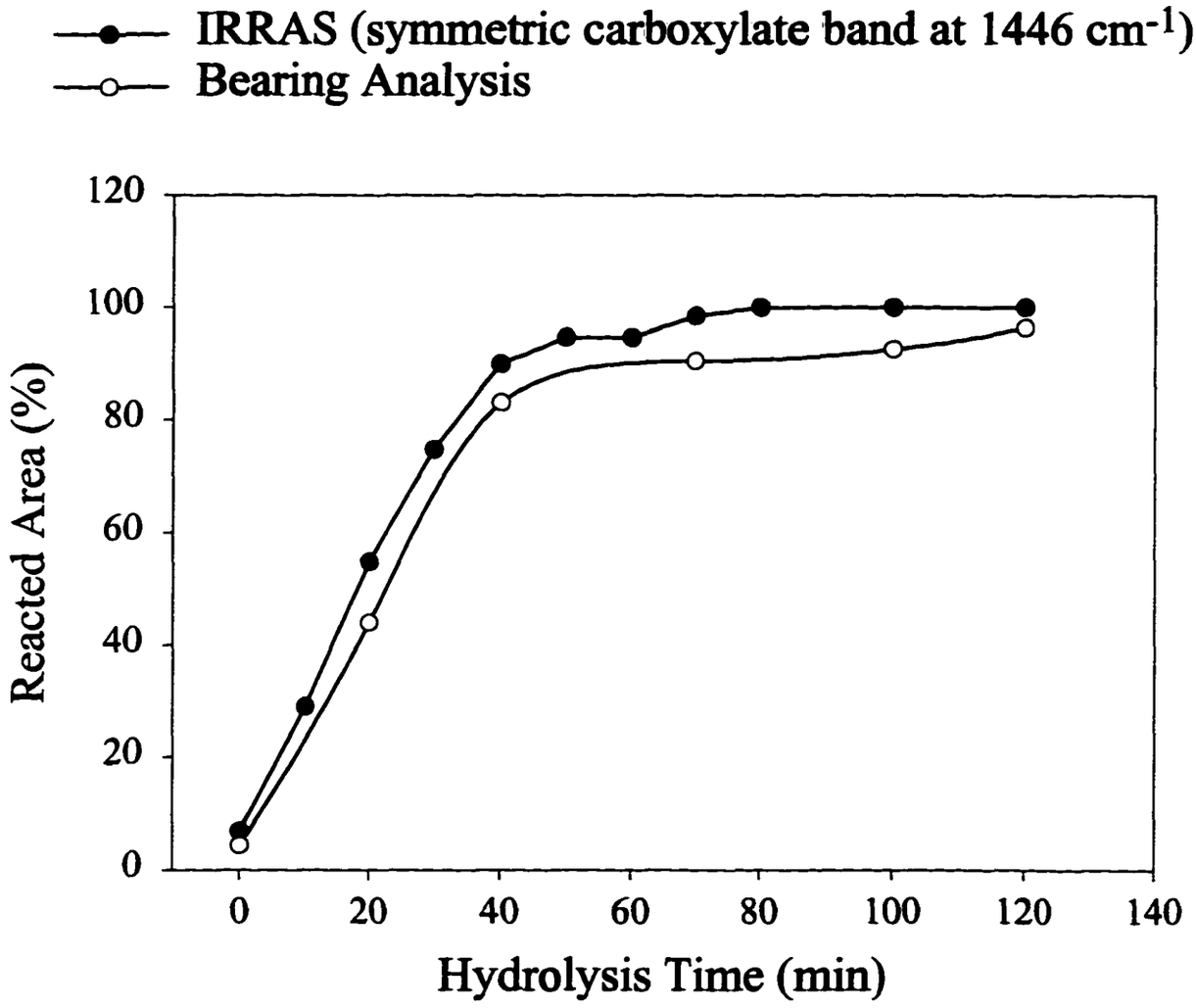

Figure 6. Comparison of the macroscopic and microscopic data. The reacted area of the macroscopic data is determined by the ratio of the IRS absorbance of the symmetric carboxylate band at 1446 cm^{-1} at immersion time t to that of after fully reacted. The reacted area of the microscopic data is determined from the in situ images in Figure 5 using Bearing Analysis.

data determined from IRS. This difference could be due in part to the sensitivity of IRS to the orientation and packing of the monolayer chain. As discussed earlier, with the bulky succinimidyl groups being replaced by the smaller carboxylate ions, some changes in the spatial orientation of the adlayer are expected. Since the structure of the monolayer is more disordered, which is evident by the noted shift of the methylene C-H stretching bands to higher wavenumbers, the quantitative reliability of the analysis is weakened. The correlations between the macroscopic and microscopic data indicate that the friction change corresponds to the compositional change of the monolayer during the hydrolysis.

Since the reaction rate obtained by analyzing the ex situ IRS spectra is the average rate at a macroscopic length scale, the question about whether the hydrolysis occurs homogeneously or heterogeneously across the surface at a microscopic length scale remains unanswered. Based on the mechanism illustrated in Figure 4, the hydrolysis process should be defect-nucleated, i.e., the reaction starts at surface defects, such as domain boundaries, and the process continues from these locations to the neighboring areas. In an attempt to look for evidence for the proposed mechanism, a 90 nm x 90 nm area on the terrace at different hydrolysis time was zoomed in and the images were contrast-enhanced and thresholded to yield the images shown in Figures 7A-F. A triangular mark is used to index three different locations. The darker regions are areas of high friction. It can be seen that before hydrolysis (Figure 7A), the 90 nm x 90 nm area is free of detectable high friction regions. After 20 min in 10 mM KOH, regions with high friction become evident. With longer exposure time, these regions expand and eventually coalesce. This observation indicates a heterogeneity in the reaction rates on different areas of the surface. A homogeneous reaction rate would have

Figure 7. Zoomed-in images (90 nm x 90 nm) of the in situ friction images (300 nm x 300 nm) shown in Figure 5. The zoomed-in area is located at the top of the terrace in Figure 5.

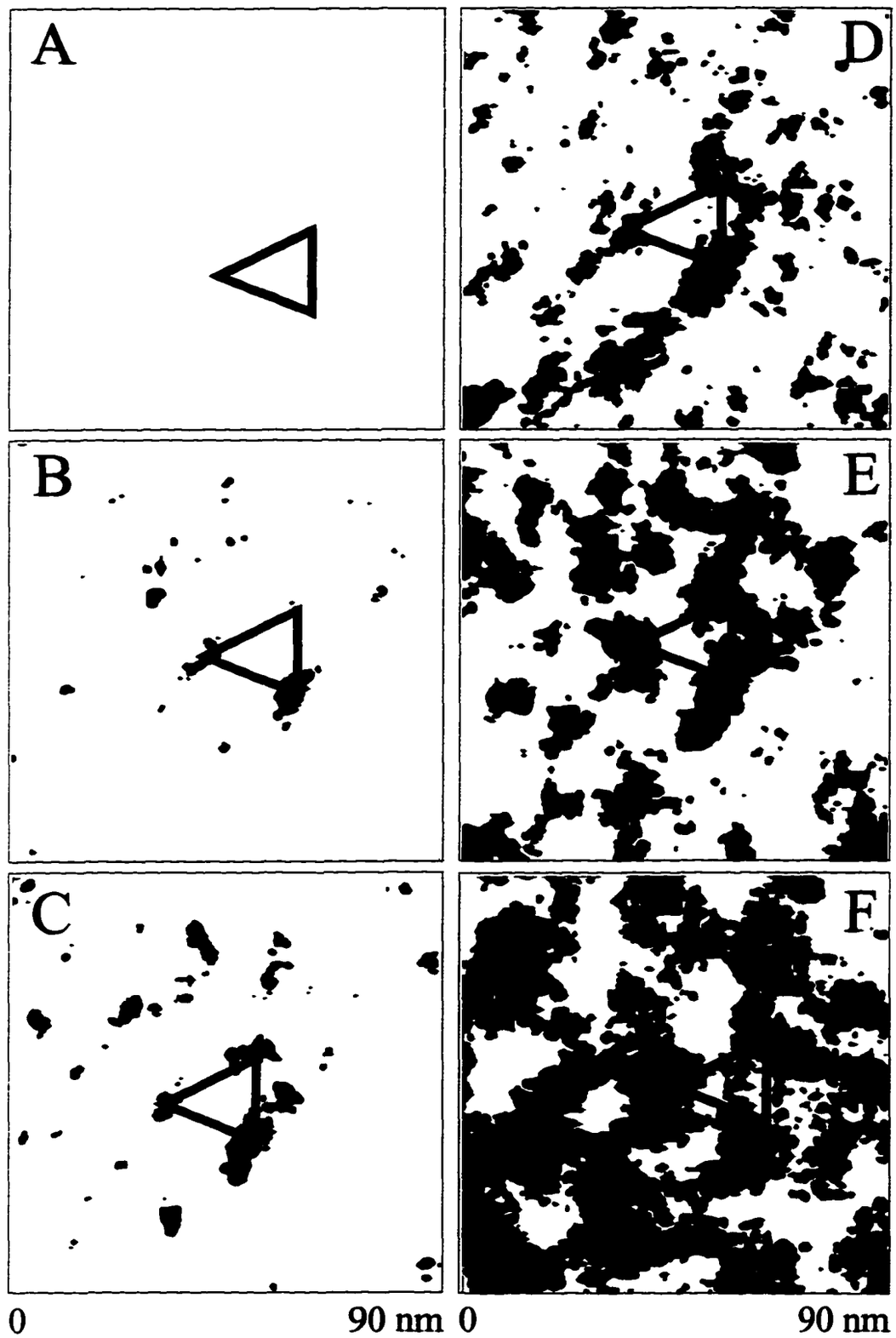
A
D
B
E
C
F
0
90 nm
0
90 nm

caused a uniform change in the friction of the imaged area instead of the nucleation-like growth of the high friction regions. This observation is consistent with our hypothesis that the reaction is nucleated at defect sites such as grain boundaries.

To look for differences in localized reactivity, two different 30 nm x 30 nm areas in the top left and center of the 90 nm x 90 nm region, respectively, were analyzed with Bearing Analysis, and compared to the result of the 90 nm x 90 nm region. The results are shown in Figure 8. As is evident, location 1 and 2 react at different rates in comparison to the 90 nm x 90 nm area. Compared with location 1, location 2 has a faster initial rate (until ~30 min). The reaction at location 1 also reacts to completion faster than location 2. This shows that although the Bearing Analysis result of the larger area is comparable with the macroscopic data obtained from IRS, the localized microscopic reactivity is different at different locations. This result is further evidence of the non-homogeneity of the reaction.

Conclusions

We have shown that frictional force imaging can be applied to follow the chemical transformation of the base-hydrolysis of a dithio-bis(succinimidylundecanoate) monolayer chemisorbed on a gold substrate. The results indicate that the friction at the microcontact formed between a Si_3N_4 probe tip and a dithio-bis(succinimidylundecanoate)-modified Au(111) substrate increases as the succinimidyl group is replaced by the carboxylate ion. This increase is consistent with an increase in the interfacial surface tension at the microcontact. A correlation between the macroscopic data determined from IRS and the microscopic data determined from the in situ SFM images was also made to confirm that the

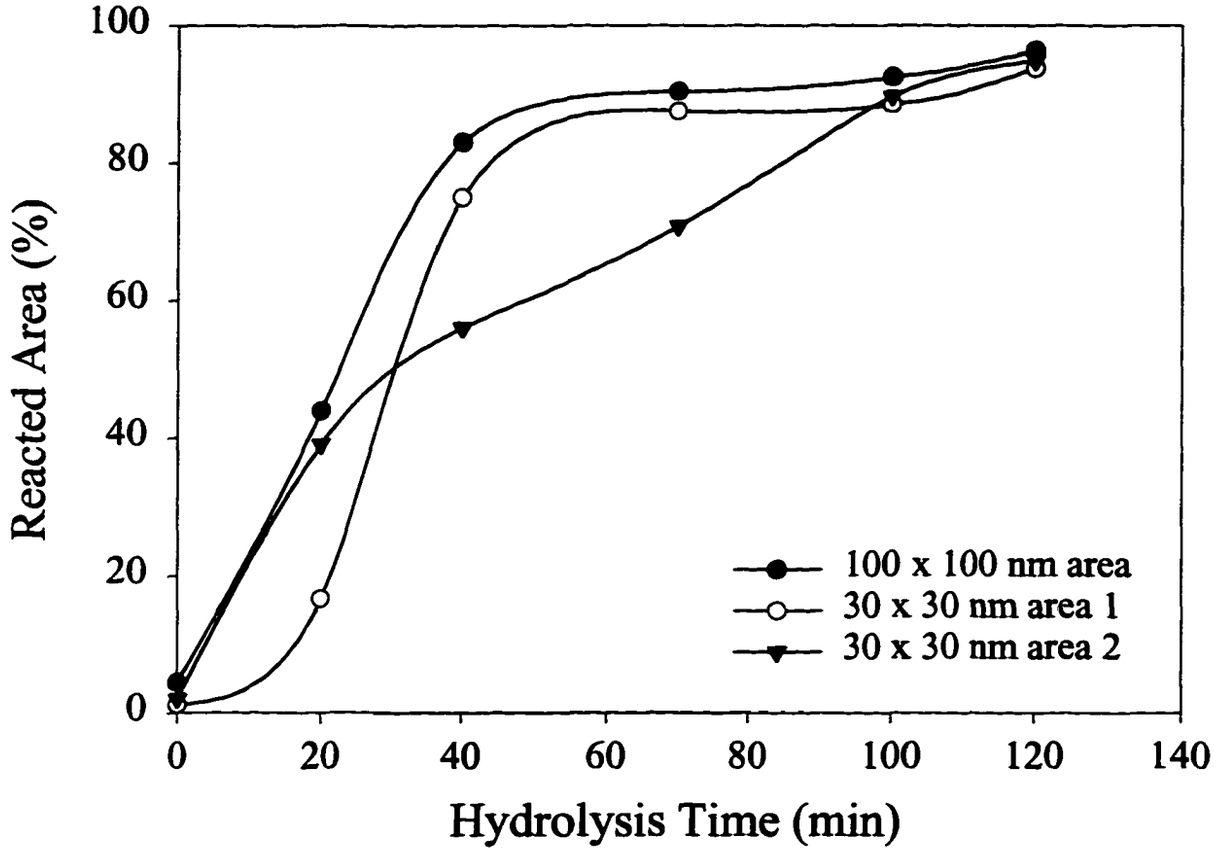

Figure 8. Bearing analysis results for a 100 nm x 100 nm area and two 30 nm x 30 nm spots in the area. The same threshold was used for all three regions.

friction change is resulted from the composition change during the hydrolysis. The study also shows the heterogeneity of the interfacial chemical reaction, i.e., it's a defect-nucleated process and has different localized microscopic reactivity for different surface locations.

Acknowledgments

This work was supported in part by the Office of Basic Energy Sciences, Chemical Science Division, of the U.S. Department of Energy, the National Science Foundation (BIR-9601789), and the Microanalytical Instrumentation Center of Iowa State University. The Ames Laboratory is operated for the U.S. Department of Energy by Iowa State University under Contract No. W-7405-eng-82.

References

(1) Quate, C. F. *Surface Science* **1994,** *299/300*, 980-995.

(2) Radmacher, M.; Tillmann, R. W.; Fritz, M.; Gaub, H. E. *Science* **1992,** *257*, 1900-1905.

(3) Magonov, S. N. *Appl. Specrosc. Rev.* **1993,** *28*, 1-121.

(4) Blackman, G. S.; Mate, C. M.; Philpot, M. R. *Phys. Rev. Lett.* **1990,** *65*, 2270-2273.

(5) Burnham, N. A.; Colton, R. J. *J. Vac. Sci. and Tech. A* **1989,** *7*, 2906-2913.

(6) Burnham, N. A.; Dominguez, D. A.; Mowery, R. L.; Colton, R. J. *Phys. Rev. Lett.* **1990,** *64*, 1931-1934.

(7) Fujihira, M.; Kawate, H.; Yasutake, M. *Chem. Lett.* **1992,** *1992*, 2223-2226.

(8) Joyce, S. A.; Houston, J. E.; Michalske, T. A. *Appl. Phys. Lett.* **1992,** *60*, 1175-1177.

(9) Overney, R. M.; Meyer, E.; Frommer, J.; Brodbeck, D.; Lüthi, R.; Howald, L.; Güntherodt, H.-J.; Fujihira, M.; Takano, H.; Gotoh, Y. *Nature* **1992,** *359*, 133-135.

(10) Frisbie, C. D.; Rozsnyai, L. F.; Noy, A.; Wrighton, M. S.; Lieber, C. M. *Science* **1994,** *265*, 2071-2074.

(11) Noy, A.; Frisbie, C. D.; Rozsnyai, L. F.; Wrighton, M. S.; Lieber, C. M. *J. Am. Chem. Soc.* **1995,** *117*, 7943-7951.

(12) Wilbur, J. L.; Biebuyck, H. A.; MacDonald, J. C.; Whitesides, G. M. *Langmuir* **1995,** *11*, 825-831.

(13) Thomas, R. C.; Tangyunyong, P.; Houston, J. E.; Michalske, T. A.; Crooks, R. M. *J. Phys. Chem.* **1994,** *98*, 4493-4494.

(14) Marti, A.; Hahner, G.; Spencer, N. D. *Langmuir* **1995,** *11*, 4632-4635.

(15) Berger, C. E. H.; Werf, K. O. v. d.; Kooyman, R. P. H.; Grooth, B. G. d.; Greve, J. *Langmuir* **1995,** *11*, 4188-4192.

(16) Green, J.-B. D.; McDermott, M. T.; Porter, M. D. *J. Phys. Chem.* **1995,** *99*, 10960-10965.

(17) Green, J.-B. D.; McDermott, M. T.; Porter, M. D. *J. Phys. Chem.* **1996,** *100*, 13342-13345.

(18) Wang, J.; Kenseth, J. R.; Jones, V. W.; Green, J.-B. D.; McDermott, M. T.; Porter, M. D. *J. Am. Chem. Soc.* **1997**, accepted.

(19) Haussling, L.; Michel, B.; Ringsdorf, H.; Rohrer, H. *Angewandte Chemie (Int. Ed. Engl.)* **1991,** *30*, 569-572.

(20) Lee, G. U.; Kidwell, D. A.; Colton, R. J. *Langmuir* **1994,** *10*, 354-357.

(21) Stuart, J. K.; Hlady, V. *Langmuir* **1995,** *11*, 1368-1374.

(22) Radmacher, M.; Fritz, M.; Cleveland, J. P.; Walters, D. A.; Hansma, P. K. *Langmuir* **1994,** *10*, 3809-3814.

(23) Wagner, P.; Hegner, M.; Kernen, P.; Zaugg, F.; Semenza, G. *Biophys. J.* **1996,** *70*, 2052-2066.

(24) Nakano, K.; Taira, H.; Maeda, M.; Takagi, M. *Anal. Sci.* **1993,** *9*, 133-136.

(25) Kenseth, J. R.; Jones, V. W.; Porter, M. D., manuscript in preparation.

(26) Frey, B. L.; Corn, R. M. *Anal. Chem.* **1996,** *68*, 3187-3193.

(27) Porter, M. D.; Bright, T. B.; Allara, D. L.; Chidsey, C. E. D. *J. Am. Chem. Soc.* **1987,** *109*, 3559-3568.

(28) Cline, G. W.; Hanna, S. B. *J. Org. Chem.* **1988,** *53*, 3583-3586.

(29) Ryswyk, H. V.; Turtle, E. D.; R.Watson-Clark; Tanzer, T. A.; Herman, T. K.; Chong, P. Y.; Waller, P. J.; Taurog, A. L.; Wagner, C. E. *Langmuir* **1996,** *12*, 6143-6150.

(30) Holmes-Farley, S. R.; Whitesides, G. M. *Langmuir* **1987,** *3*, 62-76.

(31) Vezenov, D. V.; Noy, A.; Rozsnyai, L. F.; Lieber, C. M. *J. Am. Chem. Soc.* **1997,** *119*, 2006-2015.

(32) Noy, A.; Frisbie, C. D.; Rozsnyai, L. F.; Wrighton, M. S.; Lieber, C. M. *J. Am. Chem. Soc.* **1995,** *117*, 7943-7951.

(33) Wilbur, J. L.; Biebuyck, H. A.; MacDonald, J. C.; Whitesides, G. M. *Langmuir* **1995,** *11*, 825-831.

CHAPTER 3. SFM TIP-ASSISTED HYDROLYSIS OF A DITHIO-BIS(SUCCINIMIDYLUNDECANOATE) MONOLAYER CHEMISORBED ON A AU(111) SURFACE

A paper accepted by the *Journal of American Chemical Society*

Jianhong Wang, Jeremy R. Kenseth, Vivian W. Jones, John-Bruce D. Green, Mark T. McDermott, and Marc D. Porter

Abstract

This paper reports on the use of a scanning force microscope (SFM) for the *tip-assisted* base-hydrolysis of an ester-terminated alkanethiolate monolayer on Au(111). We have found that contact imaging accelerates the base-hydrolysis of a dithio-bis(succinimidylundecanoate) monolayer relative to the surrounding unimaged area. It is proposed that 1) the mechanical disruption by the SFM probe tip of the steric barrier imposed by the neighboring adsorbates facilitates access of hydroxide ions to the buried acyl carbons in the adlayer, and 2) the surface area hydrolytically transformed by this disruption can be controlled by the SFM imaging conditions. Findings in support of our conclusions are presented, and potential implications to nanotechnology are briefly discussed.

Introduction

The scanning probe microscopies have proven invaluable as surface characterization tools to an impressive range of fundamental and technological areas.[1-4] We have, in parallel with the efforts of others,[5-15] been exploring the use of the friction and adhesion modes of scanning force microscopy (SFM) as probes of the compositional transformations of interfaces at nanometer length scales.[16,17] While continuing such investigations,[18] we have discovered that the mechanical interaction between a SFM probe tip and various ester-functionalized alkanethiolate monolayers can notably accelerate the rate of the base-hydrolysis of the ester linkage in small, spatially-defined locations. The following describes our initial findings using monolayers chemisorbed at Au(111) from dithio-bis(succinimidylundecanoate) (DSU). We also briefly speculate on the possible impact of this type of processing[19-21] to the nanofabrication of surfaces for sensor technology.

Experimental Section

Sample Preparation. (i) Au(111) Substrates. Substrates were prepared by the resistive evaporation of 300 nm of gold onto freshly cleaved mica sheets. Upon removal from the evaporator, the substrates were oven-annealed at 300 °C for 5 h. This processing results in a film with a predominant Au(111)-surface crystallinity.[17]

(ii) Monolayer Films. Two different types of monolayer samples were prepared. The first type was used in the investigations of the tip-induced acceleration of the base-hydrolysis for the DSU monolayers at Au(111). The second type was used as a control for

the determination of the differences in the friction at both unhydrolyzed and fully hydrolyzed monolayers of DSU.

The first type of sample was formed by the immersion of the Au(111) substrates into a dilute (0.1 mM) ethanolic solution of DSU for 24 hr. These samples were then removed from the formation solution, rinsed copiously with ethanol, and air-dried. The synthesis of DSU followed literature procedures[22,23] and will be detailed elsewhere.[24]

The second type of sample was prepared using a more extensive procedure. This procedure, which yielded a compositionally patterned adlayer of both unhydrolyzed and fully hydrolyzed DSU, is composed of three general steps. Step 1 entailed the immersion of a gold-bound DSU monolayer into an alkaline (1 M KOH) aqueous solution for 6 hr. This step, as determined using infrared reflection spectroscopy (IRS),[18] fully converts the succinimidyl terminus of the adlayer to a carboxylate moiety. Step 2 utilized "thiolate photolithography"[25] to construct a compositionally patterned adlayer. The patterns were created by sandwiching a copper transmission electron microscopy (TEM) grid (2000 mesh (hole size: 7.5 μm, bar size: 5.0 μm)) between a DSU-coated sample and a quartz plate. A 200-watt, medium pressure mercury lamp (Oriel) was used as the light source. The beam was collimated, reflected off an air-cooled, dichroic mirror (220-260 nm), focused by a fused silica lens, and passed through the TEM grid before impinging onto the sample surface. The power at the sample was estimated at 550 mW/cm^2. Exposure times were ~20 min. Overall, this process converts the irradiated gold-bound thiolates to various forms of oxygenated sulfur (e.g., RSO_3^-)[26] which are readily rinsed from the surface with most organic solvents.

Step 3 involved the removal of the oxygenated sulfur species by rinsing extensively the irradiated samples with deionized water and ethanol. After drying under a stream of argon, the samples were re-immersed into the dilute DSU solution for ~12 hr. Overall, the combination of the three step processing results in a compositionally-patterned surface, with DSU adsorbed in the squares and carboxylate-terminated adsorbates confined in the grids.[18,27]

Instrumentation. (i) Scanning Force Microscopy (SFM). All images were collected using a 12-μm tube scanner, SFM fluid cell, and Digital Instruments Multi Mode NanoScope III. The force constant of the triangular Si_3N_4 cantilevers (Digital Instruments) for normal bending was ~0.06 N/m and for torsional bending was ~80 N/m.[17] Unless noted otherwise, all images (512 x 512 pixels) were collected in situ in 10 mM KOH or in deionized water (pH 6.2) at a scan rate of 10.2 Hz.

(ii) Infrared Reflection Spectroscopy (IRS). The progression of the base-hydrolysis of the DSU monolayers at Au(111) was determined using IRS. These characterizations were performed in an ex situ mode for samples immersed in a 10 mM KOH solution for varied periods of time. The emersed samples were rinsed with ethanol prior to mounting in the N_2-purged chamber of a fourier transform infrared spectrometer. The extent of the base-hydrolysis was determined by the appearance of the symmetric (1446 cm^{-1}) and asymmetric (1590 cm^{-1}) carboxylate stretching modes that are characteristic of the immobilized product of the reaction.[18]

Data Analysis. The extent of the base-hydrolysis from the SFM images was determined using the Bearing Analysis resident in the NanoScope III software. This analysis

sets a threshold in the magnitude of a z-displacement (i.e., height or friction) and calculates the total percentage of the surface above the reference plane set by the threshold.

Results and Discussion

Concepts and General Observations. Scheme 1 idealizes the molecular architecture and base-hydrolyzed transformation of an ester-functionalized monolayer that forms at Au(111) from a dilute (0.1 mM) ethanolic solution of DSU.[22-24] Characterizations of the rate for the hydrolysis of the ester linkage of the adlayer using IRS indicate that the full conversion of the succinimidyl terminus to the corresponding carboxylate moiety requires more than 2 hr. for completion in an alkaline (10 mM KOH) solution.[28] This rate is ~1000 times slower than found for solution-phase analogs.[29] As discussed in investigations of similar systems,[30,31] this low rate of conversion reflects, in part, the steric hindrance that is imposed by neighboring adsorbates upon the attack of hydroxide ions on the acyl carbon of the buried ester groups.[30]

The remaining sections of this paper present our evidence for the tip-assisted base hydrolysis. We begin by discussing the underpinnings for the analysis of the SFM data in terms of the compositional changes that arise from the base-hydrolysis of the DSU monolayers. We then demonstrate that the rate of the base-hydrolysis is *enhanced* by the direct physical contact of the probe tip with the DSU adlayer during the SFM imaging process.

Scheme 1

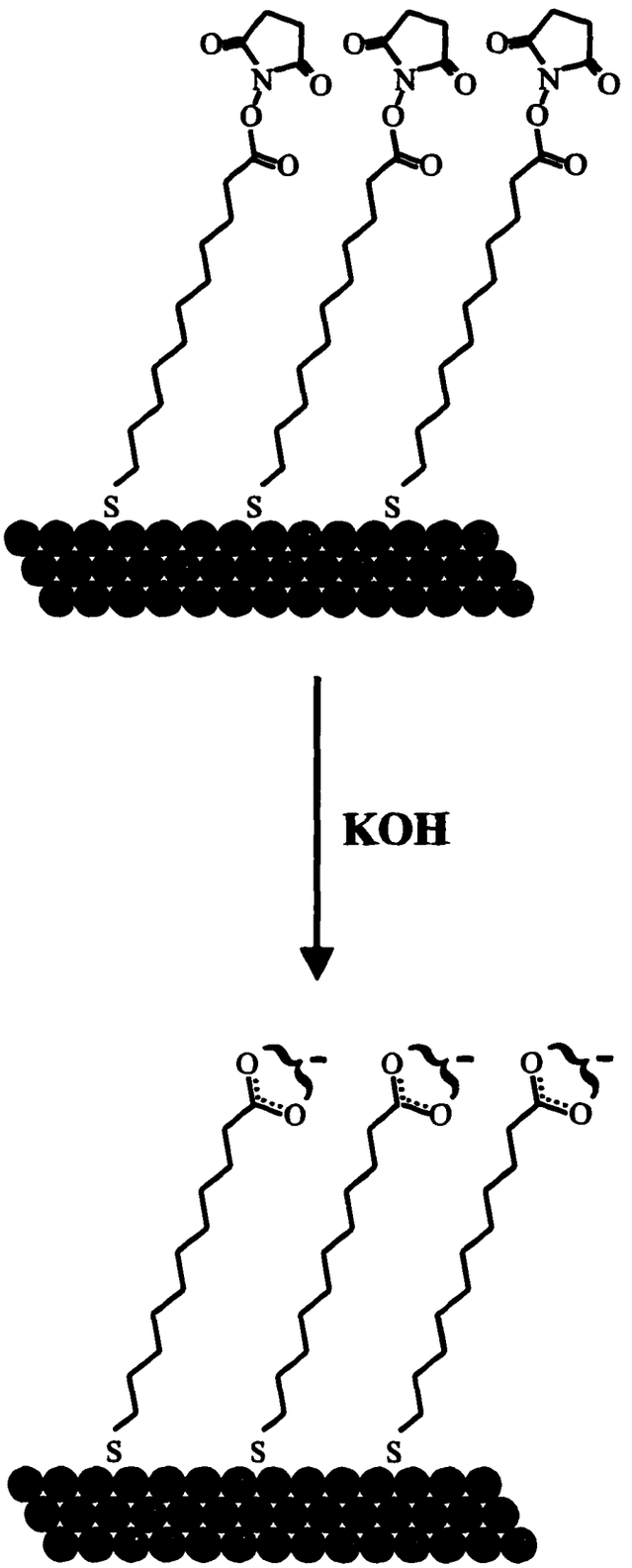

Detection of the Compositional Changes of DSU Monolayers at Au(111) by SFM from Base Hydrolysis. The analysis of the SFM images regarding the chemical transformation that results from the base-hydrolysis of the ester linkage of the DSU monolayers chemisorbed at Au(111) relies on the sensitivity of frictional imaging to the chemical composition of the outermost few angstroms on an interface.[8-11,17] As recently demonstrated,[17] the observed friction at the microcontact formed between a SFM probe tip with a high surface free energy (e.g., uncoated Si_3N_4) and a sample with a high surface free energy is greater than that for a sample with a low surface free energy.[32] Wetting characterizations using water as a probe liquid yield an advancing contact angle for a DSU monolayer and fully hydrolyzed DSU monolayer of 50° and ~0°, respectively.[22] It then follows that the friction measured when an uncoated Si_3N_4 tip is in contact with a DSU adlayer should be lower than that when an uncoated Si_3N_4 tip is in contact with a fully hydrolyzed DSU adlayer.

The in situ image of the compositionally patterned sample in Figure 1 is consistent with the general tenants of the above analysis and quantifies the differences in the friction for an adlayer of DSU and its base-hydrolyzed analog. This sample, which was imaged in deionized water (pH 6.2) at a load of ~25 nN, was prepared using thiolate photolithography[25] (see Experimental Section) and was patterned to consist of a DSU adlayer in the squares and a carboxylate-terminated adlayer (i.e., regions of fully hydrolyzed DSU) in the grids. As is evident, the observed friction for the adlayer in the squares is ~10 nN lower than that for the adlayer in the grids. Furthermore, an analysis of friction loops (not shown) reveals that the

Figure 1. Friction force image (50.0 μm x 50.0 μm) of a sample patterned with regions of DSU and fully hydrolyzed DSU monolayers recorded in deionized water (pH 6.2). The light regions (the grids) are areas of high friction and correspond to surface regions terminated with carboxylate adsorbates. The dark regions (the squares) are areas of low frictionand correspond to the surface regions with adsorbed DSU monolayer. The image was acquired at a load of ~25 nN and scan rate of 5.5 Hz.

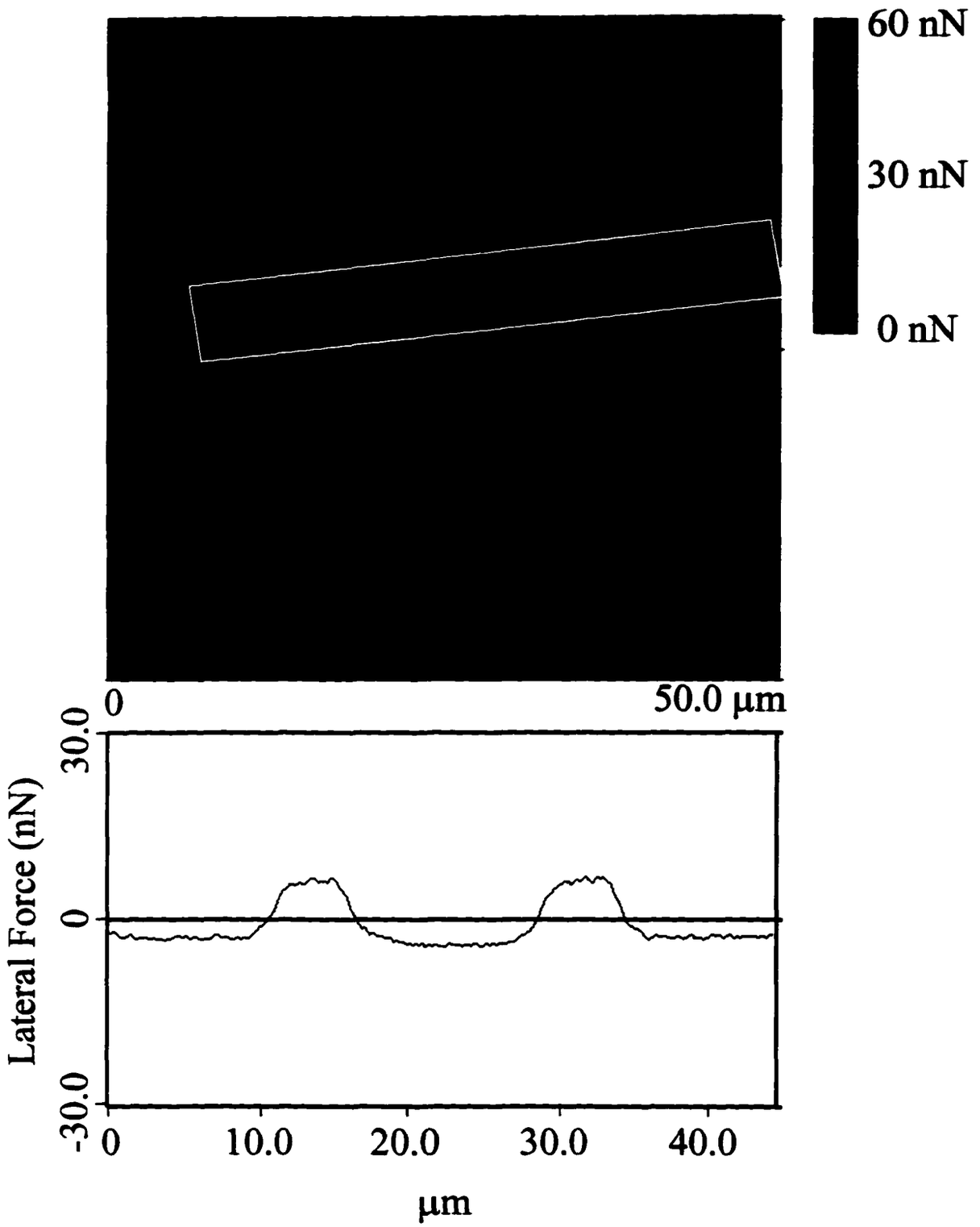
60 nN
30 nN
0 nN
0
50.0 µm
Lateral Force (nN)
30.0
0
-30.0
0
10.0
20.0
30.0
40.0
µm

friction between an uncoated Si_3N_4 probe tip and unhydrolyzed DSU monolayer is ~30 nN, whereas that between an uncoated Si_3N_4 probe tip and fully hydrolyzed DSU monolayer is ~40 nN. These observations are consistent with the earlier predictions based on considerations of the differences in the surface free energy of the two types of samples.

It is also important to establish the level at which the observed friction changes can be correlated with the extent of the compositional change induced by the base-hydrolysis of the DSU adlayer. As such, compositional changes were followed using IRS via the growth of the symmetric and asymmetric carboxylate stretching modes. These experiments were conducted by immersing a freshly prepared DSU monolayer into 10 mM KOH for differing periods of time, and characterizing the carefully rinsed sample via IRS.[33] These results were then compared to the compositional changes determined using Bearing Analysis from the in situ images of samples (i.e., samples not repetitively scanned) immersed in 10 mM KOH. This comparison, which will be reported in detail elsewhere,[18] indicated that 1) the extent of the transformation determined using the two different techniques differed by no more than 10% for all immersion times, and 2) the detectable difference (i.e., sensitivity) in the extent of the transformation from the analysis of the friction data was 10%. The next section presents evidence for the tip-assisted hydrolysis of a DSU monolayer, with the data examined within the context of the above analytical figures of merit.

Tip-Assisted Hydrolysis. Evidence for the *tip-assisted* acceleration of the base hydrolysis for a DSU monolayer chemisorbed at Au(111) that arises from contact imaging is presented by the 4.0 μm x 4.0 μm images in Figure 2. Figure 2A contains a topographic image and cross-sectional profile,[34] with the corresponding frictional image and cross-

Figure 2. In situ topographic (A) and friction (B) images (4.0 μm x 4.0 μm) and cross-sections of a DSU monolayer chemisorbed at Au(111) after immersion for 1 hr in an alkaline (10 mM KOH) aqueous solution. The y-axis of the cross-sectional profiles for Figures 1A,B are the "height" and "lateral signal", respectively. These images were acquired at a load of ~25 nN and scan rate of 10 Hz after repetitively scanning for 1 hr at a load of ~25 nN the 1.0 μm x 1.0 μm area that is evident to the right of the center of the friction image. Both cross-sectional plots represent the results of averaging cross-sectional analyses.[34]

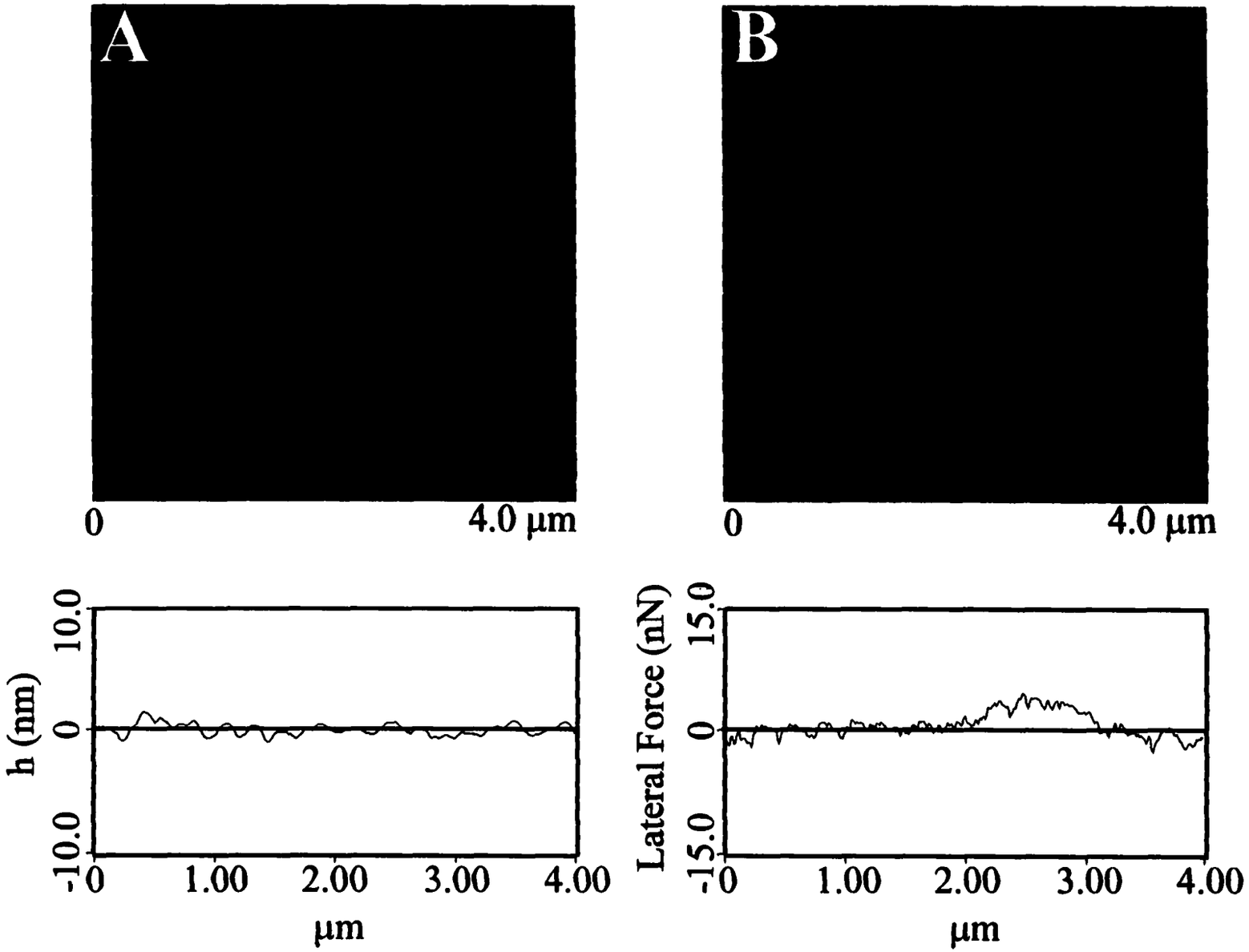
A
0
4.0 µm
B
0
4.0 µm
h (nm)
10.0
0
-10.0
0
1.00
2.00
3.00
4.00
µm
Lateral Force (nN)
15.0
0
-15.0
0
1.00
2.00
3.00
4.00
µm

sectional profile shown in Figure 2B. These images were collected after continually scanning a 1.0 μm x 1.0 μm area that was located slightly to the right of the center of the images for 1 hr at a load of ~25 nN. Both images indicate the presence of large (100-300 nm), atomically smooth terraces.[35] More importantly, the friction image reveals the effect of both the exposure to and repetitive scanning of the sample in the alkaline solution. The latter two observations, which are discussed below, reflect the sensitivity of frictional imaging to changes in chemical composition as demonstrated in Figure 1.

The friction image provides insight into the compositional changes of the sample in two ways. The first insight develops by examining the image outside the repetitively scanned area. This examination reveals the presence of small (50-80 nm), localized regions of high friction (~40 nN) interspersed among identifiable regions of low friction (~30 nN). These differences, which are superimposed on the response originating from changes in topography, reflect the partial conversion (68%) of the DSU monolayer from an ester to carboxylate end group. That is, the regions of high friction correspond to domains in the adlayer composed largely of carboxylate end groups, and the regions of low friction correspond to domains comprised largely of the ester terminus of the unhydrolyzed DSU adlayer.

The second insight, which is of critical importance to our principal assertion, develops from a comparison of the friction observed in the repetitively scanned region to the area surrounding this region. Importantly, the fraction of the area (87%) in the repetitively scanned area with a high friction is identifiably greater than that found in the surrounding region (68%). Thus, the DSU adlayer in the repetitively scanned region is more extensively hydrolyzed than that in the surrounding region.

At issue, then, is how contact imaging enhances the rate of the hydrolytic transformation. We believe that the probe tip induces a localized disorder in the outer portion of the structure of the adlayer. This disorder enhances access of hydroxide ion to the acyl carbon of DSU, which accelerates the hydrolysis in the repetitively scanned area. In other words, the repetitive scanning process results in a *tip-assisted* hydrolysis, with the tip acting like a nanoscale stirring bar.

As a further test of this possibility, we repetitively scanned an area on a freshly prepared DSU monolayer under deionized water (pH 6.2). We note that IRS experiments for samples immersed in deionized water for extended periods of time (e.g., 5 hr) did not detect the presence of a carboxylate species, indicating that the transformation of the ester linkage of DSU is exceedingly slow at pH 6.2. Figures 3A,B present the respective 3.0 μm x 3.0 μm height and friction images obtained after filling the in situ cell of the SFM with deionized water. Next, a 0.50 μm x 0.50 μm region that was located near the center of the images in Figure 3A,B was repetitively scanned at the same rate and load as used for Figure 2. After 1 hr of continual scanning, the scan area was increased to 3.0 μm x 3.0 μm, and the images in Figures 3C,D were acquired. These images, which encompass the repetitively scanned area, are notably devoid of evidence for a change in friction. Importantly, this result shows that the observed change in the friction for the repetitively scanned area in Figure 2B is not from a detectable tip-induced wear of the sample surface.

If, however, the sample in Figures 3C,D is subsequently exposed for 30 min to the alkaline aqueous solution in the absence of scanning, the images in Figures 3E,F are obtained.[36] This exposure results in the appearance of a localized, square-shaped region of

Figure 3. In situ topographic (A) and friction (B) images (3.0 μm x 3.0 μm) and cross-sections of a DSU monolayer chemisorbed at Au(111) in the SFM liquid cell filled with deionized water (pH 6.2); in situ topographic (C) and friction (D) images of the same imaged area in (A) and (B) after repetitively scanning a 0.50 μm x 0.50 μm area located in the center of the images while under deionized water; in situ topographic (E) and friction (F) images of the same area in (A) and (B) after exposing the sample to an alkaline (10 mM KOH) aqueous solution for 30 min (see the caption for Figure 2 for further details).

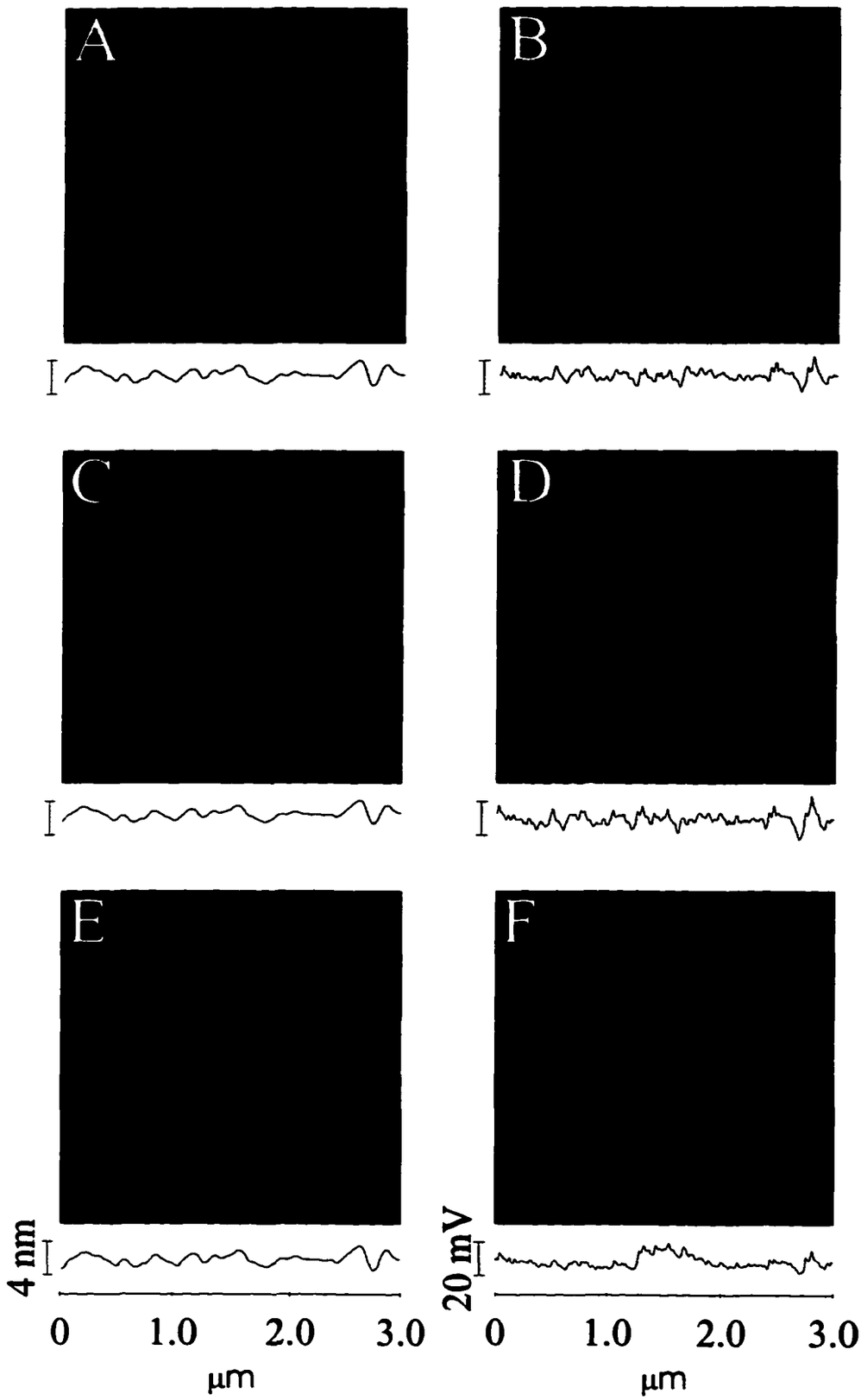
A
B
C
D
E
F
4 nm
20 mV
0
1.0
2.0
3.0
µm
0
1.0
2.0
3.0
µm

high friction that coincides with the location of the repetitively scanned area. In this case, the fraction of the area in the repetitively scanned region with high friction is 95%, whereas that in the surrounding region is 32%. We therefore conclude that the enhanced rate of hydrolysis results from a subtle tip-induced disordering of the outer portion of the DSU adlayer that increases the accessibility of hydroxide ion to the acyl carbon of the buried ester functionality. In support of this interpretation, the first results from ongoing experiments have shown that the tip-assisted enhancement of the hydrolysis rate is dependent on the load such that a higher load increases the enhancement and vice versa.

Conclusions

Studies to delineate the range and scope of this new approach to localized surface modification are underway, driven mainly by the possibility of creating chemically inhomogeneous patterns of nanometer scale dimensions for sensor design. We are particularly interested in defining the lower limit in the size of an area that can be transformed and the conditions requisite to confining the modification to only the repetitively scanned area. We are also pursuing experiments aimed at furthering insight into the extent (e.g., contact area and depth of penetration) of which the tip interacts with the sample surface, and whether solvent uptake (i.e., hydration) in the scanned regions plays a role.

Acknowledgments

This work was supported in part by the Office of Basic Energy Sciences, Chemical Science Division, of the U.S. Department of Energy, the National Science Foundation (BIR-

9601789), and the Microanalytical Instrumentation Center of Iowa State University. The Ames Laboratory is operated for the U.S. Department of Energy by Iowa State University under Contract No. W-7405-eng-82.

References and Notes

(1) Hansma, P. K.; Elings, V. B.; Marti, O.; Bracker, C. E. *Science* **1988**, *242*, 209-216.

(2) Snyder, S. R.; White, H. S. *Anal. Chem.* **1992**, *64*, 116R-134R.

(3) Salmeron, M. B. *MRS Bulletin* **1993**, 20-25.

(4) Louder, D. R.; Parkinson, B. A. *Anal. Chem.* **1994**, *66*, 84R-105R.

(5) Overney, R. M.; Meyer, E.; Frommer, J.; Guntherodt, H. J. *Langmuir* **1994**, *10*, 1281-1286.

(6) Meyer, E.; Overney, R.; Luthi, R.; Brodbeck, D.; Howald, L.; Frommer, J.; Guntherodt, H. J.; Wolter, O.; Fujihira, M.; Takano, H.; Gotoh, Y. *Thin Solid Films* **1992**, *220*, 132-137.

(7) Overney, R. M.; Meyer, E.; Frommer, J.; Brodbeck, D.; Luthi, R.; Howald, L.; Guntherodt, H. J.; Fujihira, M.; Takano, H.; Gotoh, Y. *Nature* **1992**, *359*, 133-135.

(8) Vezenov, D. V.; Noy, A.; Rozsnyai, L. F.; Lieber, C. M. *J. Am. Chem. Soc.* **1997**, *119*, 2006-2015.

(9) Noy, A.; Frisbie, C. D.; Rozsnyai, L. F.; Wrighton, M. S.; Lieber, C. M. *J. Am. Chem. Soc.* **1995**, *117*, 7943-7951.

(10) Frisbie, C. D.; Rozsnyai, L. F.; Noy, A.; Wrighton, M. S.; Lieber, C. M. *Science* **1994**, *265*, 2071-2074.

(11) Wilbur, J. L.; Biebuyck, H. A.; MacDonald, J. C.; Whitesides, G. M. *Langmuir* **1995**, *11*, 825-831.

(12) Williams, J. M.; Han, T.; Beebe, T. P. *Langmuir* **1996**, *12*, 1291-1295.

(13) Han, T.; Williams, J. M.; Beebe, T. P. *Anal. Chim. Acta* **1995**, *307*, 365-376.

(14) Hillier, A. C.; Kim, S.; Bard, A. J. *J. Phys. Chem.* **1996**, *100*, 18808-18817.

(15) Marti, A.; Hahner, G.; Spencer, N. D. *Langmuir* **1995**, *11*, 4632-4635.

(16) Green, J.-B. D.; McDermott, M. T.; Porter, M. D. *J. Phys. Chem.* **1996**, *100*, 13342-13345.

(17) Green, J.-B. D.; McDermott, M. T.; Porter, M. D.; Siperko, L. M. *J. Phys. Chem.* **1995**, *99*, 10960-10965.

(18) Wang, J.; Kenseth, J. R.; Jones, V. W.; Porter, M. D., manuscript in preparation.

(19) Müller, W. T.; Klein, D. L.; Lee, T.; Clarke, J.; McEuen, P. L.; Schultz, P. G. *Science* **1995**, *268*, 272-273.

(20) McIntyre, B. J.; Salmeron, M.; Somorjai, G. A. *Science* **1994**, *265*, 1415-1418.

(21) Xu, S.; Liu, G.-Y. *Langmuir* **1997**, *13*, 127-129.

(22) Wagner, P.; Hegner, M.; Kernen, P.; Zaugg, F.; Semenza, G. *Biophys. J.* **1996**, *70*, 2052-2066.

(23) Nakano, K.; Taira, H.; Maeda, M.; Takagi, M. *Anal. Sci.* **1993**, *9*, 133-136.

(24) Kenseth, J. R.; Jones, V. W.; Porter, M. D., manuscript in preparation.

(25) Tarlov, M. J.; D.R.F. Burgess, J.; Gillen, G. *J. Am. Chem. Soc.* **1993**, *115*, 5305-5306.

(26) Lewis, M.; Tarlov, M. *J. Am. Chem. Soc.* **1995**, *117*, 9574-9575.

(27) Under these conditions, there was no detectable displacement of the carboxylate portion of the patterned surface by solution-based DSU, as judged from IRS.

(28) We have also characterized the base-hydrolysis of several other ester-terminated monolayers, including the methyl, ethyl, and butyl mercaptohexadecanoate. In contrast to a DSU monolayer, the rates for the base-hydrolysis of the latter adlayers were markedly slower and, because of instrumental drift, were not amenable to in situ imaging. For example, the monolayer of the methyl ester required nearly seven days before complete transformation.

(29) Cline, G. W.; Hanna, S. B. *J. Org. Chem.* **1988**, *53*, 3583-3586.

(30) Ryswyk, H. V.; Turtle, E. D.; R.Watson-Clark; Tanzer, T. A.; Herman, T. K.; Chong, P. Y.; Waller, P. J.; Taurog, A. L.; Wagner, C. E. *Langmuir* **1996**, *12*, 6143-6150.

(31) Holmes-Farley, S. R.; Whitesides, G. M. *Langmuir* **1987**, *3*, 62-76.

(32) The torsional response in a SFM friction measurement because of differences in surface composition and packing density can be convoluted with changes in topography and elasticity,[5,10] respectively.

(33) An assessment of the possible change in the orientation of the adlayer as a function of the extent of the hydrolysis, based on the constancy of the relative absorbance of the symmetric and asymmetric carboxylate structures, indicated that such an effect on the compositional analysis is small (i.e. a few percent).

(34) The cross-section analysis was performed by averaging the individual lines in the area bound within the delimiting markers in the images.

(35) Alves, C. A.; Smith, E. L.; Porter, M. D. *J. Am. Chem. Soc.* **1992**, *114*, 1222-1227.

(36) Images encompassing the repetitively scanned area that were acquired immediately after the addition of 10 mM KOH into the in situ cell were also devoid of evidence for a frictional change.

CHAPTER 4. ELECTROCHEMICALLY-BASED TECHNIQUE FOR THE SELECTIVE REMOVAL OF CHLORIDE FROM LIQUID MEDIA

A paper to be submitted to *Analytica Chimica Acta*

Chuanjian Zhong, Jianhong Wang, Shelley J. Coldiron, and Marc D. Porter

Abstract

An electrochemical approach to the minimization of Cl^- interference in the determination of chemical oxygen demand (COD) is described. Two types of highly efficient silver electrodes were employed for the removal of Cl^- from a variety of different samples, including those from a waste treatment plant. Both approaches are based on the electrochemical deposition of Cl^- at silver electrodes. In one configuration, silver was electrochemically deposited onto reticulated vitreous carbon (RVC). The highly dispersive characteristic of the deposited silver films on RVC provided a means to treat large volume samples as well as those with Cl^- levels as high as ~1000 ppm. The configuration uses a silver wire in coil-form. The approach was devised to minimize the entrapment of organic particulates in wastewater samples in the porous cavities RVC.

Chloride removal to levels below 3 ppm, with analysis times of $\leq$ 15 min and COD precision $\leq \pm$ 20%, were demonstrated. Electrode surfaces and their performance in Cl^--

removal were characterized by electrochemical methods, scanning electron microscopy (SEM), and spectroscopic methods such as electron dispersive x-ray spectroscopy (EDS) and x-ray photoelectron spectroscopy (XPS).

To reduce the probability of particulate entrapment or adsorption on the uncoated silver electrodes, which attributed to a loss of ~50% COD from wastewater samples, a new strategy of surface coating was developed. By coating the surface with a low surface free energy layer such as silver sulfide, COD adsorption losses were thus reduced to < 10%, an acceptable level for most applications, while maintaining the same Cl^--removal efficiency as uncoated electrodes. Our results not only demonstrate a new technology for removing chloride in real-world samples for COD analysis, but also probes the fundamental understanding of surface treatment and film growth at a silver electrode.

Introduction

The depletion of dissolved oxygen in surface water arises in large part from the biological and chemical oxidation of organic and inorganic contaminants present in the matrix. Such processes can give rise to detrimental conditions for fish and aquatic plant life. A determination of the oxygen demand in water and wastewater is therefore an important figure of merit for evaluating water quality. There are numerous methods for the determination of oxygen demand,[1] including biological oxygen demand (BOD), chemical oxygen demand (COD), and total organic carbon (TOC).[2,3] Of these methods, COD is often the most utilized. This situation reflects the procedural simplicity of COD over the other methods and the reliability of COD as a measure of the oxygen demand in an ecosystem.

The general procedure in a COD determination involves the oxidation of the organic species in a sample by dichromate in a heated solution of concentrated sulfuric acid, followed by colorimetric determination of residual dichromate. The determination is, however, susceptible to interference by Cl^-. This species is readily oxidized by dichromate under the noted digestion conditions. A common method for minimizing the interference of Cl^- is the addition of mercuric sulfate to the sample prior to digestion to form a soluble complex with Cl^-.[1] This approach, while proving very effective suffers from the obvious environmental and health problems associated with mercury. There are only a few accounts for the removal of Cl^- by approaches that are potentially "greener" than the mercury based method.[4-11] A few examples are: the use of an equivalent concentration of $AgNO_3$ solution to precipitate chloride as AgCl;[4-6] addition of concentrated sulfuric acid to evolve Cl^- as HCl gas;[7,8] and oxidation of Cl^- to Cl_2 in the dichromate reflux followed by back-titration in acid potassium iodide solution vs. standard sodium thiosulfate solution to arrive at a chloride correction.[9] Most of these methods have not been successfully put into practice.

In this paper, we describe a novel alternative for the removal of Cl^- from samples prior to a COD determination. Our approach is based on the electro deposition of chloride as shown in equation 1.

$$Ag + Cl^- \rightarrow AgCl + e^- \quad (E^0=0.2\ V(vs.\ SHE)) \qquad (1)$$

Preparation of Ag/AgCl reference electrodes based upon this reaction has been practiced in electrochemistry-related fields for decades.[12] Typically, in KCl or HCl, films of AgCl are deposited by applying an anodic voltage or current to a Ag electrode. Fundamental aspects

of this reaction such as the film (monolayer and multilayer) formation and reaction mechanisms have been studied extensively.[13-15]

To estimate the feasibility of the proposed Cl^- pretreatment method, the following assumptions are made: an electrode surface area of ~100 cm^2, a full AgCl monolayer AgCl of $1x10^{-9}$ moles/cm^2, and a calculated charge of ~10 mC. Under these conditions, a deposition of 2700 monolayers of AgCl (27 °C) is required for complete removal of Cl^- from a 10 ml solution of 1000 mg/L Cl^-. Since it has been reported that 1.14 C/cm^2 can be passed across an electrode surface to form conductive AgCl films[13] (translating to 11800 monolayers at 100% efficiency) the use of Ag for the electrodeposition of chloride is feasible. Considering concentration as a function of time during controlled potential electrolysis, the following expression describes the process under stirring conditions:[16]

$$Q(t) = VC_0nF\left[1-\exp(-\frac{AD}{V\delta})t\right] \qquad (2)$$

where Q(t) is the charge passed at time t, V is the sample volume, C_0 is the initial Cl^- concentration, n is the electron transfer number, A is the electrode surface area, D is the diffusion coefficient, δ is the diffusion layer thickness at a defined stirring rate and F is Faraday constant. Thus for C=1000 mg/L (0.028 M) and V=10 mL, with typical parameters of $D=10^{-5}$ cm^2/s and $\delta= 3x10^{-3}$ cm, the time required to remove chloride is only ~3 min (using $d= 3x10^{-2}$ cm for a more conservative estimate, it is ~25 min). This time frame is reasonable for most applications.

This paper describes two highly efficient procedures for the electrochemical removal of Cl^-. The first procedure employs reticulated vitreous carbon (RVC) treated by

electrochemical deposition of silver. RVC is characterized by its high electrical conductivity, chemical inertness (e.g., high resistance to oxidation), low heat capacity, large surface area with self-supporting rigidity, and low resistance to fluid flow.[17,18] Highly dispersive (i.e., high surface area), strongly adhesive, and comparatively uniform silver films were deposited on the RVC to form an electrode. The electrode and its performance in Cl^- removal were characterized by scanning electron microscopy (SEM) and electrochemical methods. Chloride removal to levels below 3 ppm were demonstrated with initial Cl^- concentrations ranging from 100 to 1000 ppm. Our target parameters were: Cl^- removal to $\leq$ 10 ppm, analysis time $\leq$ 15 min, and COD analysis precision $\leq \pm$ 20% (including Cl^- pretreatment).

Development of the second procedure was primarily predicated by two factors: field-practice needs to minimize sample volume with a reduction in reagent consumption and the need to surmount problems of entrapped organic particulates in RVC. Employing a Ag-coil as an electrode, sample volumes were readily reduced from 5 mL to 0.5 mL with comparable efficiencies as the Ag/RVC method. In this configuration, the probability of particulate entrapment is reduced. However, a loss of ~50% COD from sewage water samples following Cl^- pretreatment was observed using the bare Ag coil. This was attributed to the sorption of solid organic particulate onto the electrode. To compensate for this problem, we took a novel approach by coating the silver surface with a low surface free energy layer such as silver sulfide. By electrochemically coating the surface with Ag_2S, COD adsorption losses were reduced to < 10%, an acceptable level for most applications. Our results not only demonstrate a new technology for removing Cl^- in real-world samples for COD analysis but

also probe the fundamental understanding of surface treatment and film growth at a silver electrode.

Experimental Section

Materials and Chemicals. Reticulated Vitreous Carbon (RVC) was purchased from Electrosynthesis Co. Inc., with porosity grades ranging from 20 to 100 ppi (pores per inch). Silver wire (diameter: 0.04 mm), KCl, KNO_3, NH_4OH, NaOH, Na_2SO_4 and Na_2S were obtained from Fisher; Ag_2SO_4 and KCN were from Aldrich; $AgNO_3$ was from J. T. Baker, and KHP (potassium acid phthalate, 1000 mg/L COD standards) was obtained from Hach. Sewage samples were collected from Ames Waste Control Facility at Cambridge, IA. Sample designations in treatment sequence order are as follows: (1) RAW - waste stream at point of entry to the treatment plant; (2) PC - wastewater following a primary clarifier for removal of large particulates; and (3) TF - wastewater after passing through a trickling filter for removal smaller particulate.

Electrochemical Cell Configurations. Two different cell configurations were tested. The first configuration consisted of a RVC working electrode, a reference electrode (Ag/AgCl/sat'd KCl), and a coiled Pt counter electrode. The electrodes were coaxially assembled in a single-compartment cell (cell volume ~10 mL). The second configuration was comprised of a two-compartment cell (Figure1). The counter electrode was separated from the working cell by a porous glass-frit, thereby eliminating the movement into the sample solution of reaction products (e.g., H_2 gas) that are generated at the counter electrode. With the two-compartment configuration, cells were constructed for two sample volumes of

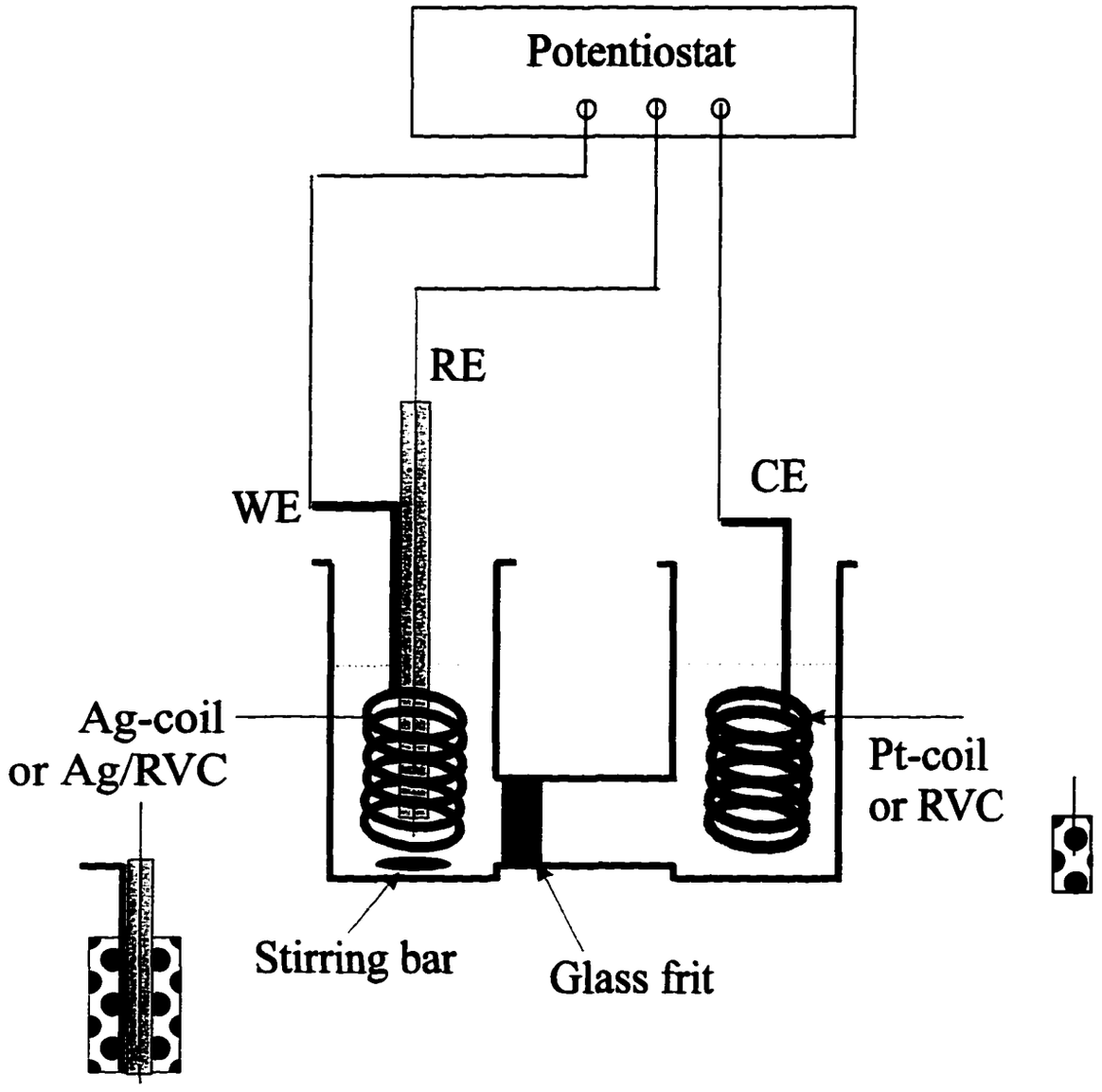

Figure 1. Configuration of a two-compartment cell. The counter electrode is separated from the working cell by a glass-frit, which eliminates the movement of reaction products (e.g., H_2 gas) at the counter electrode into the sample solution. For the Ag/RVC electrode, the cell diameter is ~1.5 cm, and the electrode is 0.7 cm in diameter and 1.27 cm in length. For the Ag-coil electrode, the cell diameter is ~0.7 cm with a sample volume of 0.5 mL and constructed with 0.04-cm diameter wire with ~10 turns.

5 mL (dia. ~1.5 cm) and 0.5 mL (dia. ~0.7 cm), respectively for the large and small COD sample volumes.

Preparation of Ag Electrodes. The Ag/RVC electrodes were configured from a RVC core (diameter: 0.7 cm and length: 1.27 cm). The corresponding surface area was roughly 20 to 40 cm^2.[17,18] Silver was electrochemically deposited on the RVC by immersing the core into 50 mM $AgNO_3$/0.1 M aqueous ammonium and applying two types of potential waveforms across the electrode: (1) stepping from open circuit potential (OCP) to a constant potential (constant potential method); and (2) applying a 2 Hz square waveform until passage of ~1 Coulomb, followed by a constant voltage until passage of an additional ~7 Coulombs (potential pulsing method).

Silver coil electrodes were constructed of 0.04 mm diameter wire with ~10 turns (the surface area was 2~3 cm^2). The electrodes were pretreated by polishing the wire to expose a fresh reactive silver surface. All electrodes were thoroughly rinsed before use.

Electrochemical Characterization. With the above electrode and cell configurations, Cl^- was removed by applying a constant potential to the electrode in the sample solution under constant stirring (magnetic stir plate). The kinetics of the Cl^--removal was followed by recording the charge passed (Q) vs time. The Cl^- concentration was determined by a Cl^--selective electrode (a detection limit of ca. 3 ppm). Cyclic voltammetry (CV) was performed with a Ag-wire tip (diameter: ~0.04 mm and length: ~0.3 cm) as the working electrode. All experiments were performed at ambient conditions.

Instruments. A potentiostat (Model 173) and charge integrator (Model 179) were from Princeton Applied Research; a different potentiostat (Model CV27) was from

Bioanalytical Systems Inc. (BAS); a wave generator (Model 145) was from Wavetek; a recorder (Model 200) was from Recorder Company; an oscilloscope (Model 2221) was from Tektronix 2221; and a chloride electrode (Model 9617BN) was from Orion Research, Inc. A JSM-840A Scanning Microscope was used for SEM imaging and Electron Dispersive X-ray Spectroscopy (EDS) (Jeol Instruments). Hach's COD reactor (Model 45600) was employed for COD measurements.

Results and Discussion

This section is divided into three parts. The first part establishes the electrochemical Cl^--removal method by studying the efficiencies and conditions of the silver electrodes in standard Cl^--containing solutions. Both the Ag/RVC and Ag-coil electrodes were examined in large and small sample volumes, respectively. The dependence of the surface morphology of Ag films on RVC was characterized by SEM. The second part investigates the use of Ag/RVC in removing Cl^- from large sample volumes of sewage water samples and the effect on COD analysis. In the last part, the use of the silver coil electrode was investigated for small sample volumes. A surface coating technology using Ag_2S on silver was developed to minimize the adsorption of organic particulate onto the Ag-coil electrode while offering efficient Cl^--removal. Satisfactory Cl^--removal and COD results were obtained by using this technology, as will be described in detail in part 3 of this section.

Electrochemical Cl^- Removal. It is known from the Nernst equation (Equation 3) for the electrode reaction in Equation 1:

$$E = E^0 - (RT/nF) \ln [Cl^-] \quad (3)$$

that the redox potential shifts negatively with increasing Cl^- concentration. The cyclic voltammograms (CV) and their peak characteristics obtained in solutions of varying Cl^- concentrations with a Ag-coil electrode are presented in Figure 2 and Table 1. These data

Table 1. Voltammetric Peak Characteristics of Ag Coil Electrodes (with 0.1 M Na_2SO_4)

Electrolyte	E_{pa} (V)	E_{pc} (V)	ΔE_p (V)	E_0^* (V)
0.003 M KCl	0.31	0.04	0.27	0.18
0.01 M KCl	0.25	0.01	0.24	0.13
0.03 M KCl	0.29	-0.12	0.41	0.09

demonstrate the oxidation/reduction concentration dependence of the system. By applying a constant potential at the voltammetric oxidative current inflection region, Cl^- is deposited as AgCl onto the electrode. Chloride deposition can be monitored as a decrease of the ion concentration in solution using a chloride selective electrode. Our experiments have firmly established that the electrical charge passed during electrolysis corresponds to the amount of Cl^- removed from solution. This can be quantitatively affirmed (±10%) with the simple relation of:

$$Q_{Total} = V_{soln} F C_{Cl^-} \quad (4)$$

where Q_{Total} is the total charge passed during the electrolysis, F is the Faraday constant, and C_{Cl^-} is the concentration of chloride ion prior to its deposition as AgCl. To achieve maximum Cl^- deposition, the applied potential is chosen based on the initial Cl^--solution concentration

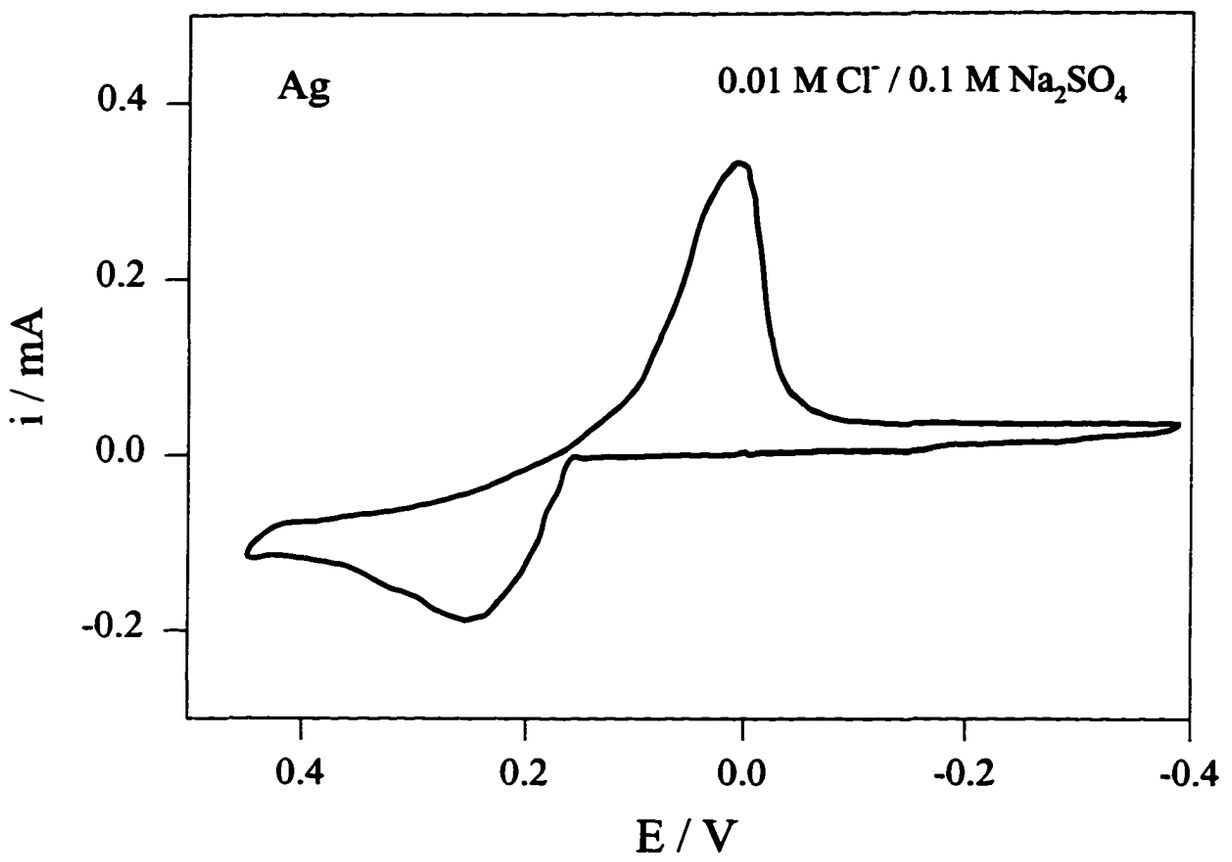

Figure 2. Cyclic voltammogram (CV) of Ag electrode in Na_2SO_4 electrolyte containing Cl^-. Scan rate: 50 mV/sec.

(deposition potential shifts as a function of Cl^- concentration). At potentials < E_{pa} (the anodic peak potential), Ag was at non-detectable levels in solution, as confirmed by inductively coupled plasma (ICP-AES) analyses (<1 ppm). Potentials at which CV diffusional tails are depicted lead to fast reaction and diffusion rates resulting in the formation of AgCl in bulk solution instead of at the electrode surface.

Typical examples of chronocoulometric curves for both configurations, Ag/RVC and Ag-coil, are shown in Figure 3 to demonstrate AgCl deposition and Ag regeneration. The reversibility of the process is evident by the mirror-image of the shapes and magnitudes of the curves for deposition and regeneration. Chloride mass balance was confirmed by monitoring the concentration profile during deposition and regeneration.

The active surface area of a Ag deposited RVC electrode was expected to be dependent on the deposition conditions such as potential waveform, electrolyte, and concentration of Ag^+. Figure 4 provides a comparison of the Cl^--removal rates for Ag films prepared by the two electrode preparation methods described in the experimental section: the constant potential method (curve 1, °) and the potential pulsing method (curve 2, •). The dashed lines were theoretically calculated for Cl^--removal using two different surface areas according to Equation 2. This comparison demonstrated a higher Cl^--removal efficiency with the films grown using the pulsed potential waveform, as indicated in curve 2. Agreement between theoretical and experimental data revealed that the effective surface area of silver films prepared by potential pulsing was dramatically increased (as will be further supported by subsequent SEM images) over those by the constant potential method. We have found,

Figure 3. Typical examples of the charge-time curves of the two steps in our electrochemical Cl^--removal method. (A) (1) AgCl deposition in 355 ppm KCl/0.1 M KNO_3, and (2) Ag regeneration in 0.1 M KNO_3; (B) A typical example of the chronocoulometric charge-time curves of the two steps in our electrochemical Cl^--removal method using Ag-coil electrode: (1) AgCl deposition in 1065 ppm KCl/0.1 M Na_2SO_4, and (2) Ag regeneration in 0.1 M Na_2SO_4.

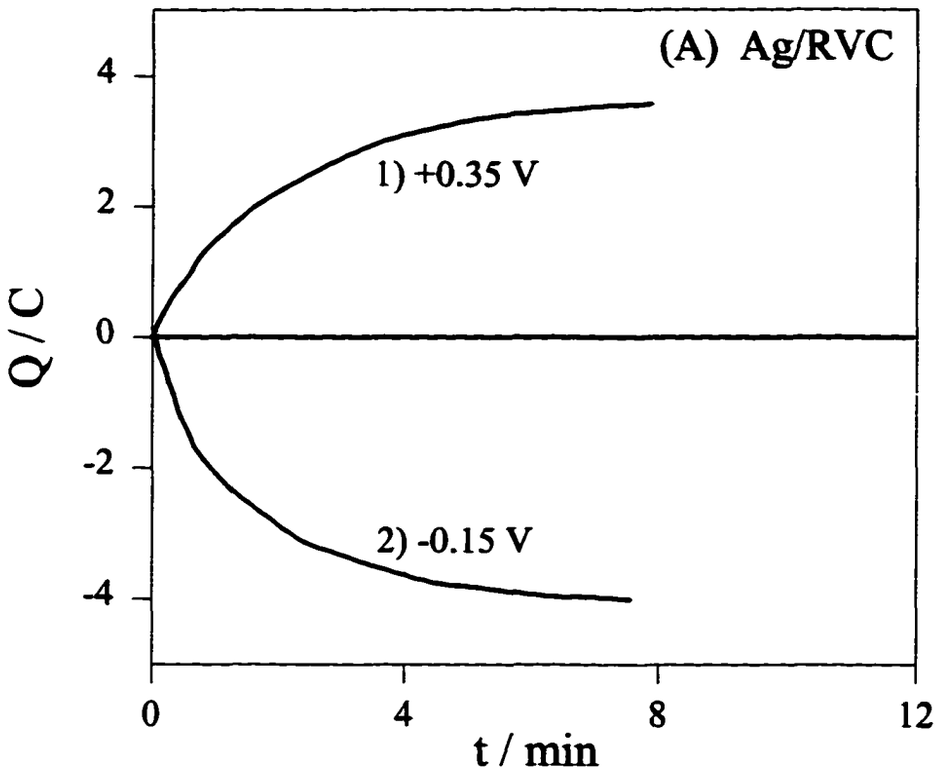
(A) Ag/RVC
1) +0.35 V
2) -0.15 V
Q / C
t / min
4
2
0
-2
-4
0
4
8
12

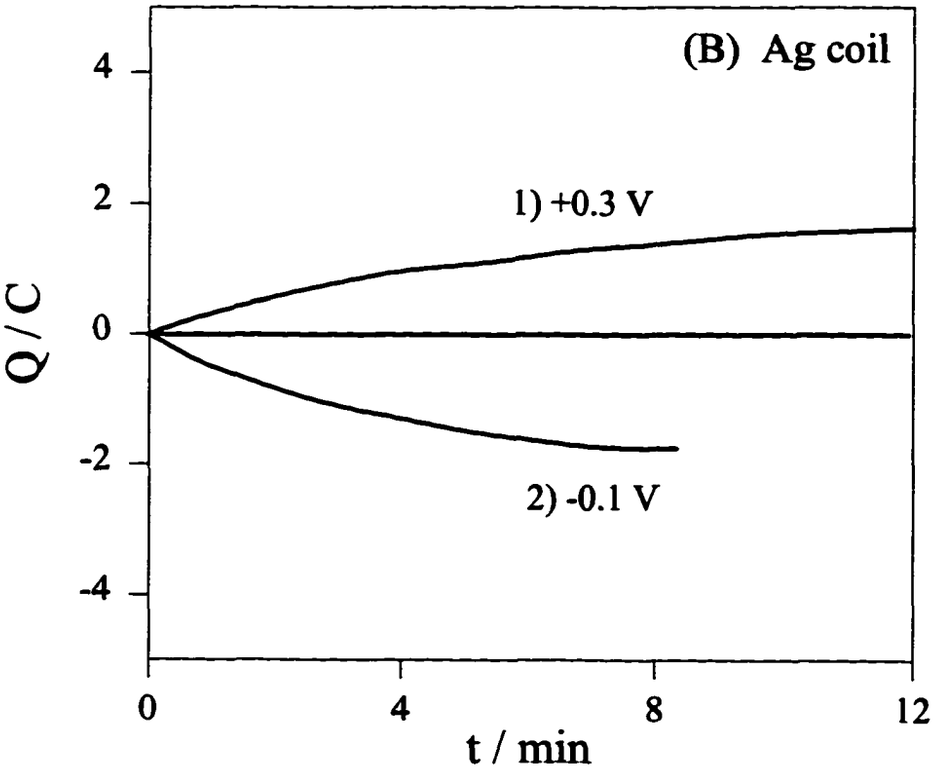
(B) Ag coil
1) +0.3 V
2) -0.1 V
Q / C
t / min
4
2
0
-2
-4
0
4
8
12

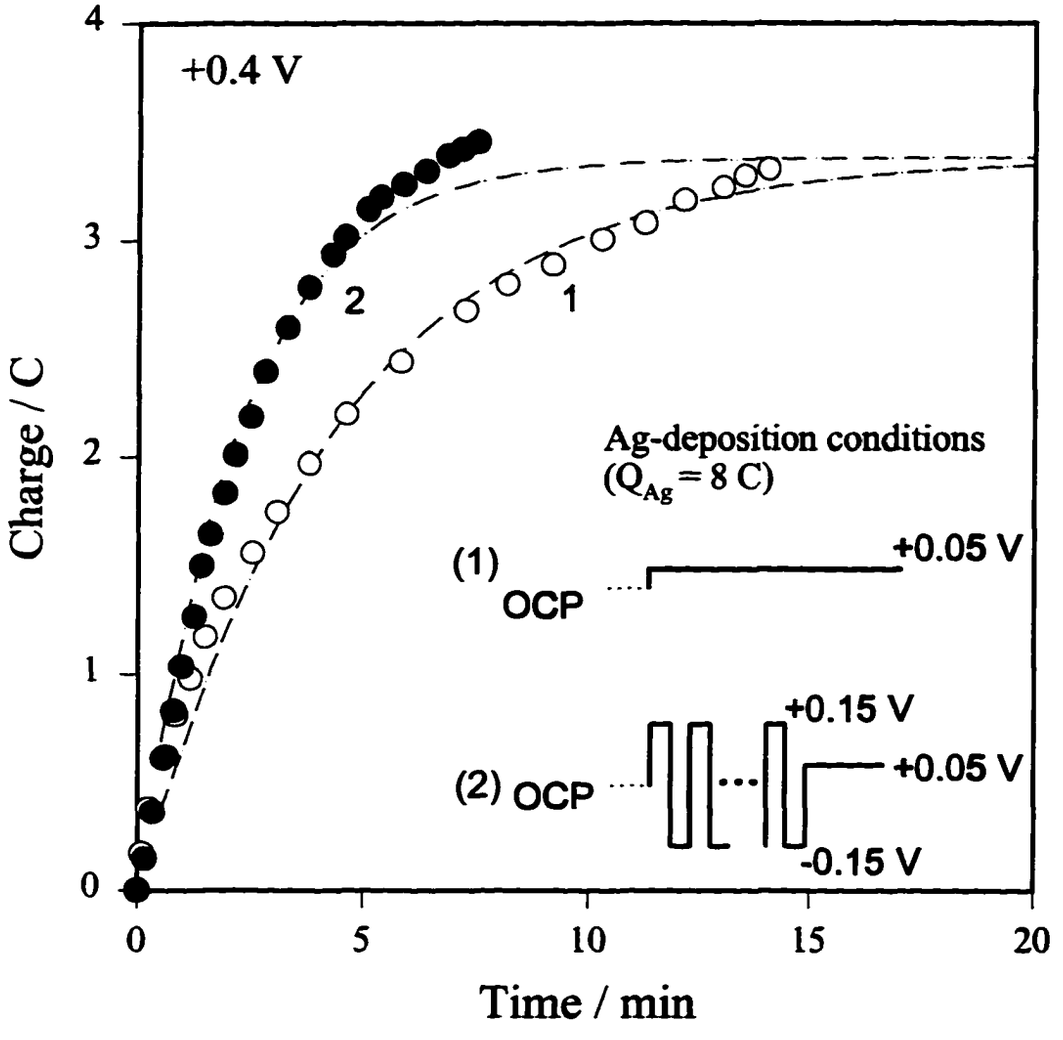

Figure 4. Cl^--removal rates for Ag films prepared by two methods: (curve 1, °) stepping from open circuit potential (OCP) to a constant potential; (curve 2, •) applying a 2 Hz square waveform until passage of ~1 Coulomb, followed by a constant voltage until passage of an additional ~7 Coulombs. The later is the procedure used in preparing the Ag films, and is dubbed the potential pulsing method. The dashed lines are theoretically calculated according to Equation 2 using two different surface areas. In both cases, a constant stirring rate was maintained.

however, that pulses at too high of an overvoltage (e.g., ≤ -0.2 V) can lead to poor adhesion of the silver film to RVC.

Remarkable surface morphology differences were revealed by SEM for the silver films deposited by the two methods. The SEM images presented in Figures 5A and 5B compare: (1) surface morphologies of the silver films prepared by using the constant potential method (A) and the potential pulsing method (B); and (2) the surface morphology changes from the freshly formed Ag film to the AgCl film and to the regenerated Ag film. The films are comprised of comparable amounts of deposited silver, as controlled by the charge passed during electrodeposition. The highly dispersive characteristics of silver on RVC are clearly shown at the film surface prepared by the potential pulsing method. The increase in particle size and the formation of pores upon the initial transformation from Ag to AgCl reflects the uptake of Cl^- and the subsequent irreversible expansion of the microstructure of the film. Moreover, the film after ~20 cycles between AgCl and Ag (i.e., image d of Figure 5B) appears similar to that after one cycle, demonstrating the durability of the film.

We examined the ability to reuse the electrodes and found that we were able to regenerate the electrode surface by cycling between AgCl and Ag using a square voltage waveform. By comparing the charge transients between anodic (AgCl formation process) and cathodic (Ag regeneration), as well as monitoring Cl^- uptake and release, electrode performance was evaluated. There was a slight performance degradation of the electrode after numerous recycling efforts (e.g., 50 cycles), which was reflected as a decrease of the reaction rate. We attributed this effect to a change in film porosity, as shown in the SEM

Figure 5A. SEM images of silver films prepared by using the constant potential method; and changes of surface morphologies from (a) the freshly formed Ag film, (b) the AgCl film, (c) the regenerated Ag film, and (d) the regenerated Ag film after ~20 cycles. All these films have the same approximate amount of deposited silver, as controlled by the charge passed during electrodeposition.

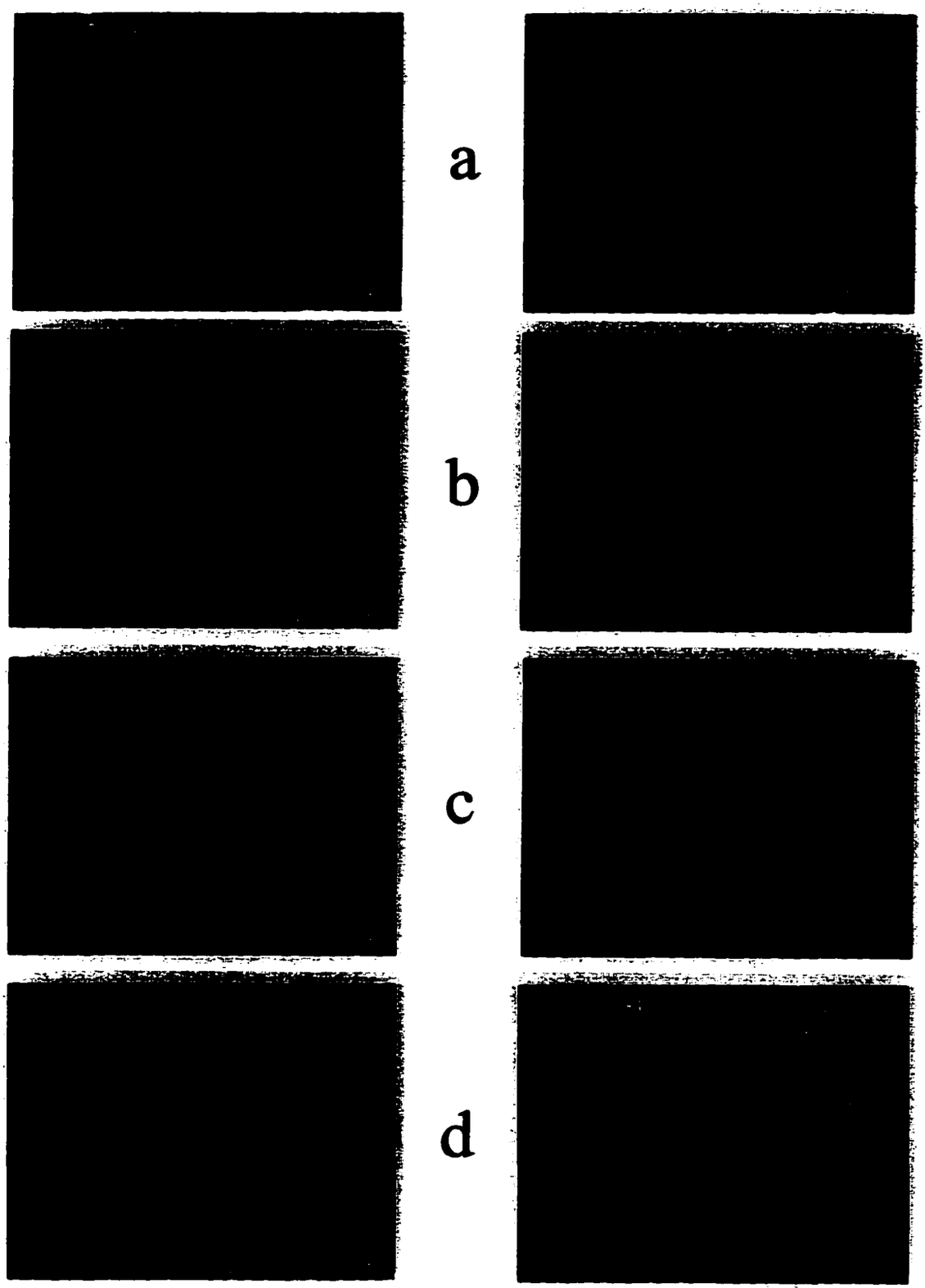
a
b
c
d

Figure 5B. SEM images of silver films prepared by using the potential pulsing method; and changes of surface morphologies from (a) the freshly formed Ag film, (b) the AgCl film, (c) the regenerated Ag film, and (d) the regenerated Ag film after ~20 cycles. All these films have the same approximate amount of deposited silver, as controlled by the charge passed during electrodeposition.

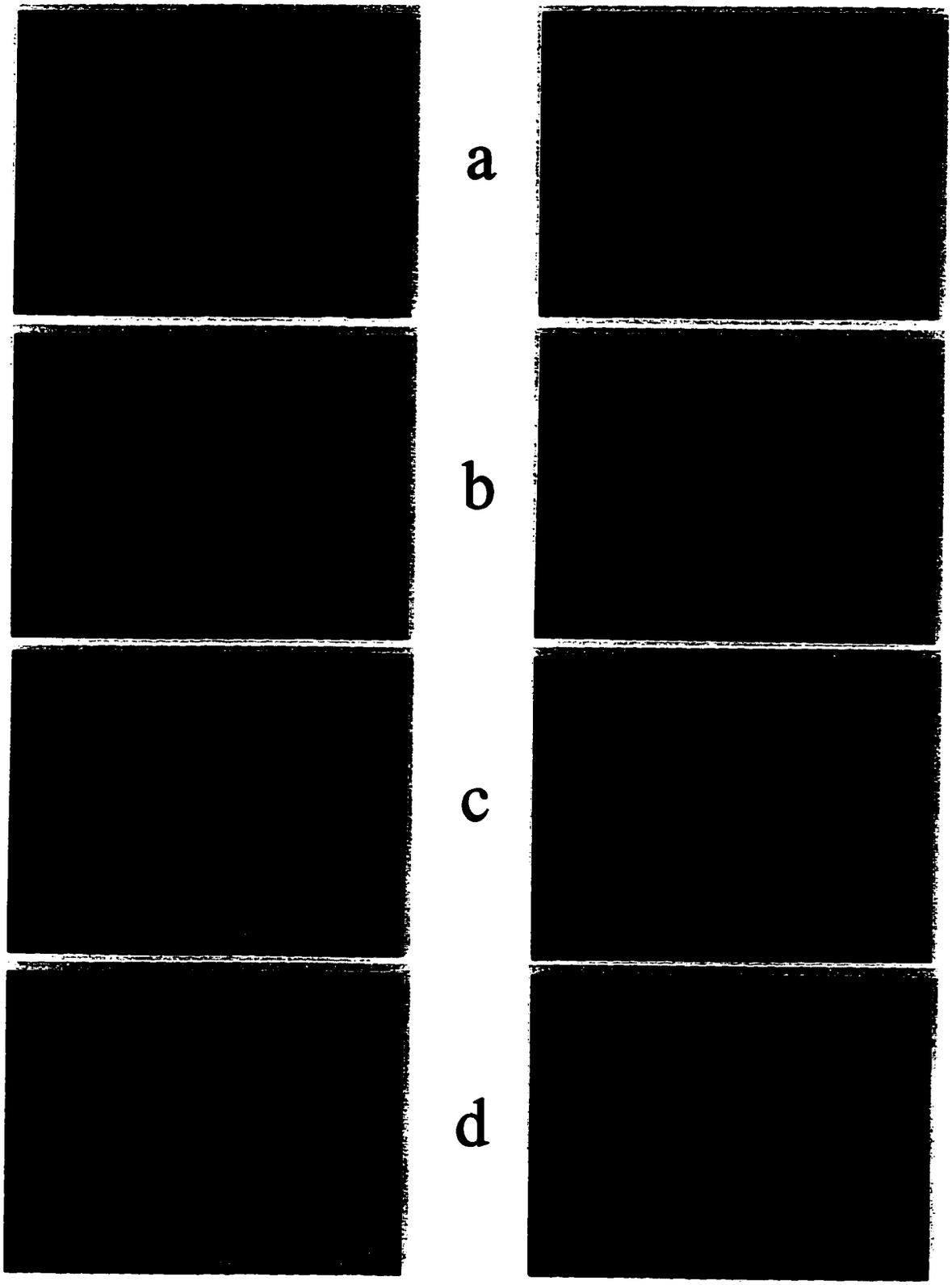
a
b
c
d

results. However, by extending the electrolysis time, an equivalent charge can be passed without affecting the Cl^--removal efficiency.

The two electrode configurations were highly efficient in removing Cl^- from standard solutions ranging in concentration of 100 - 1000 ppm Cl^- to levels typically below 10 ppm (Table 2). The time required for Cl^--removal was generally below 15 min, and the amount of charge passed corresponded to the initial Cl^- concentration.

Cl^--Removal and COD Analysis for RVC Electrode. We examined the effects of RVC electrode pretreatment upon COD analysis. Standard COD solutions were used as controls and consisted of KHP, Cl^- (low levels, i.e., $\sim\leq$100 ppm), and low ionic strength. Low solution conductivity (i.e., low supporting electrolyte) posed two problems: (1) solution migration through the glass-frit to the counter electrode compartment via electroosmosis (15% volume changes were sometimes observed); and (2) slow electrolysis due to large voltage drops across the solution. Both problems were minimized by adding 0.01 M to 0.05 M supporting electrolyte (e.g., KNO_3).

Another problem, however, arose with low level Cl^- solutions, as indicated by the transition of the solution from transparent to translucent during the electrolysis. This was a result of the rapid conversion of Ag(0) to Ag^+ as compared to the slow deposition of AgCl via Equation 1. Two approaches were tested to overcome this complication: (1) pre-coating the Ag/RVC with a small amount AgCl; and (2) initially applying a lower overpotential, which was gradually increased. Both processes successfully corrected the limitation, but required a slightly longer (but acceptable) time length (< 15 min) for the complete removal of

Table 2. Cl^- Removal in Standard Cl^- Solutions

Sample	$[Cl^-]_{initial}$ (ppm)	Potential (V)	Time (min)	Charge (C)	$[Cl^-]_{final}$ (ppm)
		Ag / RVC (80 PPI)			
0.01 M KCL (0.0150 M)/0.05 M H_2SO_4 (4.0 mL)	530	+0.35	16	4.032	3
0.01 M KCl (0.0150 M)/0.05 M H_2SO_4 (4.0 mL)	530	+0.40	11	3.562	< D.L.
0.0345 M KCl/0.05 M H_2SO_4 (3.5 mL)	1225	+0.40	30	8.202	32
		Ag coil			
0.03 M KCl / 0.1 M Na_2SO_4 (0.5 mL)	1065	+0.30	12	1.720	7
0.01 M KCl / 0.1 M Na_2SO_4 (0.5 mL)	330	+0.30	7	0.610	11
0.003 M KCl / 0.1 M Na_2SO_4 (0.5 mL)	128	+0.225→ 0.30	7	0.210	< D.L.

Cl^-. The results listed in Table 3 indicate an average COD deviation of ~10%. Tap water was also examined to demonstrate the Ag/RVC method applicability to samples relatively free of particulates.

Sewage water samples were tested for Cl^--removal and the results are listed in Table 4. Compared with the standard KHP sample, the sewage water samples showed an unacceptable decrease in the COD values after Cl^--removal. We assumed that this large deviation arised from the adsorption of organic particulate species onto the electrodes, as was evident with SEM. The next section discusses our approach using surface coating technology to minimize the adsorption problem.

Table 3. COD Results in Standard COD Samples (KHP) and Tap Water (3.5 mL)

Sample comp.	$[Cl^-]_{initial}$ (ppm)	Applied Potential (V)	Electrolysis Time (min.)	Charge passed (C)	$[Cl^-]_{final}$ (ppm)	COD (ppm) (before)	COD (ppm) (after)	D[a] (%)
S[b]	142	+0.35	11	1.09	7	300	311	+4
S + 0.05 M KNO_3	71	+0.35	5	1.01	3	300	265	-12
S + 0.01 M KNO_3	128	+0.35	7	1.00	3	300	269	-10
tap water	36	+0.20→0.30	8	0.238	3	13	11	-15

[a] Deviation
[b] COD standard solution

Table 4. COD Results of Using Ag/RVC Electrode in Sewage Samples

Sample comp.	$[Cl^-]_{initial}$ (ppm)	Applied Potential (V)	Electrolysis Time (min.)	Charge passed (C)	$[Cl^-]_{final}$ (ppm)	COD (ppm) (before)	COD (ppm) (after)	D[a] (%)
RAW	96	+0.35	14	0.745	3	209	115	-45
RAW	96	+0.25→0.30	16	0.712	3	181	71	-61
PC	89	+0.35	14	0.725	3	120	40	-67
PC	89	+0.25→0.28	15	0.743	3	128	49	-62
TF	89	+0.40	9	0.840	3	96	48	-50
TF	89	+0.25→0.32	15	0.750	3	100	47	-53

[a] Deviation

Cl^--Removal and COD Analysis for Ag-Coil Electrode. The high surface free energy of silver, which promotes the adsorption of organic particulate (probably surfactants) on silver surface, was believed to be the primary cause of the observed COD negative deviation. It is known that anodic films on metal electrodes (e.g., oxides or salts) can reduce

the surface free energy of the metal electrode.[19] For metal-electrolyte interfaces, the surface free energy is on the order of ~10^3 erg/cm^2, while the free energies at anodic film-water interfaces are on the order of 10^2 erg/cm^2.[19] Modification of an electrode surface with a lower surface free energy coating was taken as an approach for minimizing the adsorption of organic particulate. Silver sulfide films were found to minimize particulate adsorption while still offering high Cl^--removal activity. Additionally, to reduce reagent consumption, the use of a silver coil electrode with lower sample volumes (<0.5 mL) was examined.

Table 5 compares Cl^--removal and COD analysis results with and without added supporting electrolytes in three types of COD sewage samples. The COD results generally showed negative deviations ranging from -10 to -55%. The addition of 0.1 M Na_2SO_4 electrolyte noticeably reduced the time for Cl^--removal, ≤ 5 min. In some cases the electrode was reused (up to 7 times for samples with low Cl^- concentrations) without the need to regenerate Ag. The wide range of [COD] deviation (-9% ~ -55%) was further evidence of particulate adsorption at the electrode surface.

Our initial efforts to overcome the adsorption problem with AgO/Ag_2O-coatings and AgCl surface treatment to lower surface free energy were not successful. Further investigations found that electrochemical treatment to form a Ag_2S-coating gave the best performance, as evidenced by COD deviations on average of <10% (Table 6). To form the Ag_2S coating, a ~50 mM Na_2S solution with 0.1 M Na_2SO_4 was used under unstirred condition; the applied stepped potentials (and charge passed) were, in sequence) -0.35 V (1.5 C) → -0.9 V (-1.5 C) → -0.35 V (1.5 C). Based upon Cl^--removal times of ~5-6 min, the charge passed, and the final Cl^--concentration, we concluded that the Ag_2S coating did not

Table 5. COD Results of Using Ag-Coil Electrode in Sewage Samples (0.5 mL)

Sample	Potential (V)	Time (min)	Charge (C)	COD (bef.) (ppm)	COD (aft.) (ppm)	Deviation (%)
RAW[a]	+0.25→0.30	13	0.140	132	68	-48
PC[a]	„	10	0.098	100	86	-14
TF[a]	„	9	0.110	68	40	-41
PC/0.04 M H_2SO_4	+0.25	5	0.096	80	36	-55
PC/0.013 M KCl	+0.20	18	0.540	80	46	-42
PC/0.02 M KNO_3	+0.25→0.30	6	0.064	152	118	-22
PC/0.02 M Na_2SO_4	+0.30	7	0.075	152	128	-16
PC/0.1 M Na_2SC_4	+0.25→0.30	5	0.110	94	70	-26
RAW/0.1 M Na_2SO_4	+0.25→0.30	4	0.130	113	71	-37
TF/0.1 M Na_2SO_4	„	5	0.120	44	40	-9

[a] The initial Cl^- concentration is ~90 ppm

interfere with the Cl^--removal activity. Blank experiments indicated that there were no significant levels of S species released from the electrode surface during Cl^--removal, which otherwise could contribute to COD.

Experimental data indicate that length of time required for Cl^--removal to < 10 ppm is directly related to the initial Cl^- concentration (e.g., 5 min for 90 ppm, 8 min for 360 ppm and 12 min for 900 ppm). The general deviation for COD analysis following Cl^--removal pretreatment was negatively proportional to Cl^- concentration (e.g., -10% for 90 ppm, -13%

Table 6. COD Results of Using Ag_2S/Ag Electrode in Sewage Samples (0.5 mL with 0.1 M Na_2SO_4 as Supporting Electrolyte)

Sample	Potential (V)	Time (min)	Charge (C)	COD(bef.) (ppm)	COD(aft.) (ppm)	Deviation (%)
0.0036 M KCl	+0.25→0.30	10	0.18	28	28	0
,,	,,	10	0.19	28	24	-14
RAW[a]/0.0025 M Cl^-	0.25→0.30	5	0.15	136	128	-6
,,	,,	5	0.12	144	124	-14
,,	,,	5	0.12	140	124	-11
,,	,,	5	0.12	136	140	+3
,,	,,	5	0.12	140	96	-31
,,	,,	5	0.12	128	116	-9
RAW/0.0025 M Cl^-	,,	5	0.13	160	144	-10
,,	,,	5	0.12	152	120	-21
,,	,,	6	0.12	140	144	+3
PC[a]/0.0025 M Cl^-	,,	6	0.12	124	120	-3
,,	,,	6	0.12	124	128	+3
,,	,,	6	0.12	136	116	-15
RAW/0.01 M Cl^-	,,	8	0.79	136	120	-12
,,	,,	13	0.75	,,	116	-15
RAW/0.025 M Cl^-	+0.30	10	1.84	128	92	-28
,,	,,	11	1.82	,,	96	-25
,,	,,		1.80	,,	100	-22

[a] The initial [Cl^-] is ~90 ppm

for 360 ppm and -25% for 900 ppm). We believe this relationship can be attributed to particulate adsorption at a higher free energy surface resulting from the growth of AgCl onto the Ag_2S-film. SEM images of the surface support this interpretation.

At ~100 ppm Cl^-, the Ag_2S-coated electrode can be used at least 6 times without significantly affecting COD analyses before regeneration. The regenerated electrode can be re-coated with Ag_2S with minimal performance degradation. Repetitive cycling (> 60 cycles) did not significantly affect the Cl^--removal efficiency of the electrode, but surface morphology was found to be changed with the growth of AgCl/Ag onto the Ag_2S film, as evidenced by SEM/EDS.

The electrochemical behavior of Ag_2S films was characterized by cyclic voltammetry. Compared with the electrochemical behavior for an uncoated Ag electrode, the redox potential and current of the Ag/AgCl reaction basically remained unchanged, as evidenced in Figure 6 and Table 7. These results are strong evidence of the unchanged thermodynamic equilibrium for the AgCl/Ag reaction of Equation 1. The decrease of the peak separation was probably a result of the mass transport through the porous and ionic coating. We believe that the silver sulfide film is a non-continuous film, similar to silver chloride.[19] Unlike continuous films such as silver oxide,[19] which require high electric fields to overcome its high ionic resistance, the non-continuous films usually have very low resistance to ion transport so that the redox equilibrium potential stays close to E^0.

Further support comes from SEM images and EDS analysis. The SEM images presented in Figure 7 and the EDS data listed in Table 8 compare the surface morphologies and the compositions of the Ag_2S-coated electrode before and after Cl^--removal operations.

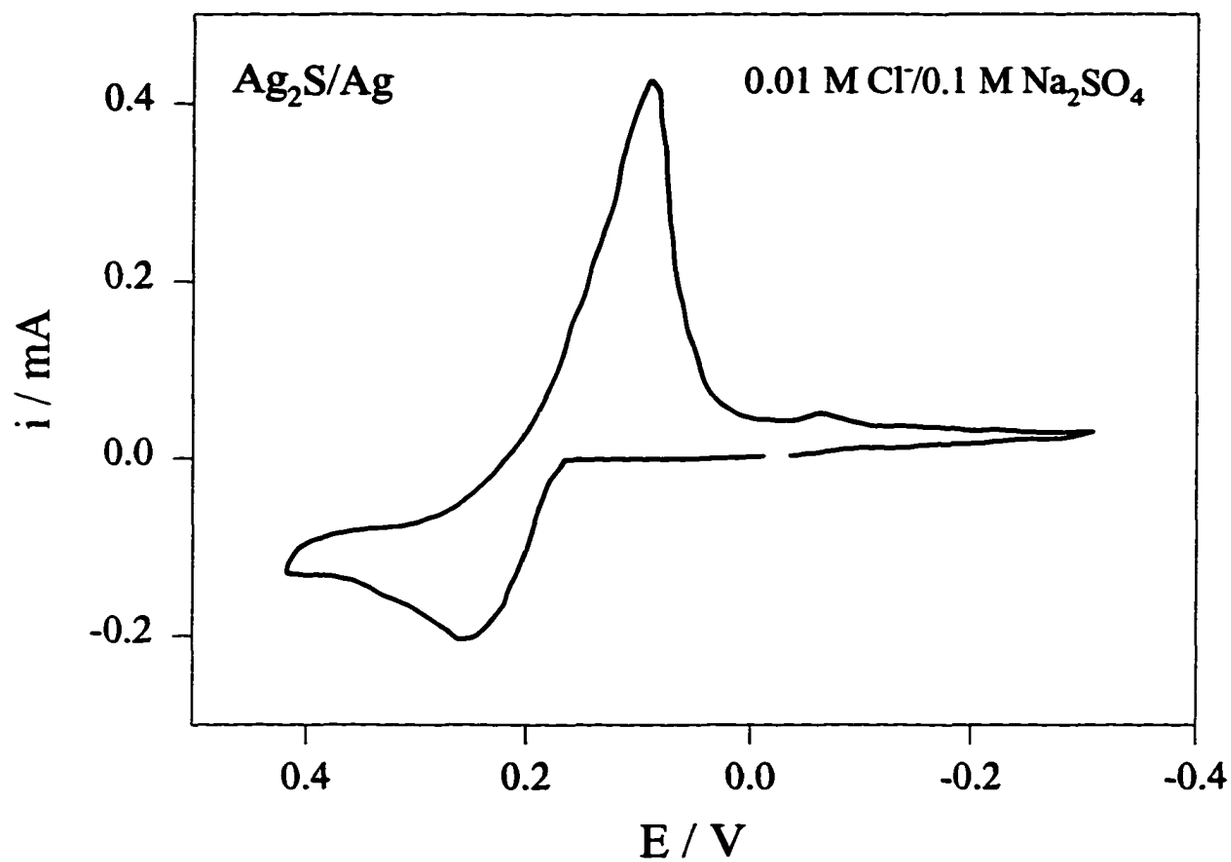

Figure 6. Cyclic voltammogram (CV) of Ag_2S-coated Ag electrode in Na_2SO_4 electrolyte containing Cl^-. Scan rate: 50 mV/sec.

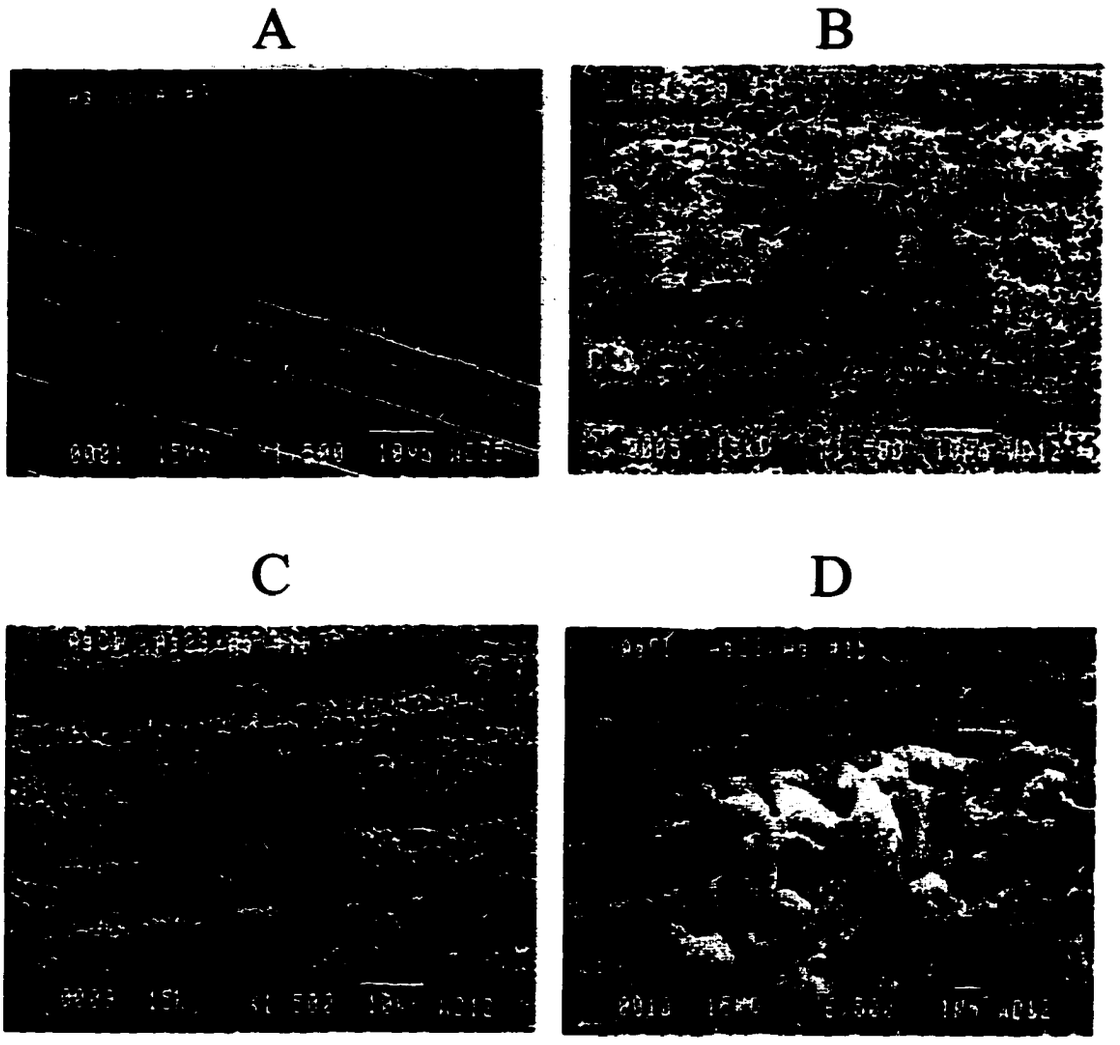

Figure 7. SEM of (a) Ag, (b) Ag_2S-coated Ag, (c) b following Cl^--removal, and (d) enlarged image of c.

Table 7. Voltammetric Peak Characteristics of Ag_2S/Ag Coil Electrodes (with 0.1 M Na_2SO_4)

Electrolyte	E_{pa} (V)	E_{pc} (V)	ΔE_p (V)	E_0^* (V)
0.003 M KCl	0.27	0.09	0.18	0.18
0.01 M KCl	0.23	0.08	0.15	0.15
0.03 M KCl	0.23	-0.05	0.28	0.09

The silver chloride appears to grow through the porous structure of silver sulfide to the surface (mushroom-like feature). The EDS data clearly indicates a composition dominated by AgCl at the area with the mushroom feature, and a composition dominated by Ag_2S as the background feature, i.e., the Ag_2S surface. After ~60 cycles of the Ag/AgCl reaction, the regenerated surface composition is predominated by Ag, suggesting the sulfide is deeply buried under the silver layer. Another important observation was the appearance of large, dark areas at the uncoated silver electrode following Cl^--removal of RAW samples. The composition of such spots was primarily carbon based particulate, as detected by EDS. This was strong evidence that the silver sulfide coating effectively prevents the surface from adsorbing COD particulate, a result consistent with the COD analyses.

Additional evidence by surface sensitive x-ray photoelectron spectroscopy (XPS) is basically consistent with the EDS results. The relative composition changes from a Ag_2S/Ag to AgCl/Ag_2S/Ag stratification (after Cl^- removal) and to a film layering of Ag/Ag_2S/Ag (after regeneration) are listed in Table 9. Following Cl^--removal with RAW sample solutions, the XPS results on the Ag_2S/Ag electrode indicated the presence of carbon and mercury (Figure 8). The surface profile of the sample, as exhibited in Figure 8, suggests that

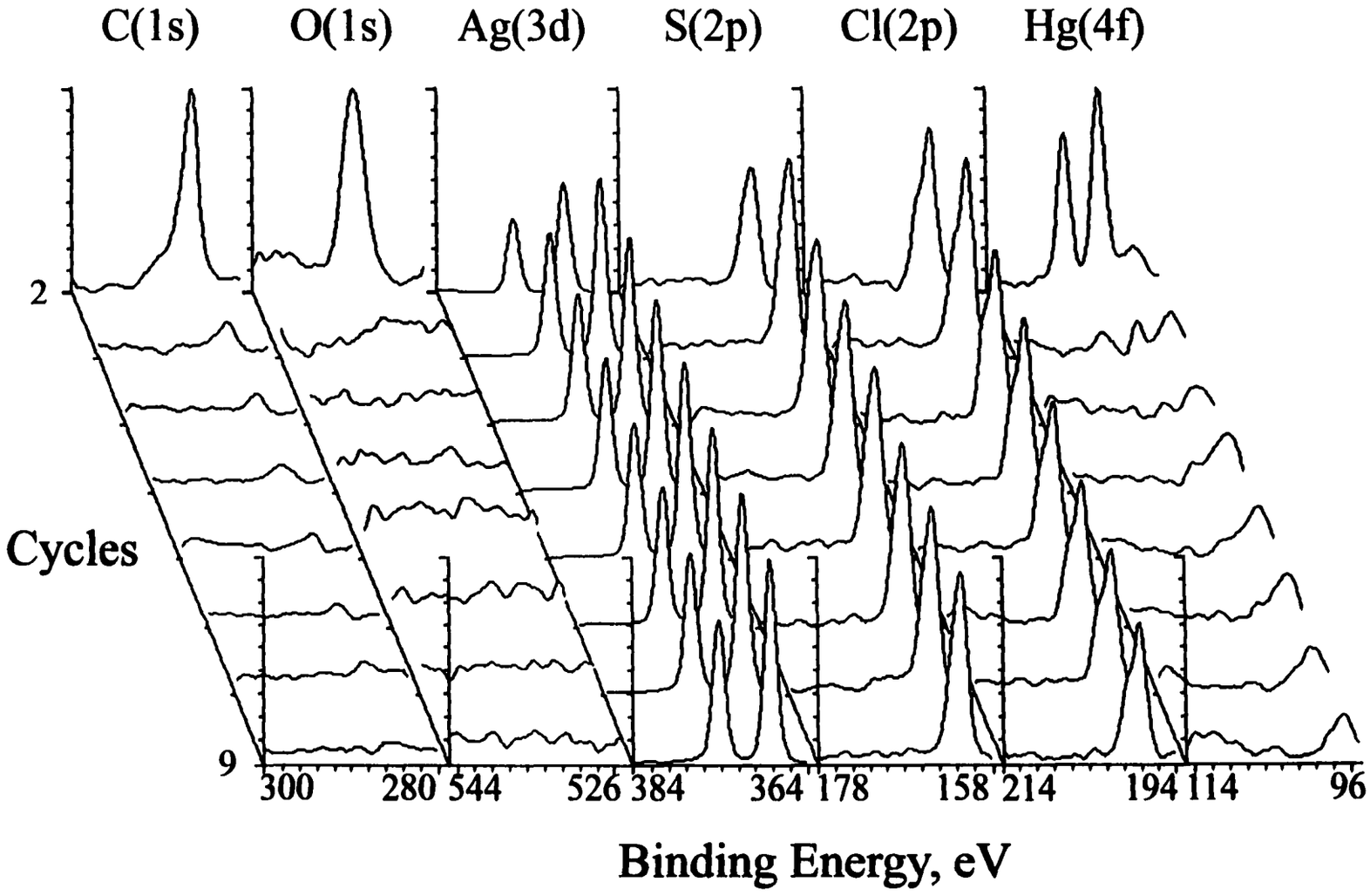

Figure 8. XPS surface profiling, as a function of surface sputtering, of a Ag_2S-coated Ag electrode following Cl^- pretreatment of a RAW sewage sample solution.

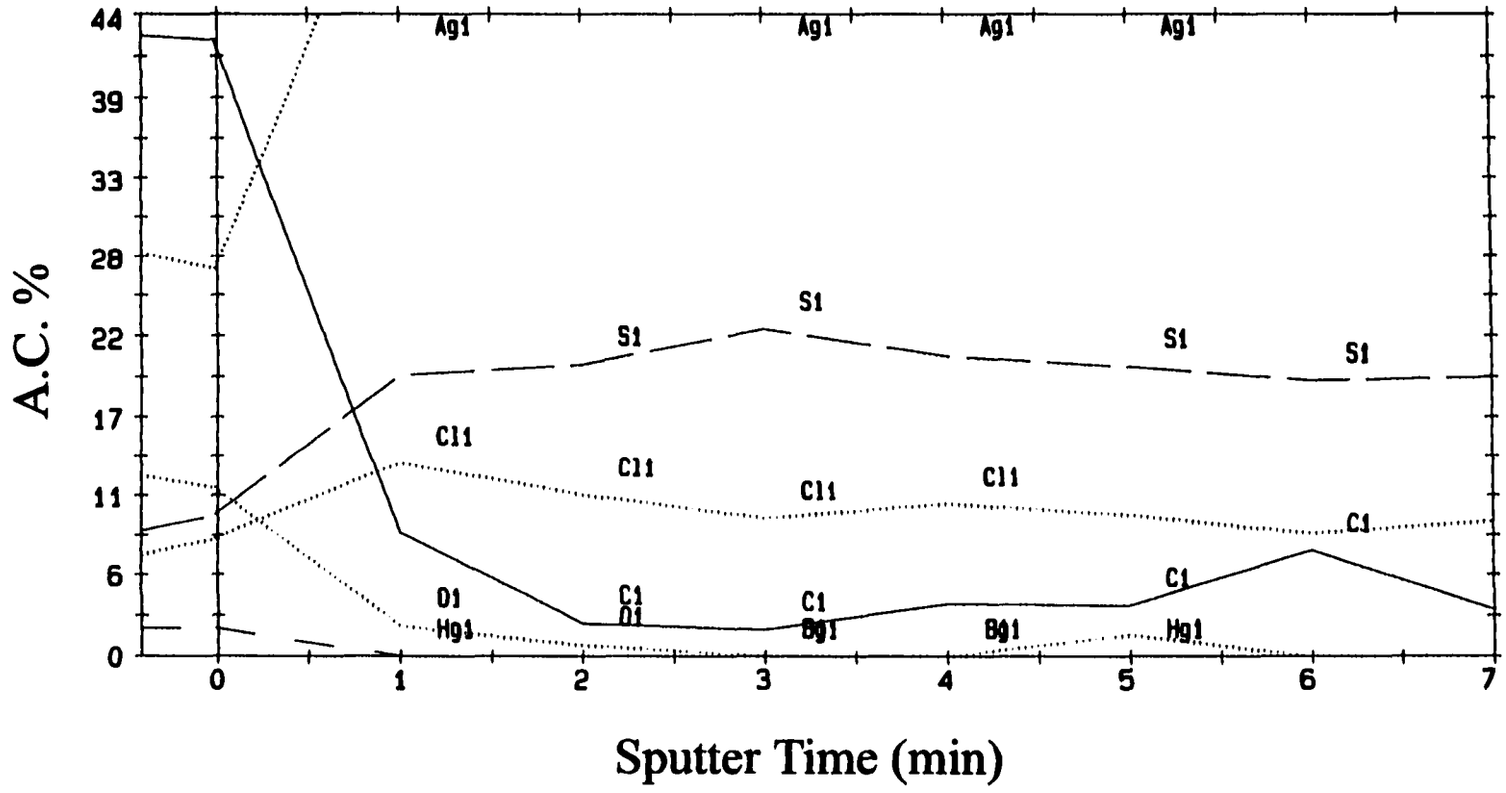

Figure 8. (continued)

Table 8. Results of Electron Dispersive X-Ray Spectroscopic (EDS) Analysis

Electrode sample	Surface treatment	Probe Area	Elemental composition detected			
			Ag	S	Cl	C
Ag_2S/Ag	untreated	all area	64.65	35.35	0.00	-
Ag_2S/Ag	AgCl formed from 0.01 M KCl	white area	56.83	1.43	41.73	-
		dark area	67.31	30.42	2.26	-
Ag_2S/Ag	Ag regenerated from AgCl	all area	68.84	31.09	0.07	-
Ag_2S/Ag	Ag regenerated from AgCl (60 cycles)	all area	99.67	0.33	0.00	-
Ag_2S/Ag	AgCl formed from *Raw*-solution	dark area	63.60	28.96	7.44	-
Ag	AgCl formed from 0.01 M KCl	all area	80.38	0.15	19.47	-
Ag	AgCl formed from *Raw*-solution	white area	71.56	0.30	28.14	-
		organic mass area				C detected

Table 9. Surface Composition Analysis Using XPS

Sample	Composition (%)				
	C1s	O1s	Ag3d	S2p	Cl2p
Ag_2S/Ag	30.02	22.37	32.68	14.93	-
AgCl/Ag_2S/Ag	22.95	5.00	39.78	1.06	31.20
Ag/Ag_2S/Ag	2.33	0.30	83.71	10.55	3.10

the organic and mercury contaminants are on the outer layer (absent after ~2 min sputtering). In contrast, Cl^- permeated deeply into the Ag_2S film, a result consistent with the conclusion that multilayers of AgCl can be formed into the Ag_2S film coated electrodes.

Conclusions

In this work, the electrochemical approach to the elimination of Cl^- interference in chemical oxygen demand (COD) analysis was successfully demonstrated with both reticulated vitreous carbon (RVC)-supported silver film and silver coil electrodes in controlled and wastewater samples. The electrochemically-deposited silver film on RVC was highly disperse, as exhibited by SEM imaging, reflecting the high Cl^--removal efficiency of the electrode. The silver coil electrodes accommodate small sample volumes ($\sim\leq$0.5 mL), which is desirable for many field applications to minimize reagent consumption. Chloride ion was removed from samples with initial Cl^- concentrations ranging from 100 to 1000 ppm to levels below 3 ppm, with analysis times of $\leq$ 15 min, and a COD precision of $\leq \pm$ 20%.

We also demonstrated a new strategy of surface coating to reduce the probability of particulate entrapment or adsorption on the uncoated electrodes, which attributed to a loss of ~50% COD from sewage wastewater samples. An example of this strategy was coating the surface with a low surface free energy film such as silver sulfide, chemically or electrochemically. Without changing the Cl^--removal efficiency, the resulting surface coating dramatically reduced COD adsorption losses to < 10%, an acceptable level for most applications. Our results not only demonstrate a new technology for removing chloride in

real-world samples for COD analysis but also probes the fundamental understanding of surface treatment and film growth at a silver electrode.

This electrochemical Cl^--removal method offers several advantages over the traditional methods. One of them is the utility of an electrode as a reagent for oxidation or reduction reaction, rather than the traditional chemical reagents. The electrodes are reusable and environmental friendly. Although there is still some detectable COD loss due to adsorption at the surface during AgCl growth, the coating strategy does provide a new route for substantial improvement in minimizing COD losses.

Acknowledgments

The expert assistance of Jim Anderegg in XPS measurement is greatly acknowledged. This work was supported in part by Hach Company, the Office of Basic Energy Sciences, Chemical Science Division, of the U.S. Department of Energy, and the Microanalytical Instrumentation Center of Iowa State University. The Ames Laboratory is operated for the U.S. Department of Energy by Iowa State University under Contract No. W-7405-eng-82.

References

(1) Gibbs, C. R. In *Technical Information Series-Booklet No. 8*; Hach Company, 1993.

(2) In *Standard Methods for the Examination of Water and Wastewater*; Greenberg, A. E., Trussel, R. R., Clesceri, L. S., Eds.; American Public Health Association: New York, 1985; Vol. 16.

(3) Smith, R. K. *Handbook of Environmental Analysis*, 2nd ed.; Genium Publishing Corporation: New York, 1994.

(4) Ballinger, D.; Lloyd, A.; Morrish, A. *Analyst* **1982,** *107*, 1047-1053.

(5) Lloyd, A. *Analyst* **1982,** *107*, 1316-1319.

(6) Pitrebois, L.; Schepper, H. D. *Trib. Cebedeau* **1984,** *37*, 83-86.

(7) Wagner, V. R.; Ruck, W. *Z. Wasser Abwasser Forsch* **1982,** *15*, 287-290.

(8) Wagner, V. R.; Ruck, W. *Z. Wasser Abwasser Forsch* **1981,** *14*, 145-151.

(9) Bauman, F. J. *Anal. Chem.* **1974,** *46*, 1336-1338.

(10) Dobbs, R. A.; Williams, R. T. *Anal. Chem.* **1963,** *35*, 1064-1067.

(11) Thompson, K. C.; Mendham, D.; Best, D.; Casseres, K. E. d. *Analyst* **1986,** *111*, 483-485.

(12) *Reference Electrodes, Theory and Practice*; Academic Press: New York, 1961.

(13) Katan, T.; Szpak, S.; Bennion, D. N. *J. Electrochem. Soc.* **1973,** *120*, 883-888.

(14) Jaya, S.; Rao, T. P.; Rao, G. P. *J. Appl. Electrochem.* **1987,** *17*, 635-640.

(15) Giles, R. D. *J. Electroanal. Chem.* **1970,** *27*, 11-19.

(16) Yeager, E.; Bockris, J. O. M.; Conway, B. E.; Sarangapany, S. *Fundamentals of Transport Phenomena in Electrolytic Systems*; Plenum Press: New York, 1982.

(17) Strohl, A. N.; Curran, D. J. *Anal. Chem.* **1979,** *51*, 1045-1049.

(18) Wang, J.; Dewald, H. D. *J. Electrochem. Soc.* **1983,** *130*, 1814-1818.

(19) Vermilyer, D. A. *Advances in Electrochemistry and Electrochemical Engineering;* Interscience Publishers: New York, 1963.

GENERAL CONCLUSIONS

This dissertation has investigated approaches to chemically modifying metal and polymer surfaces for applications to chemical analysis, and demonstrated SFM's ability to characterize interfacial chemical reactions at nanoscale level for probing the microscopic surface reactivities, which other surface characterization tools cannot do.

Chapter 1 has demonstrated that the pH sensors based on the covalent immobilization of fluoresceinamine at hydrolyzed cellulose acetate film show a rapid response time (< 30 s), a large dynamic range (> 7 pH units), and exceptional long-term stability (several months). The immobilization schemes are both simple and free of organic solvents. Compared with the indirect immobilization scheme, the direct immobilization procedure is simpler, and the large background due to light scattering by the beads is minimized. However, the sensor film prepared through indirect immobilization scheme shows better mechanical strength and gives better long-term stability than the one that was prepared through direct immobilization scheme. An extended pH sensitivity is achieved by co-immobilizing fluoresceinamine and Congo Red at a hydrolyzed cellulosic film.

Chapter 2 and 3 have demonstrated that frictional force imaging can be applied to follow interfacial chemical transformations at microscopic level. The base-hydrolysis of a dithio-bis(succinimidylundecanoate) monolayer chemisorbed on a gold substrate was monitored in situ with scanning force microscopy (SFM). The results indicate that the friction at the microcontact formed between a Si_3N_4 probe tip and a dithio-bis(succinimidylundecanoate)-modified Au(111) substrate increases as the succinimidyl

group is replaced by the carboxylate ion. This increase is consistent with an increase in the interfacial surface tension at the microcontact. The correlation between the macroscopic data determined from IRS and the microscopic data determined from the in situ SFM images confirms that the friction change was resulted from the composition change during the hydrolysis. The study also shows the heterogeneity in the reaction rates on different areas of the surface, and the acceleration of the reaction rate by the nano-contact between the tip and surface.

An electrochemical approach to the elimination of Cl^- interference in chemical oxygen demand (COD) analysis was examined in Chapter 4. Both silver-supported reticulated vitreous carbon (RVC) and silver coil electrodes were successfully utilized for removal of Cl^- in controlled and wastewater samples. Chloride ion was removed from samples with initial Cl^- concentrations ranging from 100 to 1000 ppm to levels below 3 ppm, with analysis times of $\leq$ 15 min, and a COD precision of $\leq \pm 20\%$. By coating the surface with a low surface free energy film such as silver sulfide, the probability of particulate entrapment or adsorption on the uncoated electrodes, which attribute to a loss of ~50% COD from sewage wastewater samples, has been reduced to < 10%.

The ability to not only characterize interfaces at atomic scale, but also manipulate atoms and molecules on surfaces with atomic precision will open opportunities for the nanofabrication of materials. For example, the fact that the contact imaging with SFM can accelerate the reaction rate in a localized region creates the possibility of making microscale sensor arrays by creating chemically inhomogeneous patterns of nanometer scale dimensions.

With the advancement of technology, interfacial phenomena will be better understood and play a more important role in a variety of applications.